ELECTROMAGNETIC STIMULATION ON MAGNETIC PLASMONIC

NANOPARTICLES TO REGULATE CELLULAR ACTIVITIES

A Dissertation

by

MUZHAOZI YUAN

Submitted to the Office of Graduate and Professional Studies of
Texas A&M University
in partial fulfillment of the requirements for the degree of

DOCTOR OF PHILOSOPHY

Chair of Committee,	Ya Wang
Committee Members,	Ying Li
	Gerard L. Coté
	Samuel B. Mabbott
Head of Department,	Andreas A. Polycarpou

August 2019

Major Subject: Mechanical Engineering

ABSTRACT

Neurodegenerative disorder imposes a significant challenge in neuroscience due to the lack of effective treatment to reverse the progress. Here we introduce an approach of using multifunctional superparamagnetic iron oxide (SPIO)-gold (Au) core-shell nanoparticles (NPs) to regulate cellular activities and promote neuronal differentiation and neurite growth under the stimulation of electromagnetic fields. SPIO-Au NPs were firstly synthesized by a synergistic seed growth method with tunable thicknesses, uniform quasi-spherical nanostructures and excellent plasmonic properties. The high stabilities of SPIO-Au NPs in deionized water and cell culture medium were then confirmed by UV-Vis absorption spectra and zeta potential measurements. The outstanding plasmonic properties were further characterized by using a novel thermocouple (TC)-tip-exposing technique to measure the temperature profile of NPs with laser irradiation in a simple and accurate way. The near unity photothermal conversion efficiency (≈ 1) of NPs (26 nm) was demonstrated by embedding the finite element modeling with experimentally measured parameters.

Then the SPIO-Au NPs were functionalized with nerve growth factor (NGF) with high stability for the magnetic fields (MFs) stimulation. The enhanced cell uptake of NPs by the bounded NGF and their high cell viability were observed in PC-12 neuron cells. The NGF-SPIO-Au NPs also showed the promotional effect on neuronal differentiation, neurite growth and orientation by the stimulation of dynamic MFs, which performed better than their static counterparts.

In the end, the effect of NGF-SPIO-Au NPs on promoting the neuronal differentiation in response to light emitting diode (LED) stimulation was explored. LEDs (1.9 mW/cm^2) exhibited no obvious cellular toxicity and no significant reduction of proliferation for up to 1 h of exposure. The promotional effect of LEDs and NGF-SPIO-Au NPs on neuronal differentiation and neurite growth was proved through morphology studies. The stimulation of LEDs on NGF-SPIO-Au NPs with strong photothermal effect also triggered an increase of calcium level and the upregulation of the neuronal differentiation specific marker β3 tubulin and the cell adhesive molecule integrin β1 through the activation of plasmonic NGF-SPIO-Au NPs. To conclude, the capacities of multifunctional SPIO-Au NPs on regulating the cellular activities and promoting the neuronal differentiation suggest the strong potential of this nanomedicine for neuroregeneration.

ACKNOWLEDGEMENTS

I would like to express the deepest appreciation to my committee chair, Dr. Ya Wang, who introduced me to work in these interesting topics and enlightened me in solving scientific problems: she continually guided me both in my academic work and my personal life. Without her persistent support, this dissertation would not have been possible.

I would like to thank my committee members, Dr. Ying Li, Dr. Gerard L. Coté and Dr. Samuel B. Mabbott, for generously offering their time, guidance and support throughout the preparation of this dissertation. I would also like to thank Dr. Yi-Xian Qin for providing amazing facilities for running cell work and sharing his biomedical expertise so willingly. And thank Dr. Jon P. Longtin and Dr. David Hwang for their continuous instruction and assistance on the configuration of the photothermal experiments setup, the construction of the heat transfer model and the paper writing.

Thanks to Dr. Dongye Zhang, for providing me with a fantastic lab training of cell work. And thanks to Grace Hu, for her kindly assistance during the experiments and the report writing.

Thanks to my colleagues, lab mates, department faculty and staff for their kindly assistance of my research.

Finally, thanks to my husband and my son for their encouragement, patience, and love throughout my Ph.D. study.

CONTRIBUTORS AND FUNDING SOURCES

Contributors

This work was supervised by a dissertation committee consisting of Professor(s) Ya Wang [advisor] and Ying Li of the J. Mike Walker '66 Department of Mechanical Engineering and Professor(s) Gerard L. Coté and Samuel B. Mabbott of the Department of Biomedical Engineering.

All the work conducted for the dissertation was completed by the student independently.

Funding Sources

TABLE OF CONTENTS

LIST OF FIGURES

LIST OF TABLES

CHAPTER I

INTRODUCTION*

Motivation: Neurodegenerative diseases, like Alzheimer's and Parkinson's, and other neurological damages like traumatic brain injury resulting from the loss of neurons in the brain, have been a major challenge in neuroscience. Axon regeneration in humans generally occurs at very low speed (2-5 mm/day), which leads to the extremely prolonged recovery time.[1] Therefore the study of the regenerative agents and techniques that promote the nerve repair and speed the neuronal growth and differentiation is of great interest. Nerve growth factor (NGF) has the strong pharmacological potential for the treatment of neurodegenerative diseases as it is essential for the stimulation of neuron survival and differentiation.[2] However the short half-life and slow diffusion restricted the therapeutic usage of NGF. Nanoparticles (NPs) as drug carriers have been demonstrated to influence the activity and stability of therapeutic molecules, and enable the extended half-life and increased efficiency of NGF.[3] Multifunctional core-shell NPs are promising nanocarriers to deliver the therapeutic biomolecules like NGF across the blood-brain barrier (BBB) for the treatment of nerve repair. Capable of magnetic and plasmonic responses, multifunctional magneto-plasmonic NPs are of great interest among other type of NPs

because of their strong potential to regulate cellular activities and neuronal differentiation through generating mechanical tensile forces under external magnetic fields (MFs) or producing photothermal effect by light stimulation.

SPIO-Au core shell NPs

Advanced medical techniques for taking advantages of the special optical properties has driven the development of superparamagnetic iron oxide (SPIO) NPs coupled with active coatings, such as metal,[4-8] alloy,[9] polymer or nonmetallic oxides.[10] SPIO NPs have been widely studied for their unique magnetic properties in the biomedical field. For example, SPIO NPs have been used as a highly sensitive contrast agent,[11,12] noninvasive cell labeling[13-15] and visualization using magnetic resonance imaging (MRI).[16] Besides their potential applications as contrast agents, SPIO NPs can also be directed to a specific site by external MFs, which further extends their usage in targeted drug or gene delivery.[17] However the direct use of uncoated magnetic NPs faces challenges such as their instability in biological environments,[1,18-20] , aggregations,[16] and the cellular toxicity.[21-24] To address these issues, magnetic NPs can be protected by a thin and impenetrable shell made by biocompatible materials, which not only shield the magnetic core from being exposed to surroundings but also make them to be readily functionalized with different groups.[25] The coating modifies the surface function of the SPIO NPs to reduce their toxicity,[17,26] increase their anti-oxidation resistance,[12] and improve their plasmonic properties,[27] e.g., photothermal therapy,[28-32] brain tumor imaging,[16,18] active targeting[19] and drug delivery.[20,22] Among various active coating materials (polymer, alloy, metal, etc.),[5,33,34] gold (Au) exhibits excellent

biocompatibility[35-37] and low cytotoxicity because of its inertness and high stability.[6,7] Au not only shield the magnetic core from exposure to complicated environments, but also provides tunable surface functionalization with various ligands such as proteins, aptamers and peptides through its stable thiol (-SH) and amide ($-NH_2$) binding affinity.[38-40] The tunable surface functionalization[23,24,33,41-44] of Au NPs due to the well-developed Au-S chemistry[45,46] further extends their applications to the fields of drug/gene delivery,[47,48] fluorescence imaging,[49] cell labeling[50] and bio-sensing.[41] Especially, the surface plasmonic resonance of Au coatings provides an efficient mechanism to convert photon energy to thermal energy when Au coatings are irradiated at their resonance wavelength with a laser[51-56] for photothermal therapy. Au-coated SPIO NPs can also be stabilized more efficiently with NGF, biomolecule,[23,42,43] cytotoxic agents[44] or tumor-targeting molecules.[57] This makes Au-SPIO NPs an extremely interesting nanomedicine for photothermal treatment,[28-32] bone regeneration, nerve regeneration and many other medical applications.[58,59]

Synthesis of SPIO-Au NPs

Important progress has been made in chemical synthesis of the monodisperse Au NPs[60,61] and the Au coated magnetic NPs.[4,6,46,57,62-64] The monodisperse Au NPs can be synthesized by seed growth method with mild reducing agents like citrate acid to obtain Au NPs of different size. The controlled seeded growth method combining the Turkevic[61] citrate reducing method was proposed by Bastus[60] to form the citrate-stabilized monodisperse Au NPs (from 10 ~ 180 nm) with quasi-spherical shape and a narrow size distribution and controlled diameter, by controlling the reaction condition such as the PH, seed to gold

precursor ratio, temperature, etc. The Au coated SPIO NPs can be synthesized in a similar way. Instead of using Au NPs, SPIO NPs can be used here as seeds and the Au shell can be formed at the surface of SPIO NPs, followed by the formation of thicker Au shell by simply adding more chloroauric acid and reducing agent to the aqueous solution. For example, Fan et al[63] used citrate reducing method to form Au coated Fe_3O_4 magnetic NPs. They first prepared the iron oxide NPs as seeds by co-precipitation method and then coated them with Au shell by reducing Au^{3+} into Au on the iron oxide surface. The adding of sodium citrate and gold chloride solution was repeated several times to achieve thicker shell. However there is a lack of enough characteristics to demonstrate the formation of SPIO-Au NPs. Another strategy is developed by Xu et al.[6] to form Au coatings (1, 1.5, 2, and 2.5 nm) on Fe_3O_4 cores (10 nm) using ascorbic acid as reductant. Yet the difficulty of removing extra CTAB makes the NPs less bio-friendly. Lyon et al[62] also developed an iterative hydroxylamine seeding method to synthesize the Au coating on Fe_2O_3 cores at a total diameter of 60 nm with 14 nm standard deviation.

Exploration of plasmonic property via photothermal measurement of SPIO-Au NPs

The localized surface plasmon resonance (LSPR) of Au NPs is caused by the collective resonation of the conduction free electrons at the certain wavelength of light. Such a superior optical property of Au NPs indicates their potential advantages in photothermal therapy to efficiently convert photon energy to thermal energy when irradiated by a laser at their resonance wavelength.[28,30-32,51-53] When Au is used as a coating material for SPIO NPs, this newly formed SPIO-Au nanomedicine expands its usage in many medical fields, such as magnetic hyperthermia[65] and photothermia[28,31] where their

4

light-to-heat conversion efficiency becomes critical.

Before using SPIO-Au NPs for photothermal therapy, it is necessary to develop techniques to quantify the photothermal properties of SPIO-Au NPs. Traditional techniques for the photothermal conversion efficiency measurement and calculation rely mainly on experimental techniques. One method was developed in 2007 by Roper et al.,[52] which proposed a microscale heat transfer model and designed an experimental setup of placing the cuvette in the vacuum condition to measure the temperature profile of Au NPs (20 nm diameter, 920 ppm in deionized (DI) water, 7.9 ul, 350 s to reach equilibrium) using a 514 nm continuous wave (CW) laser (0.17 W, 3 mm beam size). According to their modeling and calculation of the time constant, the photothermal conversion efficiency η of Au NPs of 920 ppm was 0.034, which was very low and inaccurate. The possible reason is that the mass of water was greatly underestimated during the photothermal conversion efficiency calculation because of the heat convection dominated heat transfer driven by the temperature gradient in the NPs solution under the illumination of the laser. Until now, Roper's method of using the time constant was still adopted for measuring the photothermal conversion efficiency of several newly synthesized plasmonic NPs.[66-68] Followed the same method, Feng et al. (2015)[66] measured the photothermal conversion efficiency (η=0.24) of Au/Polypyrrole@Fe_3O_4 NPs (200 nm, 1400 ppm) using an 808 nm laser at a power density of 2 W/cm^2. Hu et al.(2017)[67] tested the photothermal conversion efficiency (η=0.1) of Au-coated Fe_3O_4 NPs (100 nm, 0.78-100 ppm) using an 808 nm laser irradiation at 15 W/cm^2. Wang et al. (2018)[68] measured the photothermal

conversion efficiency ($\eta = 0.618$) of MoSe$_2$ nanoflowers (150-180 nm, 75 ppm) using an 808 nm laser at a power density of 1 W/cm^2.

To address the aforementioned inaccuracy in the time constant method developed by Roper et al,[52] Jiang et al. (2013)[53] used a stirrer to experimentally reduce the temperature gradient in the Au NPs solution (5-50 nm, 39.4 ppm, 1 mL) inside the cuvette under the laser irradiation (532 nm, 0.228 W, 2 mm beam size). It took at least 1200 s to reach an equilibrium and the calculated efficiency was size-dependent and reached 0.737 for Au NPs of 18 nm in diameter. As a result, the heat conversion efficiency of Au NPs was largely modified compared with Roper's method. Unfortunately, due to some possible collective heating losses during the long period to reach the equilibrium state, their experimental data was not quantitatively correlated with the theoretical prediction of conversion efficiency η, which was proportional to the ratio of absorbance/extinction in order to account for scattered light that removes non-heat energy from the system.

In comparison with Roper's work, Richardson et al.(2009)[51] developed a new experimental technique by controlling a hanging drop (10 ul) of Au NPs solution (20 nm, 45 ppm) from a syringe needle with thermocouple (TC) tip inside the droplet to measure the temperature profile of NPs under a 532 nm CW laser (0.14 W, 0,23 W and 0.28 W). The time to reach equilibrium was about 50 seconds. Using their measurement setup, the efficiency η was determined to be very close to 1 (0.97-1.03), which was in agreement with the expectation of the near unity energy conversion of photon to heat for small NPs because of the nearly zero quantum yield (10^{-6}).[69] However this method required careful control of the syringe droplet and the evaporation of the NPs solution cannot be avoided

during the laser irradiation. After reviewing the techniques developed in the literature for the measurement of photothermal conversion efficiency, it is necessary to develop a simple but accurate technique to easily measure the temperature profile and to yield a highly accurate calculation of the photothermal conversion efficiency of different plasmonic NPs of different sizes and concentrations.

Biocompatibility of SPIO-Au NPs

So far, many studies have been carried on to evaluating the biocompatibility of pure Au NPs with different sizes. High viability towards different cell lines was found for citrate-capped Au NPs of 4 nm by Connor et al.[70] and 12 nm by Mustafa et al.[59] The impact of aggregation of Au NPs was examined by Albanese et al.[71] They found that the aggregation of Au NPs does not induce the toxicity of Hela cells. Moreover, Kawazoe et al.[45] proved the good viability of Au NPs conjugated with different surface functional groups, such as amine, carboxyl, hydroxyl and citrate, towards human MSCs. SPIO-Au core-shell NPs (36-56 nm, 1-500 µg/mL) were proved to be nontoxic to mouse leukemic monocyte macrophage cells by Zhang et al. (> 90% viability, 3 days of incubation).[7] However, they were not able to test the concentration-dependent cell viability for longer incubation periods and there was a lack of proliferation evaluation, which is essential for the application of this nanomaterial in regulating neuronal activities.[72]

Multifunctional SPIO-Au NPs for nerve regeneration

MF stimulation

Due to the slow rate of axonal regeneration,[73] neuroregeneration, one of the most significant challenges in neuroscience, has driven extensive studies focused on techniques

to increase the speed of neuron recovery. Many efforts have been contributed to develop the molecules,[74,75] proteins,[76,77] growth factors[78,79] and biomaterials[80,81] possessing the ability to stimulate or direct the axonal outgrowth. Among them, NGF has been found to be essential for the neuronal growth and differentiation via the tropomyosin kinase receptor and the non-selective p75 neurotrophin receptor.[82,83] However, the slow diffusion and short half-life of NGF from the enzyme degradation[84,85] have restricted its application in neuroregeneration. Moreover, the main obstruction impeding its in-vivo studies is that many drugs designed for the treatment of nerve recovery like NGF cannot be easily transported through the blood brain barrier (BBB) due to the selective permeability of the BBB.[86] Therefore, it is necessary to find a suitable carrier to efficiently deliver nerve regenerative agents such as NGF across BBB and to enhance the half-life and efficiency of NGF in promoting neuronal growth.

Magnetic NPs have been extensively used in clinical practice, such as MRI,[12,15,16] cell-labeling[13,14] and targeted drug or gene delivery[17] due to their special magnetic properties. Recent studies have examined the effect of SPIO NPs as the nanocarrier of NGF, and have shown the improvement of neurite outgrowth on PC-12 cell line.[87] M. Marcus et al.[3] found the promotion effect of differentiation and neurite outgrowth of PC-12 cells and the extension of the NGF's half-life by conjugating NGF with SPIO NPs. They have also proved the ability of iron oxide NPs to direct the neurite orientation.[88] Christina Riggio et al.[1] confirmed that the NGF functionalized magnetic NPs can guide the neurite outgrowth along the external MF direction by generating a tensile force under the applied MFs. It was also demonstrated that the effective delivery of brain-derived neurotropic factor

(BNDF) across the BBB can be achieved by using magnetic NPs as the nano-carriers, which enables the in-vivo application of BNDF.[86] However, none of the previous work involves the study of SPIO-Au NPs for nerve regeneration and the demonstration of dynamic magnetic field stimulated neurite growth through activating the magnetic SPIO-Au NPs, which are also the potential nano-carriers of NGF for nerve regeneration due to their unique magnetic, optical and chemical properties.

LED light stimulation

Engineered NPs mediated by external stimuli have attracted accumulative attentions in nanomedicine for non-invasive or less invasive therapeutics. In particular, Au NPs have been used as a mediator to induce light-based neuro-stimulation through photothermal effect from LSPR.[89] SPIO NPs can also be stimulated by MF for nerve regeneration due to their strong magnetic properties.[1,88,90] Adding a protective and functional shell of Au on SPIO core to avoid aggregation[12] and enhance the biocompatibility,[5] SPIO-Au core-shell NPs possess very unique and attractive features integrating the magnetic properties of SPIO and the LSPR properties of Au into one single nanoplatform,[6,7,70] and therefore exhibit strong potential for many multimodal biomedical applications, such as the targeted drug delivery,[91,92] photo induced/magnetic hyperthermia[93-95] and imaging-assisted cancer treatment.[96,97]

However, among these applications, there has been no attempt to use NGF-SPIO-Au NPs to modulate neuronal activities under photostimulation. In comparison with other traditional stimuli such as electrical stimulation,[98] photostimulation is considered non-invasive and relatively harmless. [99-101] In comparison with other types of nanomedicine,

NGF-SPIO-Au NPs have their unique advantages for brain therapeutics. First of all, the gold shell can help regulate neuronal functionality since the plasmonically-induced heat activates temperature-sensitive channels in neurons[102] for excitation[103] and inhibition[104] of action potentials. Such a photothermal effect is also believed to regulate Ca^{2+} level,[105] which is critical for transmitting neuronal signals between neurons,[106, 107] and for regulating cytoskeleton growth behaviors via phosphorylation.[108] Besides, the effective loading of therapeutic molecule (like NGF) and the magnetic property enabled the usage of magnetic force guided drug delivery. Our team has recently synthesized NGF-SPIO-Au NPs using a facile method and proved their stimulation impact on neuronal growth and differentiation under dynamic MFs.[90,109] However, how this nanomedicine responds to photostimulation, an advantageous non-invasive tool to regulate neuronal activities and promote nerve regeneration, is still unknown.

Traditional photostimulation strategies rely on laser sources which could induce potential tissue damages, often require a high-voltage power supply, and are costly.[103] As an emerging alternative to a laser,[13] light emitting diode (LED) is portable, cheap, consumes little power, and has negligible human and environmental toxicity.[110-114] It has shown potentials for improving cognition on patients with chronic and traumatic brain injury (TBI).[115] The effect of 940 nm LED on sciatic nerve regeneration was also reported on rats,[116] which showed improved morphofunctional sciatic nerve recovery with phototherapy after nerve damage. However, LED has not been used as a light source to irradiate and activate plasmonic NPs, especially NGF-SPIO-Au NPs for regulating neurological functions through the plasmonically-generated heating effect.

Objectives and outlines

With the ultimate goal of promoting the development of nanomedicine-based neurogenesis induction scheme for optimized nerve regeneration and repair, the objective of this dissertation is to study the multifunctional plasmonic-magnetic behavior of SPIO-Au NPs and their synergistic effect on neuronal activities with the stimulation of electromagnetic fields (MFs and LED light).

In **Chapter II**, we describe the synthesis method of SPIO-Au NPs and their characterization techniques. This includes the reaction conditions, synthesis protocols, reagents and operational conditions of sample characterization such as TEM and light absorbance spectrum. A synergistic seed growth method is developed to synthesize SPIO-Au NPs with tunable size, narrow size distribution, high dispersity and excellent plasmonic property. The stabilities of NPs are then investigated by UV-Vis absorption spectra and zeta potential measurement.

In **Chapter III**, in order to explore the plasmonic behavior of SPIO-Au NPs under laser irradiation, we develop a simple but accurate TC tip exposing technique to measure the photothermal efficiency of SPIO-Au NPs (Diameter: 20.8 nm) by embedding the experimentally measured data into the finite element modeling (FEM). The heating period is restricted to the first 30 seconds. Within such a short period of laser exposure, the characteristic heat diffusion length is smaller than the cuvette dimensions, so the heat transfer process was simplified by avoiding both the natural convection and the influence of the container geometry on the heat transfer of the SPIO-Au NPs aqueous solutions. The

TC tip exposing technique also reduces the complexity of the experimental set-up and assures the accuracy of the measurement by directly placing the TC tip in the center of the laser beam.

In **Chapter IV**, the effect of magnetic stimulation on multifunctional SPIO-Au NPs (Diameter: 20.8 nm) is explored. The parametric effects on cell viability and cellular uptake are studied to explore the impact of different concentrations and conjugating of NGF. Then the static and dynamic MFs are constructed and applied on PC-12 cells treated with NGF functionalized SPIO-Au (NGF-SPIO-Au) NPs to compare which configuration is preferred to promote neuronal differentiation, neurite growth and orientation. Finally, the cytoskeleton force-based model is developed to predict the neurite elongation and the orientation stimulated by magnetic fields, and the effectiveness of which can be demonstrated with experimental data.

In **Chapter V**, to explore the effect of light stimulation on neuroregeneration, we use low-intensity LEDs (<2 mW/cm^2) to irradiate NGF-SPIO-Au NPs of 20.8 nm diameter and 20 µg/ml and to examine their molecular and cellular effect on PC-12 cells. At first, the toxicity of LED light at different power intensities, exposure times and incubation times is evaluated to find the optimal setting of LED light. Temperature assessment of LED-irradiated NPs proves the strong photothermal effect of NGF-SPIO-Au NPs and the temperature equilibrium is achieved after 25-30 minutes of heating. Therefore, we set 30 minutes as the duration time of LED treatment that is sufficient to stimulate neuronal activities via plasmonically-generated heat. The morphological evaluation of LED irradiated NGF-SPIO-Au NPs at the intensity of 1.90 mW/cm^2 on enhanced neuronal

differentiation and neurite growth of PC-12 cells is performed through quantitative analysis. Using calcium imaging and molecular analysis through the reverse transcription-polymerase chain reaction (RT-PCR) and western blot assay, we further examines how the LED-irradiated NGF-SPIO-Au NPs interact with the calcium level and proteins/genes related to neurite outgrowth and neural differentiation. For example, the neural specific marker, β3-tubulin protein is known as an essential element to form microtubules,[117] and the cell adhesive molecules, integrin β1 is important to the PC-12 cell attachment on substrate and the neurite extension.[118]

CHAPTER II

TUNABLE SPIO-AU CORE-SHELL NPS: SYNTHESIS AND

CHARACTERIZATIONS

In this chapter, we reported a facile synthesis of Au coated SPIO-core nanoparticles (NPs) with tunable shell thickness (1.5 nm to 8.8 nm). A synergistic seed growth method using citrate acid as a reducing agent was proposed to reduce Au3+ to Au at the surface of SPIO NPs (10 nm) that serve as original seeds. The thickness of Au coatings was tuned by moderating the composition of the reactants and other reaction conditions. This refined synthesis method facilities the easy tuning of plasmonic properties of SPIO-Au core shell nanomedicines to promote high light-to-heat conversion efficiencies, demanded by different hyperthermia treating conditions (discussed in chapter 3) Transmission electron microscope (TEM) images of the SPIO-Au NPs reveal the uniform quasi-spherical nanostructure and the absence of aggregation. The inductively coupled plasma mass spectrometer (ICP-MS) analysis demonstrates the successful formation of SPIO-Au NPs at predicted sizes and concentrations. UV-Vis light absorption spectra verify the slightly red shift of the surface plasmon resonance band with the increase of the thickness of Au coating.

Materials and methods

Materials

Hydrogen tetrachloroaurate (III) hydrate (HAuCl$_4$ •xH$_2$O) and sodium citrate were purchased from Sigma-Aldrich, USA. Water-based super paramagnetic iron oxide

(SPIO, γ-Fe_2O_3) nanoparticles (EMG-304) were purchased from Ferrotec. All chemicals were used as received without further treatment.

Synthesis of Au coated SPIO-core NPs

Briefly, SPIO-Au core-shell NPs were synthesized by the seed growth method[62,63] with sodium citrate as a reducing agent to form an Au coating on a SPIO core (10 nm) as shown in Figure 1(a). In this reaction, 0.02 mL of SPIO (EMG-304 (10 nm), Ferrotech, Santa Clara, CA) aqueous solution (0.931 M) was diluted to 3.724 mM by adding 4.98 mL of Deionized (DI) water and then sonicated for 5 minutes. 0.1 mL of diluted SPIO solution (3.724 mM) was then added into 30 mL of DI water and heated to 90°C under vigorous mechanical stirring. Next, 1.1 mL of 1% sodium citrate (Sigma-Aldrich, St. Louis, MO) and 0.5 mL of 1% $HAuCl_4$ (Sigma-Aldrich, St. Louis, MO) were sequentially added to the solution. During the reaction, the color of the solution changed from light brown to deep red in 30 min. Then, the resulting solution was used as a seed solution and the citrate reducing process was repeated again to produce a thicker Au coating, as shown in Figure 1(b), from left to right: sample size of 13 nm at 117 ppm, sample size of 19 nm at 103 ppm and sample size of 26 nm at 120 ppm. All the as-prepared SPIO-Au NP solutions were directly used for the characterization of NPs without further purification.
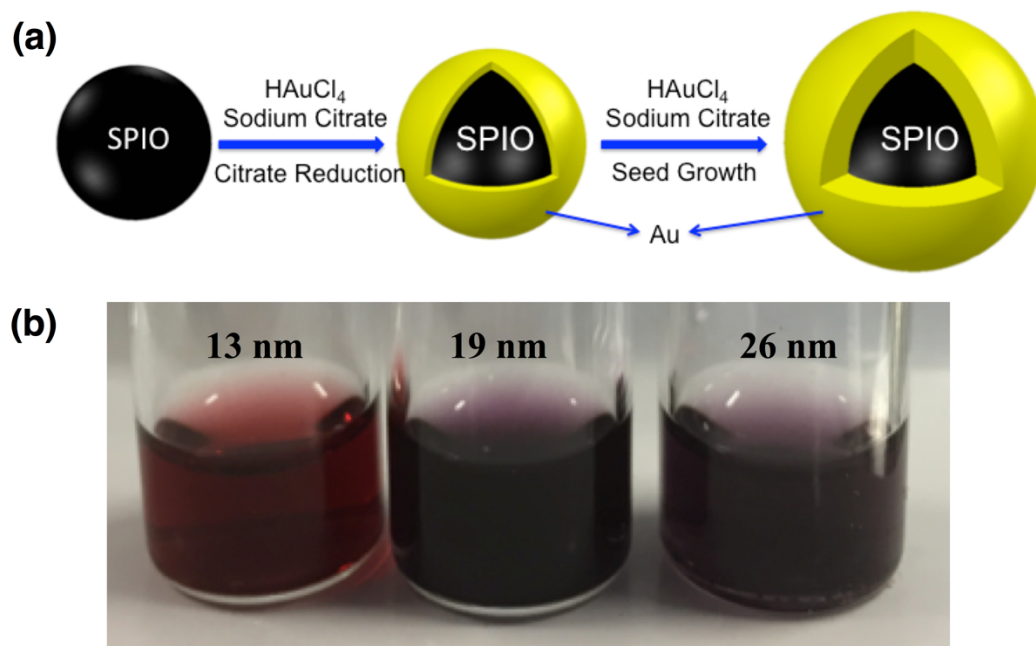
Figure 1. (a) Synthesis process of SPIO-Au NPs (b) Sample pictures

TEM imaging

The TEM imaging of as-synthesized SPIO-Au NPs was performed on a JEOL JEM 1400 Transmission Electron Microscope (TEM) at 120 kV operating voltage. 100 microliter droplets of each sample were dropped onto a 300-mesh copper grid (Ted-pella, inc.) and left to dry in air. Size distribution measurement as well as the calculation of average diameter and standard deviation is obtained based on at least 100 NPs from TEM images of each SPIO-Au NP sample.

Inductively coupled plasma mass spectrometer (ICP-MS) test

The samples were digested in mineral acid to bring Au and Fe into solution. 2% nitric acid was used as an analytical matrix for ICP-MS. In detail, the SPIO-Au NPs were digested by a mixture of HCl (0.3 mL, ~30%) and HNO_3 (1.1 mL, ~65%) under slow

heating. After the evaporation to near dryness, the samples were diluted into 2% nitric acid. Then the samples were tested on the Inductively Coupled Plasma Mass Spectrometer (Thermo-Finnegan Element2).

UV-Vis light absorption spectra

1 mL of each SPIO NP solution (10 nm diameter) or SPIO-Au NP solution (13, 15, 17, 18, 19, 21, 26, 27 nm diameter) at different concentrations were placed in a standard cuvette (1 cm) and the light absorption spectra were recorded at wavelengths between 350 nm and 900 nm at room temperature. As shown in Figure 2, the experimental setup consists of computer installed with Spectra Suite Software to record the absorption spectra via USB 4000 spectrometer (200-1000 nm, 3648 pixels), two QP600-1-SR-600 um Premium fibers (200-2000 nm), a CUV-UV cuvette holder with two 74-UV Collimating lenses (200-2000 nm) with a focus length of 10 mm, as well as a DH-2000-BAL tungsten halogen light source (210 nm – 2500 nm) with 74 UV collimating lens (200-2000 nm). All the measuring components were purchased from Optics Co.
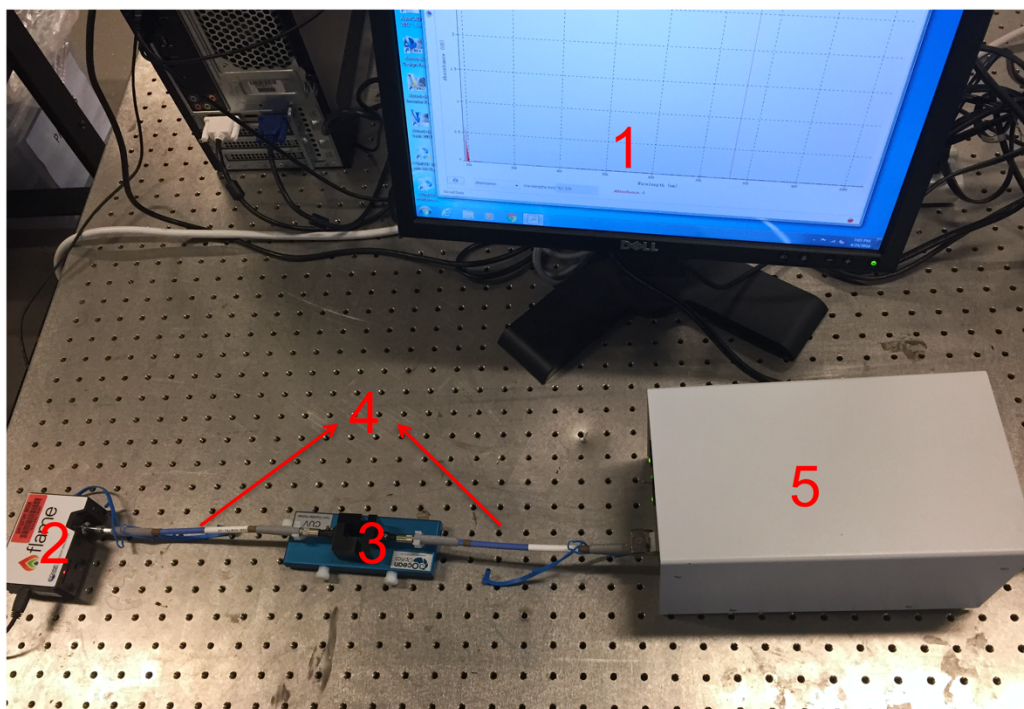
Figure 2. Experimental setup of UV-Vis light spectra test: 1) Computer with SpectraSuite software. 2) USB 4000 spectrometer, 3) CUV-UV cuvette holder with two 74-UV Collimating lenses 4) QP600-1-SR-600 um Premium fiber, 5) DH-2000-BAL tungsten halogen light source (210 nm – 2500 nm) with 74 UV collimating lens (200-2000 nm)

Stability examination

To examine the influence of the cell growth medium on the stabilities of NPs, the UV-Vis absorption spectroscopy and the zeta potential characterization were conducted. The solution of SPIO-Au NPs at the concentration of 80 μg/mL was suspended in MC3T3-E1 cell growth medium and in deionized (DI) water, respectively. At different time points, the light absorption spectra were recorded at wavelengths between 400 nm and 800 nm at room temperature with a FLAME-S-XR1-ES spectrometer and the SpectraSuite software

18

from Ocean Optics Inc. The zeta potential test was performed with a Malvern Zetasizer Nano ZS (Malvern Instruments Inc.) at 25 °C.

Results and discussion

Synthesis of Au coated SPIO-core NPs at different sizes and concentrations

In this study, the SPIO-Au core-shell NPs were synthesized by reducing Au^{3+} to Au at the surface of SPIO NPs that served as original seeds. The desired Au shell thickness was achieved by carefully controlling the Au: SPIO NP stoichiometric ratio and the repeating number of the coating procedure. A seed mediated growth strategy helps obtain higher NP concentrations after successive seeding aliquots; achieve the monodispersed NPs and enable incremental nano-shell increases for enhanced size control.[60]

Figure 3 shows the TEM image of SPIO-Au NPs of 13, 15,17, 18, 19, 21, 26 and 27 nm in diameter. The average particle diameter and standard deviation were calculated using Image J to measure the area of particles. The histograms showing size distribution over 100 NPs are depicted along with the TEM images. Narrow size distribution was obtained for each sample and uniform quasi-spherical morphology was observed through TEM images.
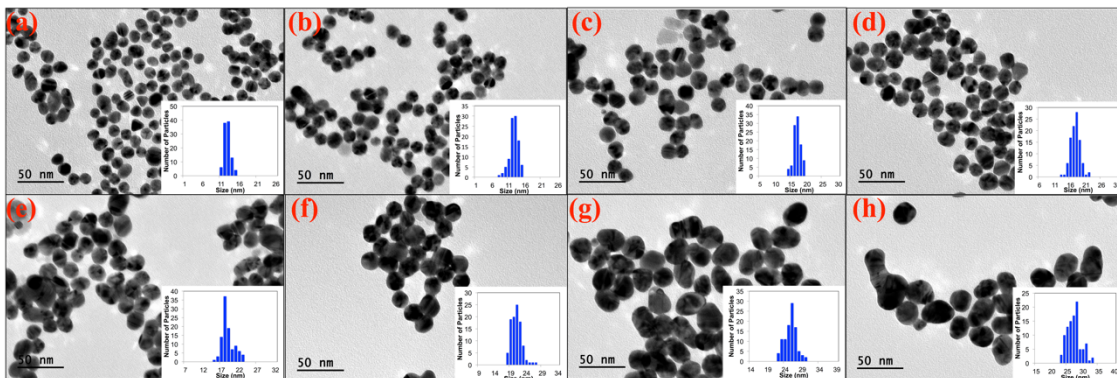
Figure 3. Nanosphere morphology and size distribution for Au-coated SPIO NPs of diameter (a) 13 nm (1.5 nm Au coating), (b) 15 nm (2.5 nm Au coating), (c) 17 nm (3.5 nm Au coating), (d) 18 nm (4 nm Au coating), (e) 19 nm (4.5 nm Au coating), (f) 21 nm (5.5 nm Au coating), (g) 26 nm (8 nm Au coating) and (h) 27 nm (8.5 nm Au coating). Histograms indicate size distribution for 100 NPs in total. Note narrow size distribution and uniform quasi-spherical morphology.

ICP-MS test of SPIO-Au NPs at different sizes and concentrations

The elemental concentration of Au and Fe for each SPIO-Au sample was measured through an Inductively Coupled Plasma Mass Spectrometer (ICP-MS) (Element 2 Finnigan MAT). The measured molar amounts of Au and Fe are listed in Table 1, which also summarizes the composition of reactants for different coating thickness. The measured average diameters of as-synthesized SPIO-Au NPs were 13, 15, 17, 18, 19, 21, 26 nm and 27 nm. Note that, M_est. indicates the estimated mass of Au according to the calculation from the molar amounts of the added seeds and the precursors for the reaction, M_ICP refers to the mass of Au measured from ICP-MS, D_ICP-MS refers to the predicted diameter from ICP-MS measurement using eq.1 by assuming the spherical shaper, and D_mea refers to the measured diameter from TEM.

$$r_{SPIO-Au}^3 = r_{SPIO}^3 + \frac{3}{4}\frac{m_{Au}}{\pi \rho_{Au} n_{SPIO}}$$ (1)

where m_{Au}, n_{SPIO}, and ρ_{Au} are corresponding to the mass of the Au, the number of SPIO particles and the density of Au, added for reaction. The measured diameters obtained from TEM images by using Image J software were lower than the predicted diameters due to the loss of Au during each experimental step. The measured molar amounts were achieved by ICP-MS test by measuring the elemental concentration of Au and Fe. The predicted diameter was calculated by using the measured molar amount of SPIO and Au. There is small discrepancy between the measured diameter using TEM and the predicted diameter using ICP-MS.

Table 1. Summary of composition of reactants for the synthesis of SPIO-Au NPs with varying average particle sizes.

Sample	SPIO/Au Mole ratio	n_SPIO (E13)	M_est (mg)	M_ICP (mg)	D_ICP (nm)	D_mea (nm)	Mass Concentration (ppt)
S13	0.026	1.141	0.968	0.392	16.4	13.1±1.5	117.4
S15	0.026	3.424	2.898	0.910	15.4	15.0±1.4	125.2
S17	0.010	0.685	2.898	0.652	21.8	17.3±1.2	251.0
S18	0.010	0.685	1.449	0.840	23.6	18.1±1.5	93.3
S19	0.017	1.141	2.417	0.155	13.3	19.3±1.7	103.0
S21	0.005	0.685	4.348	1.338	27.3	21.3±1.7	104.3
S26	0.005	0.685	4.348	1.802	30.0	26.1±1.7	119.8
S27	0.008	0.571	2.655	1.265	28.4	27.6±2.2	209.9

UV-Vis light spectra

The light absorption spectra of the SPIO NP seeds and the multifunctional SPIO-Au NPs with different coating thickness were measured by UV-Vis spectroscopy and plotted in Figure 4(a). The SPIO-Au NPs have a remarkable light absorption peak at

around 520 nm while the spectrum of pure SPIO NPs shows no peak in the range of 450-800nm, implying the formation of SPIO core-Au shell NPs. The surface plasmon resonance band of the SPIO-Au NPs shows a roughly red shift with the increase of the Au coating thickness, as shown in Figure 4(b) (from 1.5 nm to 8.8 nm of thickness), except the NPs at 13 nm and 21 nm, which may due to the possible local nonuniformity in the solution and the error of calculating diameter through TEM images.   These findings agree well with the statement that the surface plasmon resonance band exhibits a red shift when the size of the pure Au NPs is increased.[60] The fact that the spectra on SPIO-Au NPs with diameter from 13.1 nm to 27.6 nm own maximum absorption value at around 523 nm (which is close to the surface plasmon peak of pure Au NPs) indicated the uniform quasi-spherical structure and the absence of aggregation,[7,8,62] which is also supported by observing few precipitation of the solution over time.
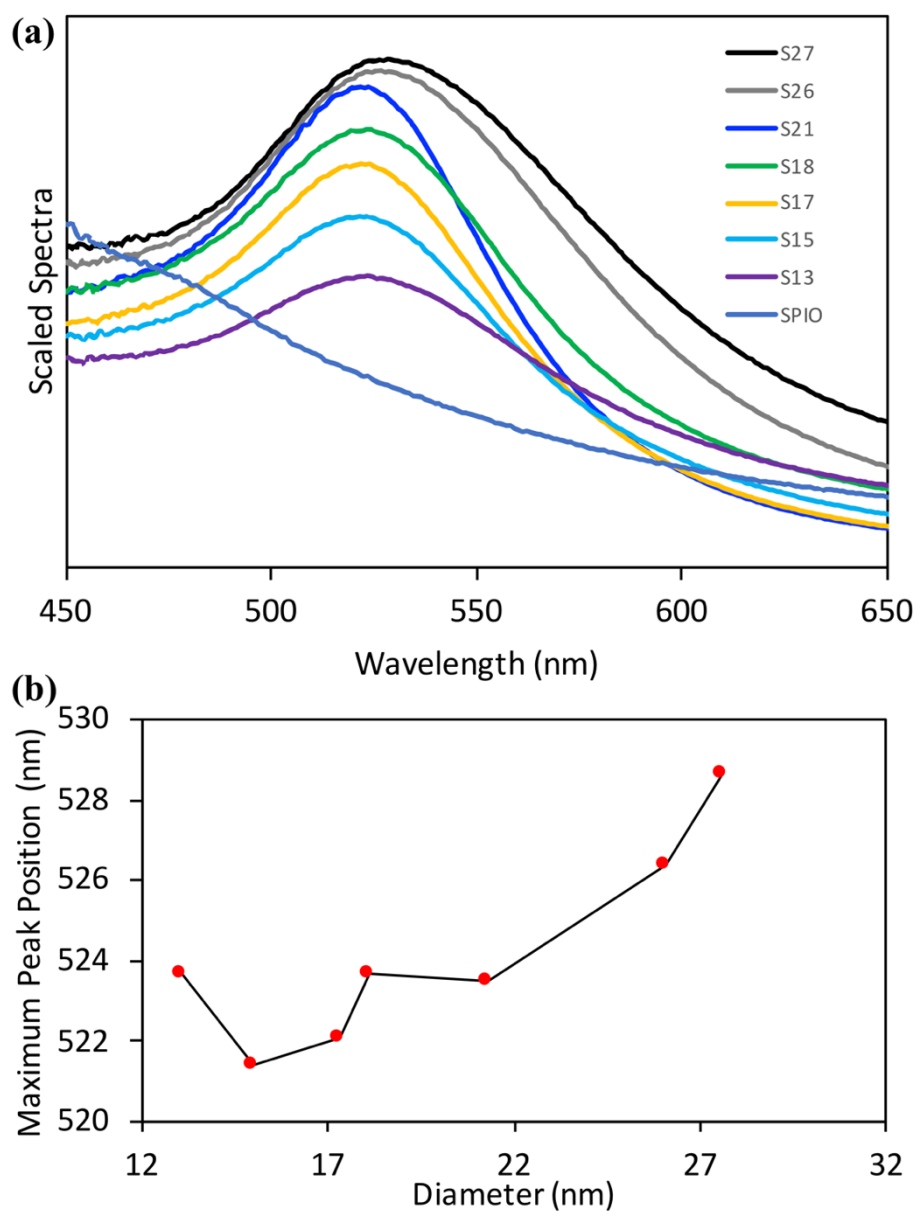
Figure 4. (a) UV-Vis absorption spectra of the SPIO NP seeds and the SPIO-Au NPs with different sizes (scaled to the same concentration). (b) the change of maximum peak position with different NP sizes

Stability of SPIO-Au NPs

In the cell growth medium, although a slight broadening of the peak with time is observed, no decrease of the absorbance peak is found even after 21 days (Figure 5(b)). Therefore, one can conclude that our SPIO-Au NPs are stable in both the cell growth medium and the DI water for up to 21 days. Interestingly, the absorbance peak shifted to 555 nm for NPs dispersed in the cell growth medium from that of 524 nm for NPs dispersed in the DI water, which is due to the optical effect of the cell growth medium, whose absorbance peak was found at 555 nm (Figure 5(c)). The measured zeta potential was changed from -31.7 mV (in DI water) to -11.9 mV (in cell growth medium), indicating the stability of NPs in the cell growth medium, due to the strong electrostatic repulsion between NPs arising from the negative charges. The change of zeta potential indicated the attaching of medium components with positive charges onto the NPs in the cell growth medium.[72]
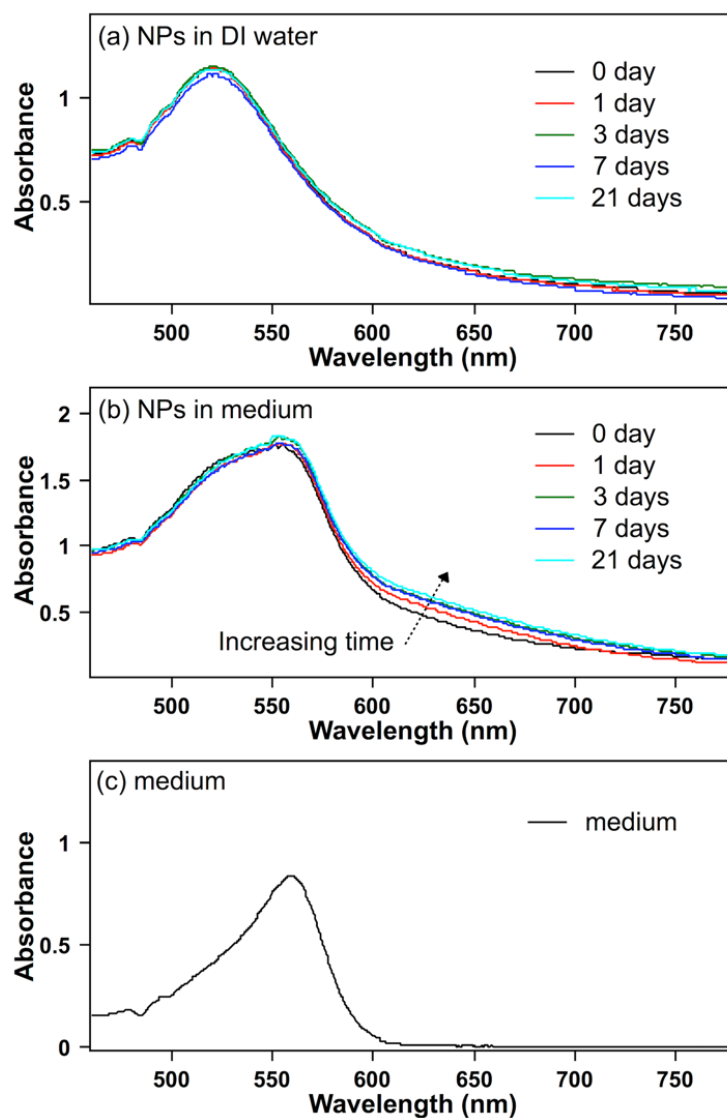
Figure 5. UV-Vis absorption spectra of SPIO-Au NPs (17.3 nm) at 80 μg/mL in (a) Cell growth medium for different time periods with a maximum absorbance at a wavelength of 553 nm and an obvious discrepancy of absorbance at a wavelength of 630 nm. (b) Deionized water for different time periods with a maximum absorbance at a wavelength of 520 nm (c) The spectrum of the cell growth medium only with a maximum absorbance at a wavelength of 560 nm, which explains the shift of the peak of the absorbance curve from (b) to (c).

CHAPTER III

SPIO-AU CORE-SHELL NPS: PHOTOTHERMAL CONVERSION EFFICIENCY

In this chapter, a new thermocouple (TC)-tip-exposing temperature assessment technique composed by the experimental measurement of temperature profile and the numerical modeling of the photothermal conversion efficiency is presented. The proposed technique is designed to evaluate the photothermal conversion efficiency of gold-coated superparamagnetic iron oxide nanoparticle (SPIO-Au NP) solution (26 nm, 12-70 ppm) at low continuous wave (CW) laser power (103 mW, 532 nm) irradiation in a very simple but accurate manner. In combination with the experimentally measured temperature profile, a finite element model (FEM) was developed to simulate the temperature rise of the NP solution at the very first 30 seconds from the starting point of the laser illumination. Experimentally measured parameters were embedded into the FEM simulation to predict the photothermal conversion efficiency of SPIO-Au NP solution which was close to the unity. The theoretical model (the ratio of absorbance/extinction) derived by the Mie theory also confirmed the near unity conversion efficiency of the as-synthesized SPIO-Au NPs. The key point of the proposed temperature assessment technique is to expose the TC tip in the center of the laser beam to ensure direct temperature measurement. In addition, the proposed technique was very straightforward, and largely reduce the complexity of the experimental set-up compared with traditional temperature assessment techniques. This technique provided a new promising strategy to evaluate the photothermal conversion efficiency of plasmonic NPs. And the lab-made SPIO-Au NPs are suggested to be the

potential nanomedicine with high photothermal conversion efficiency for high-performance laser surgery on well-controlled tumor cell removal.

Theoretical basis and methods

TC-tip-exposing temperature assessment technique

Referring to Figure 6(a) and 6(b), to measure the temperature profile of the NP solution a polystyrene (PS) semi-micro cuvette (12.5×12.5×45 mm outer dimensions) is filled with 0.5 mL of NP solution. An MGL-FN-532 (CNI Optoelectronics) CW laser provides a 1.5 mm radius (Where the intensity values fall to $1/e^2$ of the axial intensity value, e is the base of natural logarithm) Gaussian beam with a power of 103 mW that is directed horizontally through the middle of the liquid in the cuvette (cuvette inner depth: d=10 mm). A K-type TC-tip (Omega Engineering) with wires in 0.041 mm (0.0016 in) diameter and a bead diameter of 0.080 mm is placed in the geometric center ($x = 0, z = 0$) of the laser-illuminated liquid region approximately $y = 3$ mm from the inner cuvette wall facing the incident laser beam, to ensure that the temperature sensor and the heating laser were located in the same region of the liquid. The test is performed in ambient conditions (vacuum not required), and the temperature sensor is in direct contact with the heated NP solution. The temperature profile of the DI water and the NP solution at different concentrations were measured using this proposed TC-tip-exposing method under the excitation of a 532 nm CW laser.
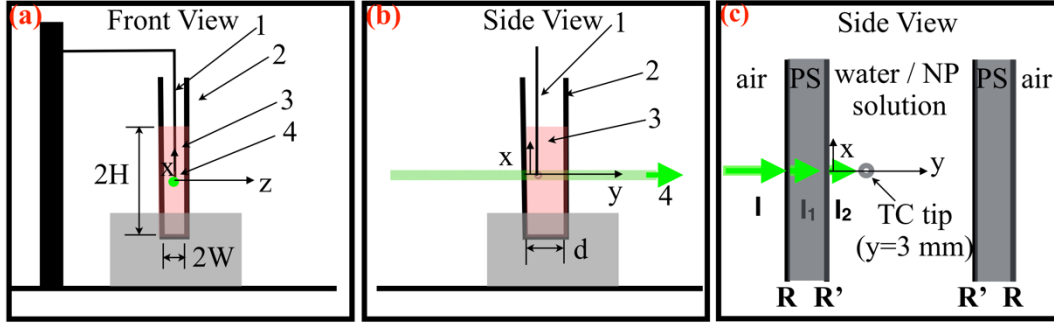
Figure 6. Experimental setup of the temperature profile measurement of SPIO-Au NP solutions. (a) Experimental setup (front view), (b) experimental setup (side view) (c) Detail of laser path through the cuvette containing DI water / NPs solution. Here (1) Thermocouple (Omega, Stamford, CT, K-type, 0.041 mm.); (2) BRAND polystyrene (PS) cuvette (1 cm by 1 cm); (3) SPIO-Au NPs solution (4) MGL-FN-532 (nm)-103 mW (PSU-H-FDA) laser.

Figure 6(c) showed how the 532 nm CW laser passes through the cuvette and the liquid. Here, I represented the axial incident laser intensity. I_1 is axial laser intensity inside the front wall of the cuvette, which is made of polystyrene (PS) and is 1 mm thick, and I_2 represents the axial laser intensity when the laser leaves the front PS wall and enters the liquid.

The refractive indices of the air, PS wall and water are n_{air}=1.00, n_{PS}=1.59, n_{water} =1.33, respectively. The reflectance between the air and the PS wall can be obtained from:

$$R = \left(\frac{n_{air}-n_{ps}}{n_{air}+n_{ps}}\right)^2 = 0.052 \tag{2}$$

while the reflectance between the DI water and the PS is:

$$R' = \left(\frac{n_{water}-n_{ps}}{n_{water}+n_{ps}}\right) = 0.008 \tag{3}$$

Then the intensities (I, I_1 and I_2 represent the maximum intensity at the center of the beam radius) in the PS wall and beginning of the liquid are:

$$I_1 = (1 - R)I \tag{4}$$

$$I_2 = (1 - R)(1 - R')I \tag{5}$$

Finite element simulation

Laser beam description

The incident laser beam is assumed to be Gaussian beam with a radius r_0=1.5 mm at which the laser intensity falls to $1/e^2$ of the axial laser intensity and propagates in the z direction. The incident laser intensity (W/cm^2) can be expressed as:

$$I(r) = I_0 e^{-2\left(\frac{r}{r_0}\right)^2} = \frac{2I_m}{\pi r_0^2} e^{-2\left(\frac{r}{r_0}\right)^2} \tag{6}$$

where $I_m = 103$ mW is the total incident laser power (mW) measured by a Coherent FieldMate laser power meter. I_0 is the axial laser intensity. In Cartesian coordinates the beam intensity becomes:

$$I(x, z) = \frac{2I_m}{\pi r_0^2} e^{\frac{-2(x^2 + z^2)}{r_0^2}}. \tag{7}$$

where the center of the laser beam is located at $x = 0, z = 0$ (the middle of the liquid as shown in Figure 6(a)), and the laser beam propagates along y direction.

A finite element model (FEM) was developed using COMSOL Multiphysics ® to simulate the temperature profile of SPIO-Au NPs irradiated under low laser power. The SPIO-Au NPs aqueous solution in the cuvette has dimensions $2W$ =4.5 mm, $2H = 23$ mm, and d=10 mm as shown in Figure 6(a) and (b)

The transient heat conduction equation is used to determine the time-dependent temperature history of the NP solution and the thermocouple:

$$\rho_i C_{p,i} \frac{\partial T_i}{\partial t} = k_i \left(\frac{\partial^2 T_i}{\partial x^2} + \frac{\partial^2 T_i}{\partial y^2} + \frac{\partial^2 T_i}{\partial z^2} \right) + \dot{Q}_i(x, y, z) \qquad (8)$$

where ρ is the density, C_p the specific heat, and k is the thermal conductivity, and $i = np$ for the NP solution and $i = tc$ for the thermocouple. (In the numerical solution the TC alloys are further distinguished between the chromel leg, the alumel leg and the bead.) The temperature $T = T(x, y, z, t)$ varies with both position and time.

The TC bead is modelled as a sphere of diameter 0.080 mm, with thermophysical properties k, ρ and C_p taken as the average of the corresponding properties for the chromel and alumel. The chromel leg extends vertically upward ($x > 0, z = 0$) and the alumel leg extends vertically downward ($x < 0, z = 0$).

The heating coefficient for the TC is determined by replacing the NP solution with DI water and measuring the transient laser heating. The DI water does not absorb the laser light, hence the only source of heating is the TC itself. The TC heating coefficient, β is adjusted in the model until model and data agree.

The boundary conditions are as follows. For the NP solution,

$$T_{np}(x, y, z, t) = T_\infty \quad \text{at} \qquad x = \pm W \qquad (9a)$$

$$T_{np}(x, y, z, t) = T_\infty \quad \text{at} \qquad z = \pm H \qquad (9b)$$

$$T_{np}(x, y, z, t) = T_\infty \quad \text{at} \qquad y = 0 \text{ and } y = d \qquad (9c)$$

where T_∞ is the ambient temperature.

For the TC, the boundary conditions are that the temperature and heat flux are continuous at the TC surface

$$T_{tc} = T_{np} \qquad (10a)$$

30

$$k_{tc}\frac{\partial T_{tc}}{\partial n} = k_{np}\frac{\partial T_{np}}{\partial n}$$

<div align="right">(10b)</div>

where the n is the direction normal to the TC at the point of interest.

The initial condition for the entire system is

$$T_i(x,y,z,t) = T_\infty \text{ at } t = 0.$$

<div align="right">(11)</div>

The thermodynamic properties for the NP solution and the thermocouple alloys chromel and alumel are shown in Table 2. Because the NP concentration is low, the NP solution properties for DI water are used.

<div align="center">Table 2. Thermal properties for analysis.</div>

Material	Density, ρ (kg/m³)	Thermal conductivity, k (W/m·K)	Specific Heat, C_p (J/kg·K)
NP solution	0.9982	0.6	4180
Chromel	8730	17.3	448
Alumel	8610	29.7	523

Heat-source terms

The volumetric heating source (W/m³) for the TC as a result of direct heating by the incident laser light is:

$$\dot{Q}_{tc}(x,z) = \beta I_2 e^{-\alpha\delta} e^{-2(x^2+z^2)/r_0^2}$$

<div align="right">(12)</div>

where $\delta = 3$ mm (TC tip position y = 3 mm) is the distance from the from the front cuvette wall through which the incident laser light enters to the TC tip location in the NP solution, α is the absorption coefficient obtained from the measured absorbance A: $\alpha = -\ln(10^{-A})/d$. The absorbance A was measured using a Flame miniature spectrometer (FLAME-S-XR1-ES, Ocean Optics Inc.) at a wavelength of 532 nm. β

<div align="center">31</div>

[1/m] is the proportionality factor above that is determined from the TC heating in DI water only.

The laser intensity in the NPs solution, after accounting for reflections in the front cuvette wall, is:

$$I(x, y, z) = I_2 e^{-\alpha y} e^{-2(x^2 + z^2)/r_0^2}. \tag{13}$$

The laser light is attenuated as it passes through the NP solution due to absorption and scattering, i.e., $\frac{dI}{dy} < 0$. The fraction of light absorbed, η, is the photothermal conversion efficiency, and contributes to the NP solution heating:

$$\dot{Q}_{np}(x, y, z) = -\eta \frac{dI}{dy} = \eta \alpha I_2 e^{-\alpha y} e^{-2(x^2 + z^2)/r_0^2}. \tag{14}$$

Results and discussion
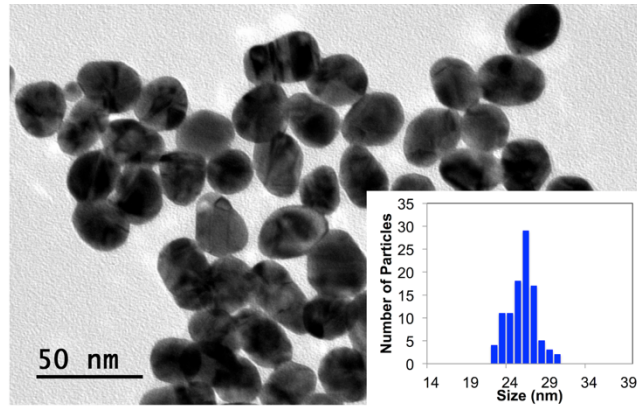
Figure 7. Morphology and size distribution for Au-coated SPIO NPs of diameter 26 nm (8 nm Au coating). Histogram indicates size distribution for 100 NPs in total. Note narrow size distribution and uniform quasi-spherical morphology.
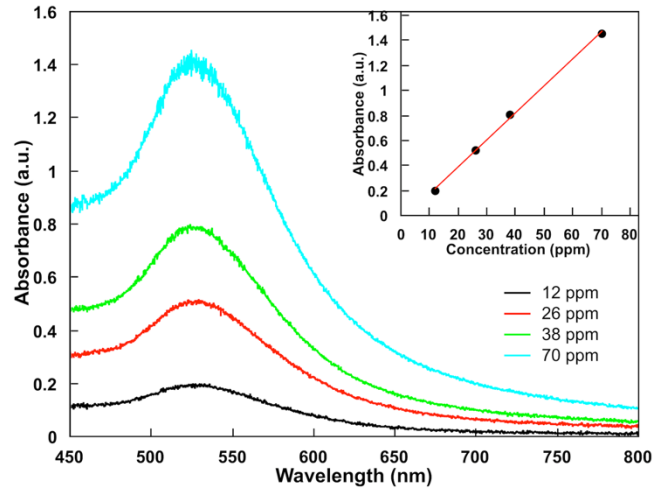
Figure 8. Light absorption spectra of the 26 nm SPIO-Au NP solutions indicating the peak absorbance value increased at higher concentrations (12, 26, 38, 70 ppm) and the insert indicating the linear relationship between the peak absorbance and the concentration.

Our SPIO-Au NPs were synthesized using the synergistic seed growth and citrate reducing method reported in previous work.[90,109] Figure 7 shows the transmission electron microscope image of the SPIO-Au NPs of 26 nm in diameter with quasi-spherical shape and narrow size distribution.

Figure 8 shows the absorbance vs. wavelength of the SPIO-Au NP solutions (26 nm) at different concentrations (12, 26, 38, 70 ppm) with the inset indicating the linear relationship between the absorbance and the concentration, agreeing well with Beer's law of absorption. The absorbance A and the corresponding absorption coefficient α of the NPs solutions at different concentrations at the wavelength of 532 nm are listed in Table 3. ($\alpha = 0$ for water only);

By comparing this FEM simulation with the temperature profile measurement, the photothermal conversion efficiency η of an unknown plasmonic NPs can be determined

33

using the following procedure: first, the temperature profile with the TC in DI water is measured, followed by a measurement with the NPs of interest. The temperature history during the first 30 seconds of the laser heating is recorded. The heat source equations (eq. 12 and eq. 14 with unknown η) are used to simulate the heating of the DI water and the NPs solution and calculate the temperature profile at one point located at the surface of the TC tip which is time-dependent. The value η is adjusted until the simulation matches with the measured temperature profile as closely as possible to determine the conversion efficiency η. Restricting the measurement time to 30 seconds is important to avoid energy loss from conduction through the cuvette walls and natural convection within the NP solution[119].

Table 3. α and A values for different concentrations of SPIO-Au NPs.

Concentration (ppm)	12	26	38	70
Absorbance, A	0.199	0.505	0.781	1.416
Absorption coefficient, α (1/m)	45.8	116.3	179.8	326.0

The temperature profile of the pure DI water and NPs at the concentration of 12, 26, 38 and 70 ppm were experimentally measured and are shown in Figure 9. Then the FEM model in COMSOL Multiphysics ® was utilized to simulate the temperature profile of the DI water only during the first 30 seconds from the starting point of the laser illumination. For this case, the heat source came from the TC tip only, thus $\dot{Q}_{np} = 0$. By

simulating the temperature profile of the DI water and comparing it with the experimental data, β was found to be 118,600 m^{-1}.

Next the simulation of the temperature profile with the NPs solution was performed. The numerical model was run with values of η ranging from 0 to 1. The goodness-of-fit parameter, R^2 was calculated, and η was adjusted to maximize R^2. The results are shown in Figure 9, and it can be seen that the simulated temperature history agrees very well with the experimental measurement within the first 30 s, indicating that our assumption of the heat conversion efficiency was valid for NPs at all concentrations. Table 4 lists the best-fit value of the photothermal conversion efficiency for each concentration and the corresponding value of R^2. It was found that in all cases, a photo conversion efficiency of unity ($\eta = 1.00$) yielded the best fit. This finding is in consistent with the literature[51] that ultra-small plasmonic NPs (~20 nm) have extremely low optical quantum yields (10^{-6}), and almost 100% of the photon energy is converted to heat.
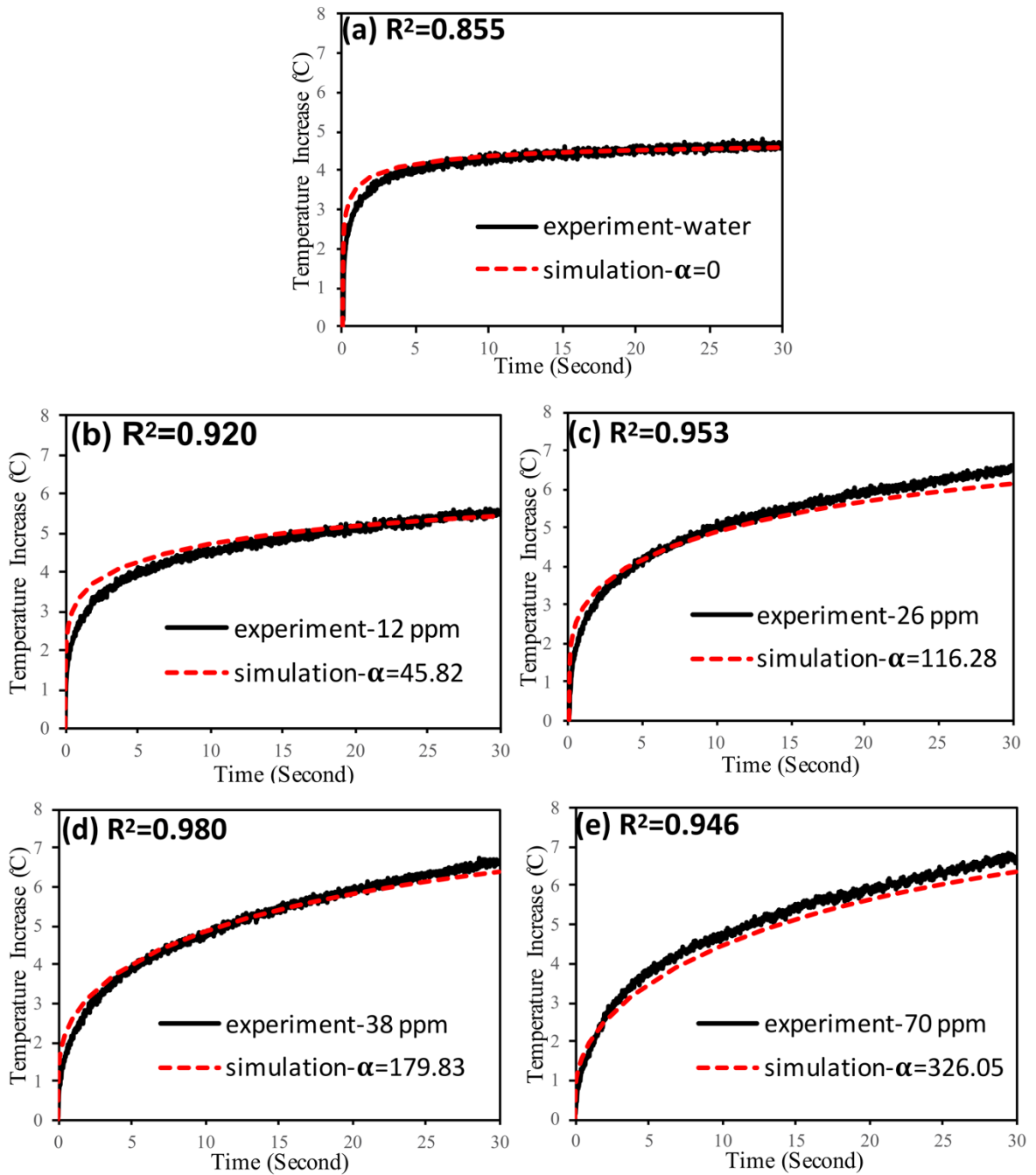
Figure 9. The comparison of measured temperature increases from experiments v.s. simulated temperature increases from the FEM modeling during the very first 30 seconds for (a) water (α = 0); (b) NPs solution at 12 ppm (α = 45.8 1/m); (c) NPs solution at 26 ppm (α =116.3 1/m); (d) NPs solution at 38 ppm (α= 179.8 1/m); (e) NPs solution at 70 ppm (α = 326.0 1/m); The value of R^2 represents how close the simulation results are to the experimental data, with higher values better.

Table 4. The photothermal efficiency for different concentrations of SPIO-Au NPs.

Concentration (ppm)	12	26	38	70
Photothermal conversion efficiency η	1.00	1.00	1.00	1.00
Coefficient of determination R^2	0.920	0.953	0.980	0.946

The scattering, absorption and extinction cross-sections of SPIO-Au core shell NPs with 26 nm diameter were studied by using a boundary element method proposed by Hohenester (MNPBEM toolbox).[120] The results were plotted in Figure 10 and the ratio of absorbance/extinction at the wavelength of 532 nm was calculated to be 0.987 (the absorbance cross section / the extinction cross section at 532 nm). This value was in agreement with the near 100% heat conversion efficiency, further confirmed the high accuracy of the simulation.
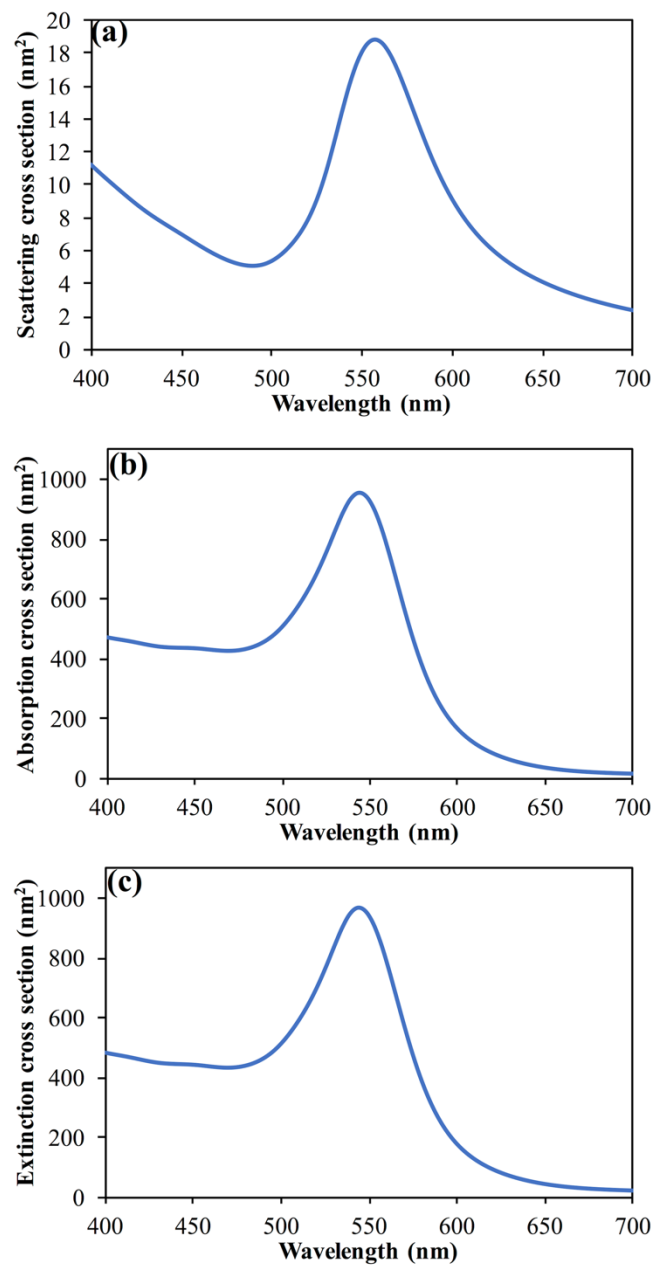
Figure 10. (a) Scattering cross section (10.87 nm^2 at 532 nm) (b) absorption cross section (831.53 nm^2 at 532 nm)   and (c) extinction cross section (842.40 nm^2 at 532 nm) for 26 nm SPIO-Au NPs (SPIO core diameter: 10 nm, Au shell thickness: 6.5 nm) calculated based on the MNPBEM toolbox

38

Compared with traditional temperature profile assessment methods reported in the literature,[1-3] this work incorporates an innovative experimental measurement technique with a FEM simulation, which provides several benefits. First, placing the TC tip in the center of the laser beam assures that the temperature sensor and the heating laser represent the same region in the liquid where the heating due to photothermal conversion occurs. Second, our method involves a fast and simple sample preparation using commercial hardware and can be done in ambient conditions in the laboratory. Third, by combining the experimental measurements with a high-fidelity FEM simulation, we only required the data of the temperature rise for the very first 30 seconds, avoiding the long-time laser heating to achieve the equilibrium temperature, which is time consuming and generated additional measurement errors due to conduction, natural convection, and evaporation of the water.

Conclusions

We have developed a novel direct-exposure technique for the measurement of nanoparticle solution photothermal coefficients. A thermocouple is immersed in the nanoparticle solution irradiated directly by a 3 mm diameter, 532 nm CW laser. The heat transfer equations for both the thermocouple directly and the surrounding nanoparticle solution are formulated and solved for using COMSOL Multiphysics® to simulate the temperature profile within the very first 30 seconds. Using the photothermal conversion coefficient as an adjustable parameter, very good agreement between the model and measurement are found. SPIO-Au NPs with uniform quasi-spherical shape and narrow size distribution were used in the development of the technique, and the photothermal

conversion affinity was found to be near unity, as expected from both predictions and

other investigations.

CHAPTER IV

ELECTROMAGNETIC STIMULATION USING DYNAMIC MAGNETIC FIELDS:

TOWARDS NEUROREGENERATION (PC-12 CELLS)*

Neuroregeneration imposes a significant challenge in neuroscience for treating neurodegenerative diseases. The objective of this study is to evaluate the hypothesis that the nerve growth factor (NGF) functionalized superparamagnetic iron oxide (SPIO)-gold (Au) nanomedicine can stimulate the neuron growth and differentiation under external magnetic fields (MFs), and dynamic MFs outperform their static counterparts. The SPIO-Au core-shell nanoparticles (NPs) (Diameter: 20.8 nm) possessed advantages such as uniform quasi-spherical shapes, narrow size distribution, excellent stabilities, and low toxicity (viability >96% for 5-day). NGF functionalization has enhanced the cellular uptake. The promotion of neuronal growth and orientation using NGF functionalized SPIO-Au NPs, driven by both the static and dynamic MFs, was revealed experimentally on PC-12 cells and theoretically on a cytoskeletal force model. More importantly, dynamic MFs via rotation performed better than the static ones, i.e., the cellular differentiation ratio increased 58%; the neurite length elongation increased 63%.

Methods

Synthesis of SPIO NPs

SPIO (Fe_2O_3) NPs were synthesized by the co-precipitation method.[7,62] Briefly, 2.81 g $FeCl_3*6H_2O$ and 1.0 g $FeCl_2*4H_2O$ were dissolved in a solution containing 1.03 g of 37% HCl in 12.5 ml of deionized (DI) water. The solution was added dropwise to 125 ml of 1.5 M NaOH solution with vigorous stirring. Then the formed black precipitate was isolated by magnetic decantation and washed 3 times with DI water, followed by dispersing the resulting Fe_3O_4 NPs in 125 ml of 0.01 M HNO_3 solution and heating the solution with stirring at 90°C for 30 min to oxidize the NPs. The resulting SPIO NPs were washed twice with DI water and dispersed in 125 ml of 0.1 M TMAOH.

Synthesis of SPIO-Au NPs

The 0.5 ml of as-synthesized SPIO NPs (60 mM) were sonicated and diluted to 1.5 mM with 19.5 ml of DI water. Then 5.5 ml of the diluted SPIO NPs was mixed with 5.5 ml of 0.1 M sodium citrate and stirred for 10 min to exchange the absorbed OH^- with citrate anions. Then the solution was diluted to 100 ml using DI water and followed by the addition of 0.5 ml of 1% $HAuCl_4$ solution to the mixture. The pH of the solution was adjusted to 8.86 by using 0.1 M NaOH solution. Then 0.6 ml of 0.2 M $NH_2OH*HCl$ was added to the mixture to form the Au coating. The color of the mixture was changed from brown to purple to pink-red in several minutes, which indicated the successful formation of the Au shell. Finally, the NPs was separated and washed by magnetic decantation. The as-prepared SPIO-Au NPs dispersed in 10 ml of DI water were directly used in the following experiments without any further purification. The concentration of the SPIO-

Au NPs was 422 µg/ml (including 68.7% of Au in mass) (Table A1, Appendix A). All the aforementioned chemicals were purchased from Sigma-Aldrich (St. Louis, MO) unless otherwise states.

Functionalization of SPIO-Au NPs

NGF-β (N2513, Sigma) was labeled with Alexa Fluor 488 (A10235, Invitrogen) according to the manufacturer's protocol. The labeled protein was purified through a size exclusion purification resin to separate the unincorporated dye. The functionalization of the SPIO-Au NPs was performed by adding 14 µg of the labeled protein to 0.47 ml of 422 µg/ml SPIO-Au NPs (NGF: NPs = 1:14 in mass). The suspension was stirred for 3 h at room temperature. The resulting mixture was washed 3 times and the free NGF was removed using magnetic separation. Finally, the functionalized NPs was re-dispersed in 1 ml of DI water. To estimate the amount of NGF bounded to SPIO-Au NPs, the absorbance of the supernatant from the previous step was first measured at the absorbance peak of 280 nm (NGF). And then the concentration of free NGF was calculated by using a calibration curve showing the absorbance of a series of solutions with known NGF concentration. By subtracting the amount of free NGF, the final composition of 198 µg/ml of SPIO-Au NPs (68.7% Au in mass) and 11.15 µg/ml of NGF was achieved.

Characterization of SPIO-Au NPs

To observe the morphology of the synthesized SPIO-Au NPs, the transmission electron microscopy (TEM) imaging was performed on a JEOL JEM 1400 microscope at an operating voltage of 120 kV. Briefly, 100 µL droplets of each sample were dropped onto a 300-mesh copper grid (Ted Pella Inc., Redding, CA) and then left to dry in the air.

The functionalization of SPIO-Au NPs was characterized by zeta-potential measurement using Zetasizer Nano ZS (Malvern Instruments Inc., Westborough, MA). The measurements were repeated 3 times and the results were expressed using average values and standard deviations.

PC-12 cell culture

PC-12 cells (from rat pheochromocytoma) obtained from American Type Culture Collection (ATCC) were cultured in ATCC modified RPMI-1640 medium supplemented with 10% heat inactivated horse serum (HS), 5% fetal bovine serum (FBS) and 1% penicillin–streptomycin (medium and supplements were purchased from Gibco, Grand Island, NY). Cells were cultured in poly-L-lysine (PLL, P4707, Sigma-Aldrich, St. Louis, MO) coated Petri dishes in a humidified incubator under a 5% CO_2 atmosphere at 37°C. To induce cell differentiation, PC-12 cells were incubated in serum reduced media (1% heat inactivated HS and 0.5% FBS).

Cell viability evaluations- Trypan blue exclusion assay and CCK-8 assay

To examine the cytotoxicity of SPIO-Au NPs, PC-12 cells were seeded into 24-well plates coated with PLL and incubated for 1 day. Then the cells were washed with Dulbecco's phosphate-buffered saline (DPBS) and incubated with SPIO-Au NPs at different concentrations (Groups: 0.7 μg/ml NGF, 10 μg/ml NPs, 0.2 μg/ml NGF-SPIO-Au NPs, 1 μg/ml NGF-SPIO-Au NPs, 5 μg/ml NGF-SPIO-Au NPs and 10 μg/ml NGF-SPIO-Au NPs). After 1, 3 and 5 days, the cells were dislodged from the dish, centrifuged and dispersed in growth medium. Cells were then stained with 0.4% Trypan blue solution (Gibco, Grand Island, NY) and examined through a hemocytometer (Bright-Line™ and

Hy-Lite™ Counting Chambers, Hausser Scientific, PA). Cell cultured without NPs or NGF were used as control.

The CCK-8 cell counting kit (Sigma-Aldrich, St. Louis, MO) was used to evaluate the effect of SPIO-Au NPs on cell proliferation. PC-12 cells were seeded into PLL coated 96-well tissue culture plates at a density of $2*10^3$ cells/well with growth medium. After 24 h of incubation, the medium was replaced by fresh medium containing SPIO-Au NPs and (or) NGF (groups: 0.7 µg/ml NGF, 10 µg/ml NPs, 0.2 µg/ml NGF-SPIO-Au NPs, 1 µg/ml NGF-SPIO-Au NPs, 5 µg/ml NGF-SPIO-Au NPs and 10 µg/ml NGF-SPIO-Au NPs). Cells without NPs were seeded as a control group. After 1 and 3 days of incubation, the media were replaced with fresh media and 10 µL of CCK-8 solution was added to each well and followed by the incubation of the plates for 2h at 37 °C. The absorbance was measured using a microplate reader (SpectraMax i3x, Molecular Devices Inc.) at the wavelength of 450 nm.

Cellular uptake TEM analysis

To study the cellular uptake of SPIO-Au NPs, PC-12 cells were seeded onto an Aclar® (Electron Microscopy Sciences Inc.) film in a 12-well plate at a density of $2*10^5$ cells per well and incubated with growth medium containing SPIO-Au NPs and NGF-SPIO-Au NPs at the concentration of 10 µg/ml. After 24 h of incubation, cells were prefixed in 3% Electron Microscopy grade glutaraldehyde in 0.1 M PBS, pH 7.4 at room temperature for 1 h. Cells were then fixed in 1% osmium tetroxide in 0.1 M PBS, pH 7.4. Followed by the dehydration in a graded series of ethyl alcohol and embedded in Durcupan resin (Sigma-Aldrich, St. Louis, MO). Ultrathin sections (80 nm) were cut with a Leica

EM UC7 Ultramicrotome (Leica Microsystems Inc.) and collected on formvar coated copper slot grids. Then these sections were stained with uranyl acetate and lead citrate and then analyzed by using a FEI Tecnai12 BioTwinG^2 microscope with an AMT XR-60 CCD digital camera system, at an accelerating voltage of 80 kV.

Neurite growth under dynamic MFs

To compare the cytoskeletal influence of dynamic MFs with static MFs, two identical magnetic applicators were printed on a MakerBot Replicator using a polylactic acid (PLA) filament. One applicator was used to generate static MFs. The other was installed on a rotating platform to generate dynamic MFs (Figure 11 (a) and (b)), where a Petri dish was mounted on a Tower Pro MG90S Micro Servo controlled by an Arduino Uno R3 Microcontroller A000066. The dish was rotated at 24 revolutions (45°) per minute during the test. Cells were seeded at the density of $2*10^5$ cells/dish in PLL pre-coated Ibidi Petri dishes (D: 35 mm). After 24 h, the medium was replaced by fresh serum reduced medium containing NGF-SPIO-Au NPs at the concentration of 10 μg/ml. Cells were incubated for 24 h to let the NPs to interact with cells. Then the Petri dish was put inside each magnetic applicator. Three groups of cells were prepared (control, static and dynamic). After 1 day, a light microscope (Axiovert 200M Inverted Fluorescence/phase Contrast Microscope (Carl Zeiss Inc.) equipped with an AxioCam CCD camera) was used to capture the images of differentiated cells. For each group, at least 40 pictures were acquired, and more than 4000 cells were quantified. The neurite angle, length and number in each image were measured using Simple Neurite Tracer as a plugin of Fiji.
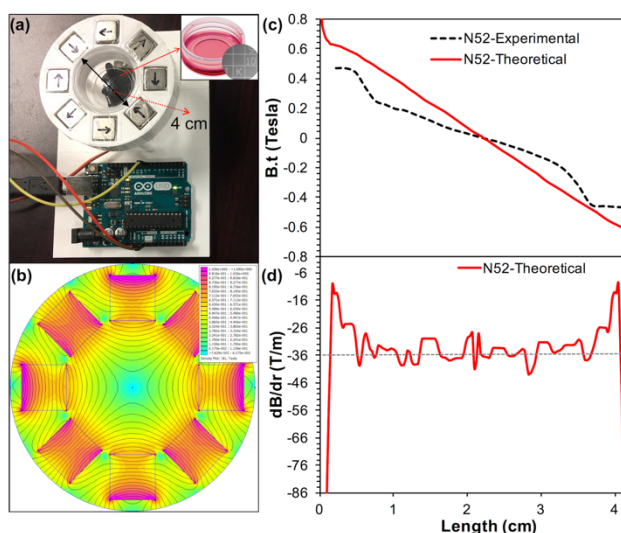
Figure 11. Set-up of the dynamic MFs. (a) The magnetic applicator using N52 magnets and the rotating platform. Inset: The Ibidi Petri dish (b) FEM of the N52 magnetic applicator; (c) FEM result (theoretical) and the experimental measurement of the flux density distribution inside the N52 Halbach-like magnetic applicator. (d) The derivative dB/dr (T/m) along the radial direction. The dot line in (d) represents the average value of dB/dr, which is -36.19 T/m. Reprinted with permission from reference 90.

Statistical analysis

All results were analyzed based on at least 3 independent experiments and expressed using the standard deviation. Statistical analysis was performed by the Mann–Whitney U test and the one-way analysis of variance with Tukey post hoc test. Each group treated with SPIO-Au NPs was compared with the control group. P value less than 0.05 was considered as a significant difference.

Results

Characteristics

The TEM images showed the synthesized SPIO cores (Figure 12(a)) (D: 13.2 ± 2.5 nm) before the coating process, and SPIO-Au NPs (Figure 12(b)) (D: 20.8 ± 2.7 nm)

with a quasi-spherical shape and a narrow size distribution. The light absorbance spectrum showed the peak of Au around 524 nm, confirming the existence of Au coating (Figure 13(a)). The as-synthesized SPIO-Au NPs were then conjugated with Fluor 488 labelled NGF through Au-amine (NH_2) linkage (covalent bond)[121] The UV-Vis measurement showed the typical absorbance peak of NGF protein and Fluor 488 at 280 nm and 494 nm respectively (Figure 13(b)). The functionalization of SPIO-Au NPs with NGF was characterized by zeta potential measurement (Figure 13(c)). The initial zeta potential of SPIO-Au NPs before the functionalization of NGF was -33.2 mV, reflecting the high stability of colloidal SPIO-Au NPs by strong electrostatic repulsion,[122] while it dropped to -25.1 mV with the addition of NGF (SPIO-Au: NGF = 1:0.005 in mass), which confirmed the successful functionalization of NGF with NPs. The zeta potential of NGF-SPIO-Au NPs increased towards the isoelectric point with higher NGF/SPIO-Au mass ratio, revealing that more of the NGF factors were bounded to SPIO-Au NPs and the saturation point was not reached in the tested range. It is also mentioned in the literature that the zeta potential changes to less negative values with increasing counter ion size.[123] Adversely, the hydrodynamic diameter decreased, this may due to the partial removal of the original citrate ligand from the ligand shell, as more of the NGFs were added to the solution, more of the citrate ligand were detached from the NPs surface and replaced by the NGF to attach to the surface of the SPIO-Au NPs. It is interesting to notice that the molecular weight of NGF (53036 kDa (1 Da= 1 g/mol) is much larger than the molecular weight of citrate acid (189.09 g/ml) and therefore more efficient shielding of the NGF was achieved to protect SPIO-Au NPs from aggregation which resulted in the formation of

smaller clusters of NPs, and therefore the hydrodynamic diameter decreased. The similar

phenomenon is observed in literature as well.[123]
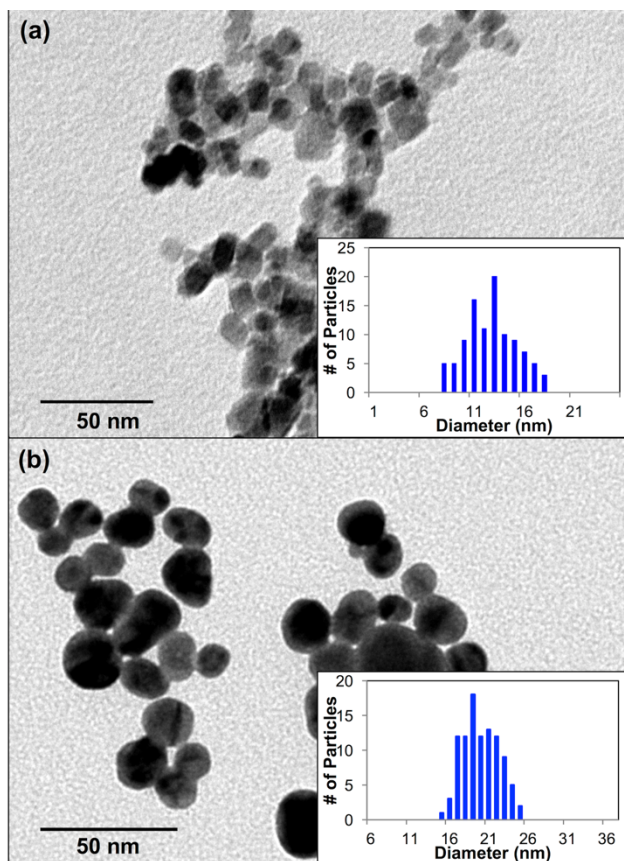
Figure 12. TEM images of the NPs. (a) SPIO NPs; (13.2 nm) (b) SPIO-Au NPs (20.8 nm). Reprinted with permission from reference 90.
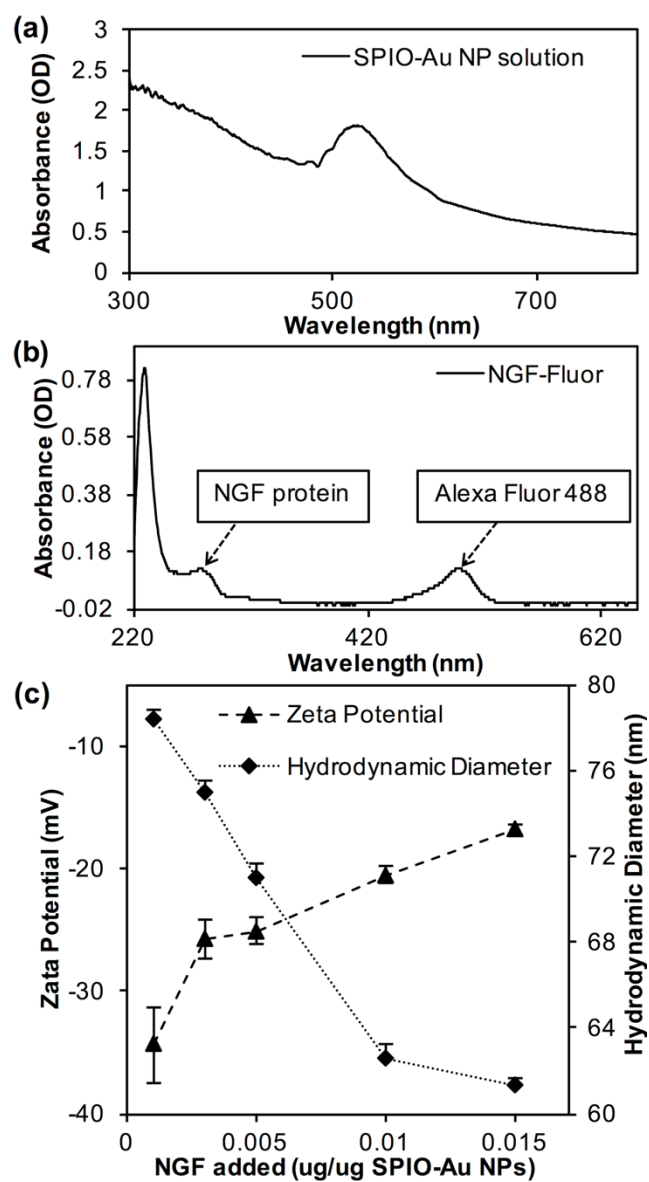
Figure 13. Light absorbance and zeta potential measurement. The UV-Vis spectrum of (a) SPIO-Au NPs and (b) NGF-Fluor. (c) Zeta potential of SPIO-Au NPs and hydrodynamic diameter at different NGF/NPs ratio (by adding different amount of NGF to the same concentration of SPIO-Au NPs). Reprinted with permission from reference 90.

Cell viability evaluation

To reveal how SPIO-Au NPs affect the *in-vitro* cellular viability, the Trypan blue exclusion assay was performed on PC-12 cells treated with NGF (0.7 μg/ml), NPs (10 μg/ml) and NGF-NPs at the concentrations from 0.1 to 10 μg/ml. For up to 5 days of incubation, no significant reduction of live cells to total cells ratio was observed for all the concentrations compared with the control group. Interestingly, there was a significant increase of the viability for groups treated with NGF, NPs and NGF-NPs at 5 days of incubation (Figure 14(a)). To further explain this phenomenon, the cell proliferation test using the CCK-8 colorimetric assay was performed. The absorbance of the formazan dye generated by the dehydrogenases activities in cells was recorded for each group, which was proportional to the number of live cells.[124] A stimulated proliferation (% of control group) was observed for groups treated with NGF, NPs and NGF-NPs. In particular, groups treated with NGF (184% of control, 7 days), NPs (166% of control, 7 days) and NGF-NPs (>163% of control, 7 days) had higher proliferation rate than the control group. And the proliferation rate was significantly improved with the increasing concentration of NGF-SPIO-Au NPs for up to 7 days of incubation. This increase explained why their viability from trypan blue assay also increased compared with the control group as more viable cells were proliferated relative to dead cells. (Figure 14(b))
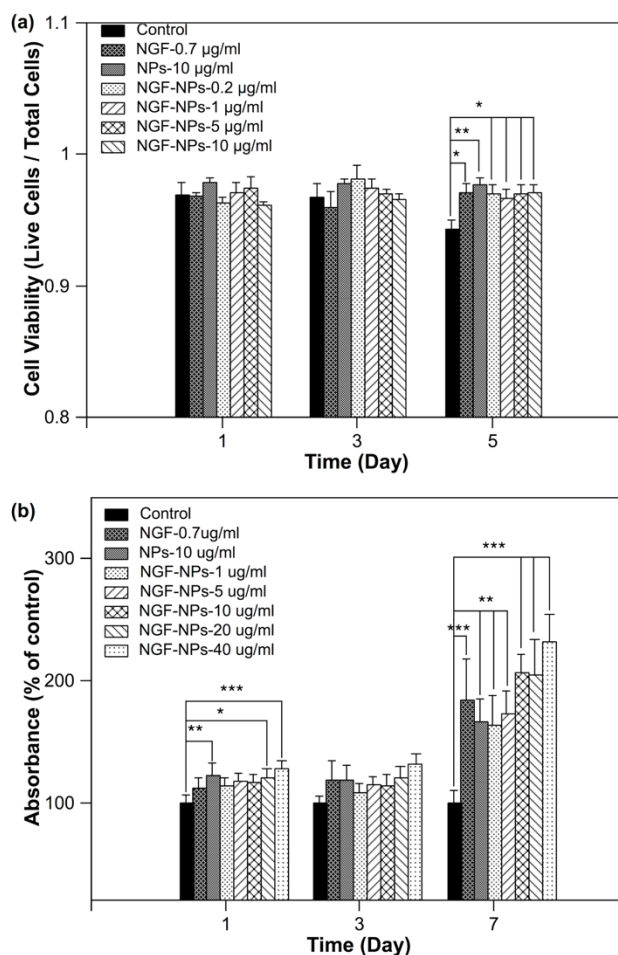
Figure 14. Cell viability evaluation. (a) The viability results from Trypan Blue staining. (b) The absorbance results from CCK-8 cell counting kit. The addition of NPs and NGFs significantly improve the cell proliferation for up to 7 days of incubation. Reprinted with permission from reference 90.

Cellular uptake of NPs: TEM analysis

The cellular uptake of NPs and NGF-NPs at the concentration of 10 μg/ml was examined by TEM analysis on PC-12 cells incubated for 24 h (Figure 15). TEM images showed the successful internalization of NPs, locating inside the endosomal vesicles in the cytoplasm, rather than in the nucleus. The cytoplasmic membranes remained intact for both of the groups. For the cells treated with NGF-SPIO-Au NPs, the large clusters of NPs

52

were found inside each cell with some of the clusters of NPs located at the cell membrane which engulfing the NPs (Figure 15(d)), implying the cellular uptake through endocytosis. While for the cells treated with SPIO-Au NPs only, some free individual NPs were found in the cytoplasm, which were more likely to penetrate into the cell membrane by direct diffusion as no SPIO-Au NPs were found to be attached to the cytoplasmic membrane, since NPs usually need to be absorbed to the cell membrane for endocytic internalization.[59]
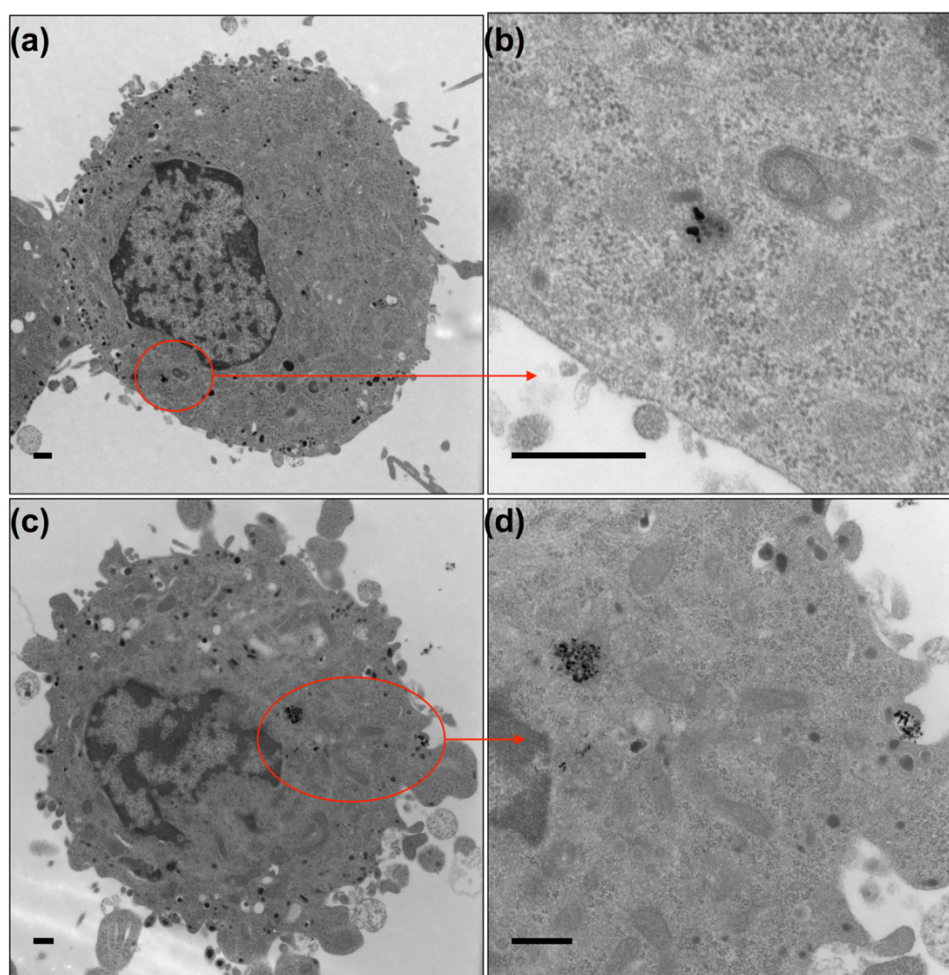
Figure 15. TEM images to show the cellular uptake of PC-12 cells. (a) and (b): PC-12 cells treated with NPs only; (c) and (d): PC-12 cells treated with NGF-NPs. (b) and (d) are enlarged images of areas shown inside the dashed circles in (a) and (c). Scale bar = 500 nm. Reprinted with permission from reference 90.

The morphology analysis-neuron growth and differentiation under static and dynamic

MFs

To demonstrate our hypothesis that the NGF-SPIO-Au NPs can stimulate the neuronal growth and differentiation under external MFs, and the dynamic MFs outperform the static ones, PC-12 cells treated with NGF-SPIO-Au NPs (10 μg/ml) were cultured and placed in a dynamic magnetic applicator composed by eight of N52 NdFeB magnetic cubes of 0.5 inch arranged in a Halbach array (Figure 11 (a) and (b)) and a static magnetic applicator with the same magnetic configuration. In this setup, the magnetic strength along the diameter of the magnetic applicator was simulated from finite element modelling (FEM) and then experimentally measured using a F.W. Bell 8010 gauss/tesla meter (Figure 11 (c)), which was in agreement with the theoretical simulation. An average MF gradient of -36.19 T/m was calculated from the FEM result (Figure 11 (d)). In this test, we visualized the morphology of differentiated cells using bright field microscopy (Figure 16). Then the Fiji software was used to trace neurites for control (no MF: 1 Day-control-MF-), static (with static MFs: 1 Day-N52-static-MF+) and dynamic groups (with dynamic MFs: 1 Day-N52-dynamic-MF+). To quantify the orientation of neurite, the angle θ between the neurites and the direction of the magnetic force (radial outward direction) was measured and the orientation index was defined as $O_i = \cos\theta$ ($0 < \theta < \pi$, $O_i \sim 1$ for neurite along the magnetic force direction).
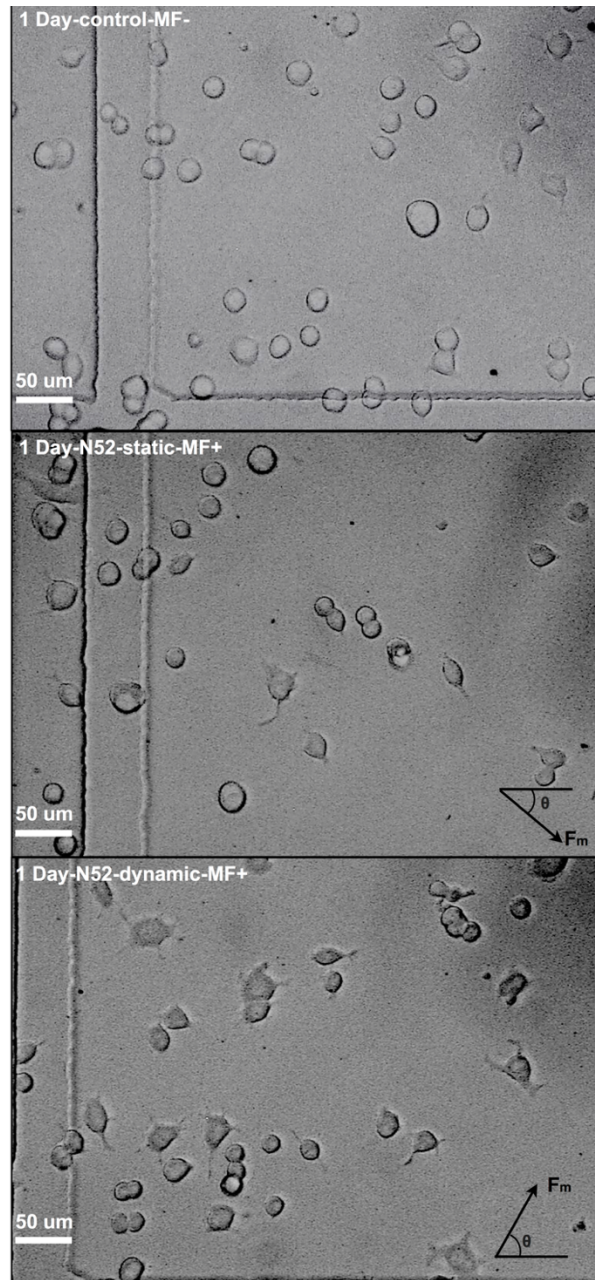
Figure 16. Bright field microscopy images. PC-12 cells were treated with 10 μg/ml NGF-SPIO-Au NPs (a) without MF, (b)with static and (c) with dynamic MF for 1 day of incubation. Reprinted with permission from reference 90.

As the results of analysis, after 1 day of magnetic treatment, both of the static (130%) and rotation (206%) groups showed a significant increase for the ratio of

differentiated cells compared with the control group which had no magnetic treatment. Moreover, the dynamic group had much higher ratio (~158%) than that of the static group (Figure 17(a)). The dynamic group also showed a significantly increased number of neurites per differentiated cells (117% of control) (Figure 17(b)). Both of the static (114% of control) and dynamic (187% of control) groups exhibited longer average neurite length. noticeably the average neurite length of the dynamic group was 63% longer than that of the static group (Figure 17(c)). The distribution of angles between the neurite and the magnetic force (0°) showed that the neurites preferentially aligned along the direction of the magnetic force (Oi=0.20 for the static group and Oi=0.14 for the dynamic group), while in the control group without MFs, the neurites showed a homogeneous distribution with no preferred directions (Oi= 0.01, the arbitrary axis was chosen as there was no magnetic field for control group) (Figure 18 (a), (b), (c) and (d)). To analyze how the MF affected the neurite outgrowth, the neurite length (normalized with control) was compared for different MF configurations at different ranges of angle relative to the direction of the magnetic force. It was shown that under the dynamic MFs, the average neurite length was much higher than the group with static MFs at the angle between 0° and 50° (Figure 18(e)).
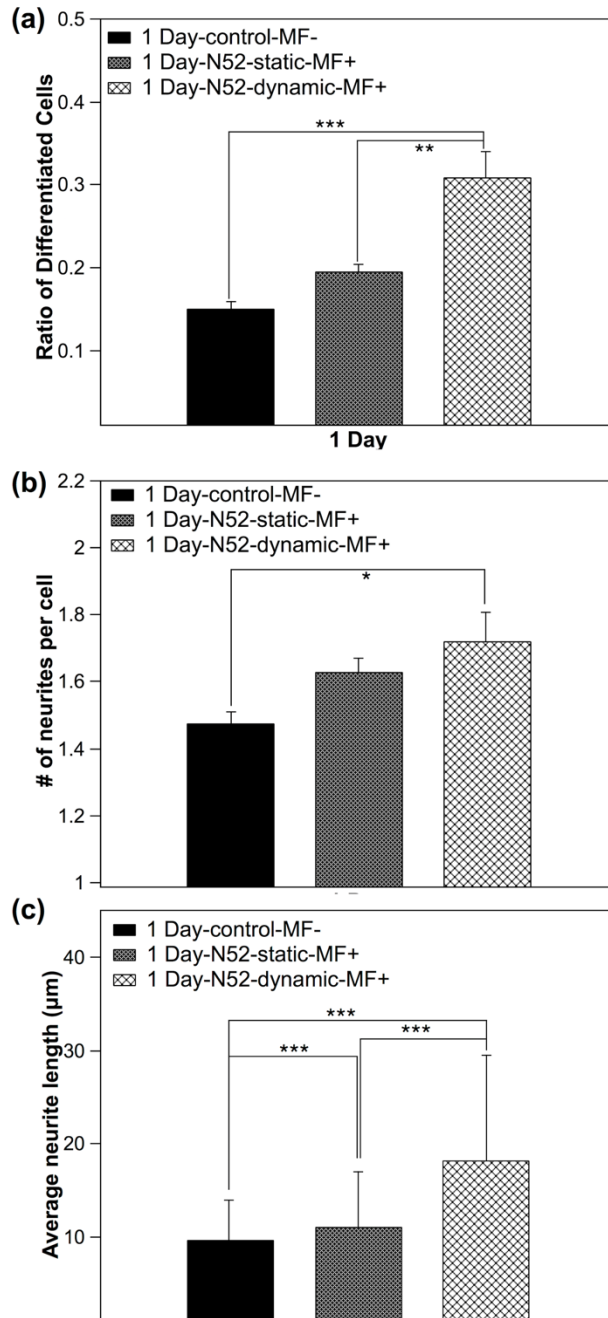
Figure 17. Morphology analysis for PC-12 cells treated with and without dynamic MFs. (a) Percentage of differentiated neuronal phenotype cells (b) Number of neurites per cell (c) Average neurite length; *p < 0.05; **p < 0.01; ***p < 0.001. Reprinted with permission from reference 90.
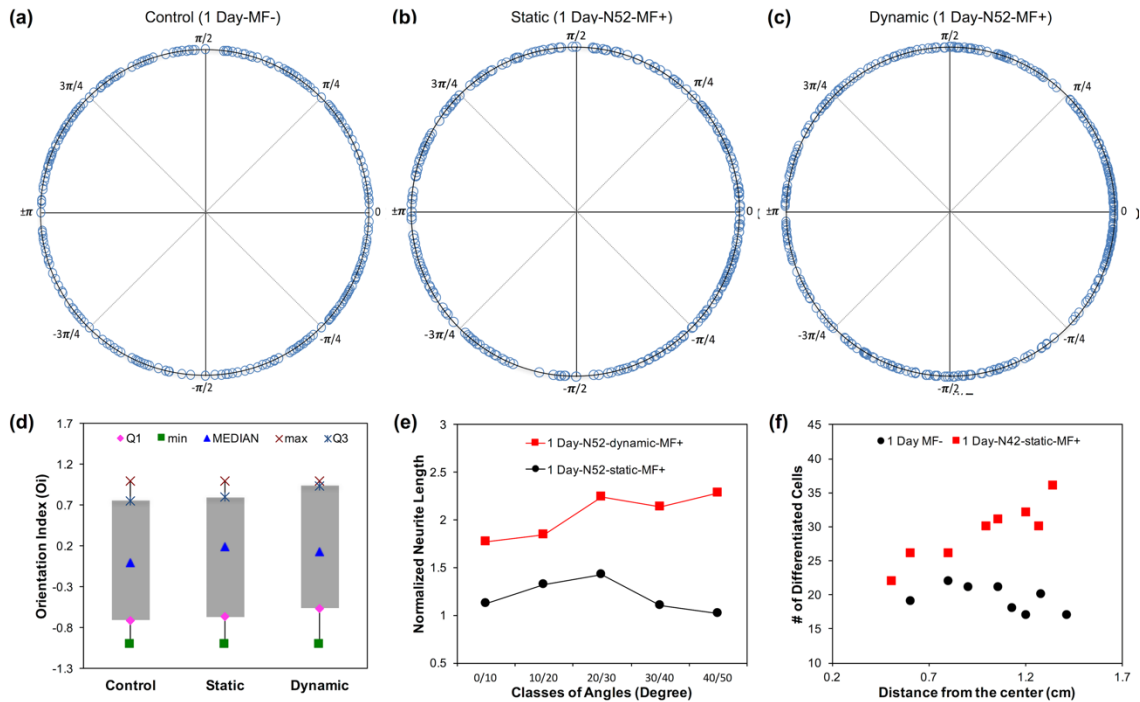
Figure 18. Neurite orientation (θ) distribution. (a) Without MF. (b) With static MFs. (c) With dynamic MFs. (d) Orientation index (cosθ) distribution: The box plot represents the median, the first quartile, the third quartile, the maximum and the minimum value. cosθ~1 for the neurites along the direction of magnetic force. (e) Average length of neurites normalized with the control grouped for different classes of angles of the neurites relative with the direction of the magnetic force (radial direction): The stimulated neurite growth aligned along the direction of the magnetic force with dynamic MFs. (f) The number of differentiated cells distributed throughout the dish (center at 0 cm): The number of differentiated cells increased with the higher magnetic flux. Reprinted with permission from reference 90.

The stimulation effect of the static magnetic force with NPs on the neuronal growth and differentiation was also validated in a Halbach-like magnetic applicator composed by eight of N42 NdFeB magnetic cubes of 0.5 inch (Figure A1, Appendix A, $dT/dr = -23.28$ T/m). It was shown that the ratio of differentiated cells significantly increased by 72%; the number of neurites per differentiated cells increased by 25%; the average neurite length increased by 43% of the control group, as well as the preferential alignment of the neurites

58

along the direction of magnetic force. (Figure A2 and A3, Appendix A) To reveal the relationship between the cell differentiation and the magnetic flux density, the distribution of the differentiated cells along the diameter of the magnetic applicator was plotted in Figure 18(f), which revealed the similar trend with the magnetic flux density. Additionally, the effective induction of neuronal differentiation verified that fluorescent labeling of NGF and the functionalization of Fluor 488 labeled NGF to SPIO-Au NPs did not affect the bioactivity of NGF, and therefore can be used in the future for the fluorescence visualization and identification of NGF-SPIO-Au NPs interacted with cells.

Discussion

Our homemade SPIO-Au NPs were characterized with uniform shape, narrow size distribution, high stability, and facile functionalization with NGF. Although SPIO-Au NPs was proved to have no toxicity in other cell lines, such as mouse leukemic monocyte macrophage cells (36-56 nm, 1-500 μg/mL, > 90% viability, 3 days of incubation)[7] and MC-3T3-E1 cells (17 nm, 10-80 μg/mL, > 93% viability, 7 days of incubation), no viability or proliferation studies were reported on neuron-like cells, which can be essential for the application in neuronal regeneration. Here we confirmed their low cytotoxicity, and high biocompatibility in neuron-like cells, and their potentials in promoting neuron growth and differentiation.

The TEM analysis revealed two different cellular uptake mechanisms. For the cells treated with only SPIO-Au NPs at the concentration of 10 μg/mL, smaller clusters of NPs were found localized in the cytoplasm and no NPs were found at the endocytic pathway, implying that they may directly penetrate into the cells through diffusion. This mechanism

has been proposed by Mustafa et al.[59] for Au NPs at the concentration as low as 10 μg/mL. However, when the SPIO-Au NPs were functionalized with NGF factors, they were more likely to cross the cytoplasmic membrane by endocytosis. To further identify which cellular uptake mechanism was (primarily) utilized, some commonly used inhibitors can be employed to study endocytic pathways, such as Chlorpromazine (to inhibit clathrin-mediated endocytosis), filipin III (to inhibit caveolae) and amiloride (to inhibit micropinocytosis). Detailed discussion will be presented in our future work.[125] By examining the existence of NPs inside the cells, the larger cluster and higher number of NGF functionalized NPs in PC-12 cells indicated that the addition of NGF promoted the cell absorption of NPs.

The morphology analysis in this study confirmed that driven by external magnetic forces, the NGF-SPIO-Au NPs can stimulate the neuronal differentiation, promote the axonal growth, and influence the neurite direction by aligning them toward the direction of the applied magnetic forces. Similar results have been obtained in literature for SPIO NPs driven by static MFs. However, none of the previous works reported the usage of dynamic MFs and examined their effect on neurons treated by NGF-SPIO-Au NPs. Our work innovatively introduced the dynamic MFs to NGF-SPIO-Au NPs for promoting neurite outgrowth. Experimental results proved that the dynamic MFs could remarkably enhance the neurite growth in comparison with the static ones.

To theoretically interpret the above results, it is necessary to establish a mechanical model to analyze NPs under forces. NPs' transport in biological systems is usually governed by several forces: magnetic force F_m, gravity F_g, viscous drag F_v, cytoskeletal

force F_c, buoyancy force F_b and interparticle force F_{in}. For the NPs located inside the neurons, there is another type of force acting on NPs, called cytoskeletal force due to the elongation and the retraction of neurons. For most submicron particles with slow flow rate (<10 mm/s), the magnetic force and the cytoskeletal force dominant as all other forces can be neglected.[126]

For example, the gravity F_g can be expressed as

$$F_g = \rho_{particles} \frac{4}{3} \pi r_{particles}^3 g. \tag{15}$$

As our NPs are composed by SPIO core and Au coating, Eq. (1) can be rewritten as:

$$F_g = \rho_{SPIO} \frac{4}{3} \pi r_{SPIO}^3 g + \rho_{au} \frac{4}{3} \pi \left(r_{partices}^3 - r_{SPIO}^3 \right) g. \tag{16}$$

Here ρ_{SPIO} and ρ_{au} are 5,240 Kg m^{-3} and 19,320 Kg m^{-3} as the density of SPIO and Au, respectively, r_{SPIO} (6.6 nm) is the radius of the SPIO core and $r_{partices}$ (10.4 nm) is the radius of the NPs. g is the gravitational acceleration near Earth's surface (9.81 m s^{-2}).

We can get $F_g = 2.73 * 10^{-19}$ N. With low Reynolds numbers, the viscous force can be expressed as

$$F_\upsilon = -6\pi\eta r_p \left(v_p - v_f \right). \tag{17}$$

Here η is the dynamic velocity of the fluid, v_p is the velocity of the particle, and v_f is the velocity of the fluid. In our experiment, the nanoparticles can be treated to be static, so this force can be neglected. The buoyancy force, F_b is given by:

$$F_b = \rho \frac{4}{3} \pi r_{particles}^3 g \tag{18}$$

Here ρ is the density of the medium (approximated as the density of water 1000 Kg m³). The buoyancy force is calculated to be 2.1 * 10⁻²⁰ N. Under a MF (**B**), the magnetic force F$_m$, on a particle is given by:

$$F_m = (m \cdot \nabla)\mathbf{B}. \tag{19}$$

Here m is the magnetic moment of the particle. Because the MF gradient d**B**/dr in our experiment is the only non-zero component, the Eq. (19) can be simplified to

$$F_m = m\frac{d\mathbf{B}}{dr} = \frac{4}{3}\pi r_{particle}^3 \rho_{SPIO}M\gamma\frac{d\mathbf{B}}{dr} = \frac{4}{3}\pi r_{SPIO}^3 \rho_{SPIO}M\frac{d\mathbf{B}}{dr} \tag{20}$$

Here, γ is the fraction of magnetic volume, which equals to $(\frac{4}{3}\pi r_{SPIO}^3)/$

$(\frac{4}{3}\pi r_{particle}^3)$, M is the magnetization of particles (54.3 Am²Kg⁻¹ from reference),[7] d**B**/dr is the MF gradient (23.28 T/m for N42, 36.19 T/m for N52). We can get F_m = 7.97*10⁻¹⁸ N for N42 magnets and 1.24*10⁻¹⁷ N for N52 magnet exerted on one NP.

To simulate the cytoskeleton force, the neurites can be modeled as Hookian springs with the spring constant k and an elongation of x. If there are n_{cells}^{NPs} NPs in the neuron, the cytoskeleton force per NP is:

$$F_c = \frac{kx}{n_{cells}^{NPs}}. \tag{21}$$

Here n_{cells}^{NPs} is roughly 2.5*10⁵ from literature.[1] From the experimental results the elongation of x for magnetic applicator with N42 magnets is 3.89 μm. When reach equilibrium, the spring constant can be estimated as 5.12 *10⁻¹³ N/μm. Using this simulation, we approximated the average elongation of neurites in the magnetic applicator with N52 magnets as 1.51 μm, which was very close to the experimental value of 1.394

μm. (Note: the cell density of the N52 case was 4 times of the N42 case. So n_{cells}^{NPs} was reduced to $0.625*10^5$ for the N52 case.)

The angle of the neurite can be simulated according to the equation:[1]

$$F_{neur}^{\theta}(\theta, t) = n_{neur}^{NPs} F_m sin\theta = n_{cells}^{NPs} \frac{V_{neur}}{V_{cytop}} F_m sin\theta = \frac{1}{3} k\Delta\theta r \left[\left(\frac{l(t)}{a}\right)^2 - 1\right]. \qquad (22)$$

For $t = 0$, $\theta = \pi/2$ and for magnetic field treating time t_f=24 h, $\theta = \theta_f$. Taking experimental results of using N52 for example, the neurite length $l(t_f)$=1.394*10^{-6} m and k =4.1*10^{-6} N/m, which was calculated before. From the literature,[1] the neurite radius r = 7.5*10^{-7} m, the number of NPs per cell n_{cells}^{NPs} =2.5*10^5 and the parameter a = $\frac{1}{\sqrt{N_b}}$ =0.0045, where N_b=5*10^4 is the number of bridges for cell. Assume a uniform particle distribution in cell cytoplasm, the number of NPs entrapped in neurite n_{neur}^{NPs} can be estimated by knowing the volume of the neurite V_{neur}==π*r^2*L=2.46*10^{-18} m^3 by modeling the neurite as a cylinder with radius r, and length L=1.394*10^{-6} m (experimental value of average neurite length for N52 case) and the volume of the cell cytoplasm V_{cytop}=4.41*10^{-16} m^3 according from reference.[1] By solving the equation (8), we found θ=82.8°, which was very close to the experimental measured value θ=78.5° (Oi=0.2). The modeling results allows the prediction the values of neurite elongation and the angle of the neurite orientation driven by a magnetic applicator formed by eight of N52 magnets, which are in good agreement with the experimental measurement. This model provides a predictive insight of the cellular effect induced by the cytoskeleton force.

This study confirms that applying dynamic MFs on NGF-SPIO-Au NPs are able to accelerate neurite growth by as high as 187% of control within only 24 h. This finding

may be beneficial for the long-term nerve recovery and repair, and thus possesses the clinical importance to treat neurodegenerative diseases. Additionally, the ultra-small size of the SPIO-Au NPs (20.8 nm) are advantageous to transverse the BBB.[127] And the core-shell bimetallic structure makes them promising dual-mode contrast agents for multimode imaging technique, like MRI and computed tomography imaging.[7] It should be acknowledged that only one size of NPs is involved in this work, and future study will focus on the size dependence analysis. And we should also explore more variables like the strength of the MFs as well as the rotating speed and the angle of the dynamic MF, which may positively affect the development of neurites.

Conclusions

In this work, the SPIO-Au NPs (D: 20.8 ± 2.7 nm) were synthesized by combining co-precipitation and iterative hydroxylamine seeding method, and then functionalized with NGF. The light absorbance and zeta potential measurement confirmed the successful functionalization of NGF with NPs. The viability results (> 96%) indicated the excellent biocompatibility of SPIO-Au NPs. The TEM images of PC-12 cells treated with NGF-SPIO-Au NPs showed that the cellular uptake can be enhanced by the functionalization of NGF. Then a noninvasive magnetic stimulation technique was developed by applying dynamic MFs on cells treated with NGF-SPIO-Au NPs. Our results showed that this multifunctional nanomedicine was able to effectively stimulate and promote the neuronal growth. And the dynamic MF was favored, as it drove the neurite stretching more efficiently than that of the static MF. Also, a cytoskeleton force model was created, which agrees well with our experimental data of neurite elongation and orientation. This study

confirmed the potential of non-invasive magnetic neuron stimulation technique synergistically combining the biocompatible magnetic NGF-SPIO-Au NPs with dynamic MFs for promoting neuronal growth.

CHAPTER V

ELECTROMAGNETIC STIMULATION USING LIGHT EMITTING DIODES:

TOWARDS NEUROREGENERATION (PC-12 CELLS)

This chapter reports the use of low-intensity light-emitting diode (LED) (525 nm, 1.09, 1.44, and 1.90 mW/cm^2) to stimulate the NGF-SPIO-Au NPs of 20 µg/ml on PC-12 neuron-like cells. A remarkable Ca^{2+} influx was detected in differentiated PC-12 cells treated with NPs, irradiated by LED of 1.90 and 1.44 mW/cm^2 with great cell viability (>84%) and proliferations. The strong heat generated through their plasmonic surface upon LED irradiation on NGF-SPIO-Au NPs was observed. For cells treated with LED (1.90 mW/cm^2) and NGF-SPIO-Au NPs, a dramatic enhancement of neuronal differentiation (83%) and neurite outgrowth (51%) was found, and the upregulation of both the neural differentiation specific marker (β3-tubulin) and the cell adhesive molecule (integrin β1) was observed by the reverse transcription-polymerase chain reaction and western blot analysis.

Methods

Preparation of NGF-SPIO-Au NPs

SPIO-Au NPs were first synthesized using the seed growth method and then functionalized with NGF at the mass ratio of 14:1 (NPs:NGF). Detailed procedures about the synthesis of SPIO-Au NPs and the functionalization of NGF are available in Chapter II and our previous publication.[90] The as-synthesized NGF-SPIO-Au NPs in the diameter of 20.8 nm were directly used in the following experiments without any further purification.

66

Cell culture

PC-12 cells (from rat pheochromocytoma) obtained from American Type Culture Collection (ATCC) were cultured in growth medium composed of ATCC modified RPMI-1640 medium supplemented with 10% heat-inactivated horse serum (HS), 5% fetal bovine serum (FBS) and 1% penicillin-streptomycin (medium and supplements were purchased from Gibco). Cells were seeded and cultured in poly-L-lysine (PLL, P4707, Sigma-Aldrich) pre-coated Petri dishes in a humidified incubator under a 5% CO_2 atmosphere at 37°C. To induce cell differentiation, PC-12 cells were cultured in serum-reduced medium (1% heat-inactivated HS and 0.5% FBS).

Cytotoxicity evaluation

To evaluate the cell viability of LED irradiation, the cell counting kit-8 (CCK-8, Sigma-Aldrich) was used at first. PC-12 cells were seeded into PLL-coated 96-well tissue culture plates at a density of $2*10^3$ cells/well with growth medium. After 24 hours of incubation, the medium was replaced by fresh medium containing NGF-SPIO-Au NPs at the concentrations of 0, 1, 5, 10 and 20 μg/ml. On each day, cells were exposed to LED irradiation (wavelength: 525 nm, maximum intensity: 1.90 mW/cm^2 (LIU525B, Thorlabs Inc. Newton, New Jersey)) at different time periods (1 min, 10 min, 30 min and 1 h). Cells without treating with LED irradiation or NPs were cultured as control groups. After 1, 3 and 5 days of incubation, the media were replaced by fresh media and 10 μl of CCK-8 solution was added to each well and followed by the incubation of the plates for 2 hours at 37 °C. The absorbance was measured using a microplate reader (SpectraMax i3x, Molecular Devices, LLC. San Jose, CA) at a wavelength of 450 nm.

To further evaluate the cytotoxicity of LED irradiation at different intensities, PC-12 cells were seeded into 24-well plates coated with PLL and incubated for 1 day. Then the cells were washed with Dulbecco's phosphate-buffered saline (DPBS) and incubated with NGF-SPIO-Au NPs at the concentrations of 5, 10 and 20 µg/ml. On each day, cells were exposed to LED irradiation for 30 minutes at 3 different light intensities (1.90, 1.44 and 1.09 mW/cm^2), which were regulated by using multilayers of the light diffuser films (Matte 1 sided, Inventables Inc. Chicago, IL). Cells without NPs were cultured as control group. After 1, 3 and 5 days, cells were dislodged from the dish, centrifuged and dispersed in the growth medium. Cells were then stained with 0.4% Trypan blue solution (Gibco, Grand Island, NY) and examined through a hemocytometer (Bright-Line™ and Hy-Lite™ Counting Chambers, Hausser Scientific Inc. Horsham, PA).

Regulation of neurite growth by LED irradiation

PC-12 cells were seeded in PLL pre-coated Ibidi Petri dishes (D: 35 mm). After 24-hour incubation in the serum-reduced medium, cells were treated with NGF-SPIO-Au NPs at the concentration of 20 µg/ml in the serum reduced medium. Cells were incubated for another 24 hours to allow the NPs to interact with cells and to induce differentiation mediated by NGF. Then the cells were cultured for 1 day with 30 minutes of LED irradiation at the intensity of 1.90, 1.44 and 1.09 mW/cm^2 daily, respectively. Cells cultured without being treated by LED irradiation or NPs were considered as controls. During the LED irradiation, the temperature of the medium was recorded using the HH374 4-Channel Type K Data Logger Thermometer (OMEGA Engineering, Inc. Norwalk, CT). Finally, the neuronal differentiation of cells (cells with at least one neurite) was observed

and recorded using a light microscope (Axiovert 200M Inverted Fluorescence/phase Contrast Microscope (Carl Zeiss, Inc. Jena, Germany) equipped with an AxioCam CCD camera). For each group, at least 40 pictures were acquired, and more than 4000 cells were quantified. The number of differentiated cells, the length and number of neurites in each image were counted and measured using the Simple Neurite Tracer as a plugin of Fiji.

Calcium imaging

PC-12 cells treated with NGF-SPIO-Au NPs of 20 µg/ml were incubated with the Fluo-4 direct calcium assay (Life Technologies) according to the manufacturer's protocol and with 5 mM probenecid as a stock solution. Briefly, 10 ml of calcium assay buffer and 200 µL of the 250 mM probenecid stock solution were mixed with the calcium reagent. The calcium reagent solution was then directly added to dishes containing cells in the growth medium in a 1:1 ratio. The dishes were then incubated for 60 minutes before fluorescence imaging. For the LED light stimulation, the calcium level was monitored immediately with the treatment of LED irradiation at the intensity of 1.90, 1.44 and 1.09 mW/cm^2. The group without LED irradiation was considered as a control. The Ca^{2+} signals of the PC-12 cells were captured by performing the real-time confocal imaging on Zeiss LSM 510 META NLO Two-Photon Laser Scanning Confocal Microscope System (Carl Zeiss, Inc. Jena, Germany) with 40 objectives under 488-nm laser excitation at the speed of 2 frames/second (512x512 pixel images). The measured fluorescence signals F were normalized to the baseline fluorescence intensity F$_0$ (10 s).

RNA extraction and reverse transcription-polymerase chain reaction (RT-PCR)

PC-12 cells were seeded in PLL pre-coated 6-well plates. After reaching

confluency, cells were incubated with fresh serum-reduced medium with and without treatment with NGF-SPIO-Au NPs at the concentration of 20 μg/ml, respectively. Cells were then incubated for another 24 hours to allow the NPs to sufficiently interact with cells and to induce differentiation. Then the cells were cultured for 1 day with LED irradiation for 30 minutes at the intensities of 1.90, 1.44, and 1.09 mW/cm^2, respectively. Then, the total mRNA was extracted from PC-12 cells using the RNeasy$^@$ mini kit (Qiagen Sciences), according to the manufacturer's protocol. mRNA concentration of each sample was measured using a NanoDrop 2000c Spectrophotometer (NanoDrop Technologies, LLC, Wilimington, Delaware). All the mRNA samples were diluted to 10 ng/μl. Then the diluted mRNA samples were reverse-transcribed to complementary DNA by using a high capacity cDNA reverse transcription kit (Applied Biosystems) and followed by polymerase chain reaction (PCR) amplification using TaqMan$^@$ gene expression assays (Applied Biosystems) for integrin beta 1 (Rn00566727_m1) and tubulin beta 3 (Rn00594933_m1). The expression levels were recorded with respect to the control group (without LEDs) and were normalized to GAPDH (Rn01775763_g1).

Western blot analysis

Cells were treated according to the previous RT-PCR process. The total cell lysate was collected and prepared using Pierce$^@$ RIPA lysis and extraction buffer (Thermo Scientific) containing the cOmplete EDTA-free protease inhibitor (Millipore Sigma) (1 tablet for 10 ml lysis buffer). After lysing for 30 minutes on ice and then centrifuging at 14000 g for 15 minutes at 4 °C, the supernatant was collected. 2x Laemmli sample buffer (Bio-Rad) was added to the protein solution in a 1: 1 ratio and the protein solution was

then heated to 95 °C for 5 min in order to denature the protein, and centrifuged at 16000

g (g is the unit of the relative centrifugal force, g=1.118*10^{-5} (radius of the rotor) * (RPM)^2

) for 1 minute at 4 °C. Then the samples were loaded onto Mini-PROTEAN® TGX™

Precast Protein Gels (Bio-Rad). After running the gel at 80 V for 5 minutes and 150 V for

1 hour, the proteins were transferred (90 V, 70 min) onto an Immun-Blot® PVDF

Membrane (Bio-Rad). The membrane was then blocked for 60 minutes with the blocking

buffer (1:1 Odyssey$^@$ blocking buffer in Tris-buffered saline (TBS) (LI-COR): 1x TBS).

After blocking, the membrane was incubated overnight at 4 °C with β3-tubulin (Cell

Signaling, 5666) and GAPDH (Invitrogen, PA1988) primary antibodies (at 1:1000),

respectively. After washing 5 times with 0.05% Tween-20 in TBS for 5 minutes, the

membranes were incubated for 1 hour at room temperature with StarBright™ Blue 700

Goat Anti-Rabbit IgG (12004158, Bio-Rad) diluted to 1:2500 (v/v). The membranes were

washed 5 times again with 0.05% Tween-20 in TBS and 2 times with TBS. Finally, the

labeled proteins were visualized by using the LI-COR Odyssey CLx Infrared Scanner (LI-

COR Biosciences) and analyzed by using the ImageJ software.

Statistical analysis

All results were analyzed based on at least three independent experiments and

presented as mean ± standard deviation. Statistical analysis was performed by using the

analysis of variance (ANOVA) with Tukey post-hoc test to assess NGF-SPIO-Au treated

and untreated cells with and without LED irradiation. A p-value less than 0.05 was

considered as a significant difference.

Results

Our previous study has shown that our lab-synthesized SPIO-Au NPs with the diameter of 20.8 nm had quasi-spherical shape with narrow size distribution and excellent optical property. The successful functionalization of NGF to SPIO-Au NPs was confirmed through zeta potential measurements.[90] In the following experiments, we focused on exploring the synergistic effect of LED light and NGF-SPIO-Au NPs for promoted neuronal differentiation and neurite growth.

Cytotoxicity evaluation

The viability and proliferation evaluation of NGF-SPIO-Au NP-treated PC-12 cells irradiated by LED light was examined by measuring the absorbance of the formazan dye generated by the reduction of water-soluble tetrazolium salt (WST-8) through dehydrogenases activities in cells, which was proportional to the number of living cells.[109] Our results show that without NGF-SPIO-Au NPs, the stand-alone LED exposure did not induce significant loss of the WST-8 reduction for up to 5 days of incubation, revealing the unaffected cellular proliferation by LED illumination alone (Figure 19). After 1 day of incubation with 20 μg/ml of NGF-SPIO-Au NPs, the LED exposure of 1 minute, 10 minutes, and 1 hour resulted in a slight decrease of WST-8 reduction (Figure 19(a)). After 3 days of incubation, this decrease by LED effect was noticed at the NP concentration of 1, 5, 10, and 20 μg/ml (Figure 19(b)). After 5 days of incubation, the decrease of WST-8 reduction was noticed at the concentrations of 5 and 10 μg/ml (Figure 19(c)), indicating that the LED irradiation suppressed the promotional effect of NPs on cell proliferation. However, the synergistic effect of LEDs and NPs still resulted in a higher proliferation

rate compared with the control groups without LEDs and NPs. Figure 19(d) showed the time and concentration dependence of the WST-8 reduction with 30 minutes of LED exposure each day. Without NP-treatment, the PC-12 cells gained the highest MST-8 reduction rate after 5 days. However, the highest WST-8 reduction rate with NP-treatment was observed after 3 days, which might be explained by the fact that the existence of NPs largely promoted the WST-8 reduction and therefore cells reached confluency after 3 days of incubation.
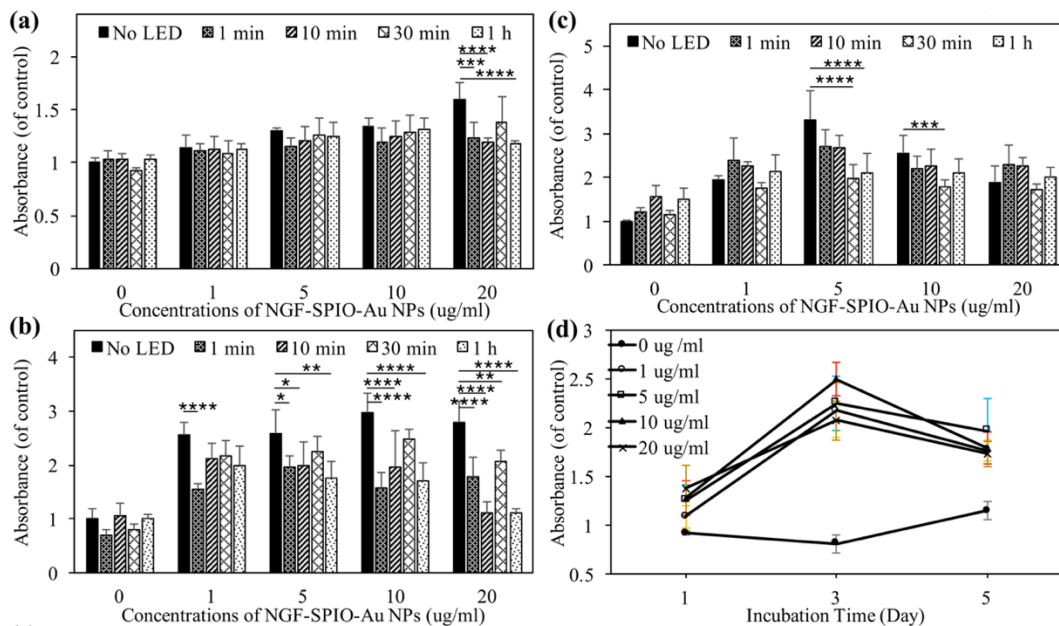
Figure 19. Cell viability evaluation by using a CCK-8 kit. PC-12 cells treated and untreated by NGF-SPIO-Au NPs for (a): 1 day, (b): 3 days and (c): 5 days of incubation with 0 minutes, 1 minute, 10 minutes, 30 minutes and 1 hour of LED exposure (1.90 mW/cm^2) daily; (d) the time and concentration dependency of absorbance value for cells exposed to 30 minutes of LED light (1.90 mW/cm^2) daily. *p < 0.05; **p < 0.01; ***p < 0.001, ****p < 0.0001.
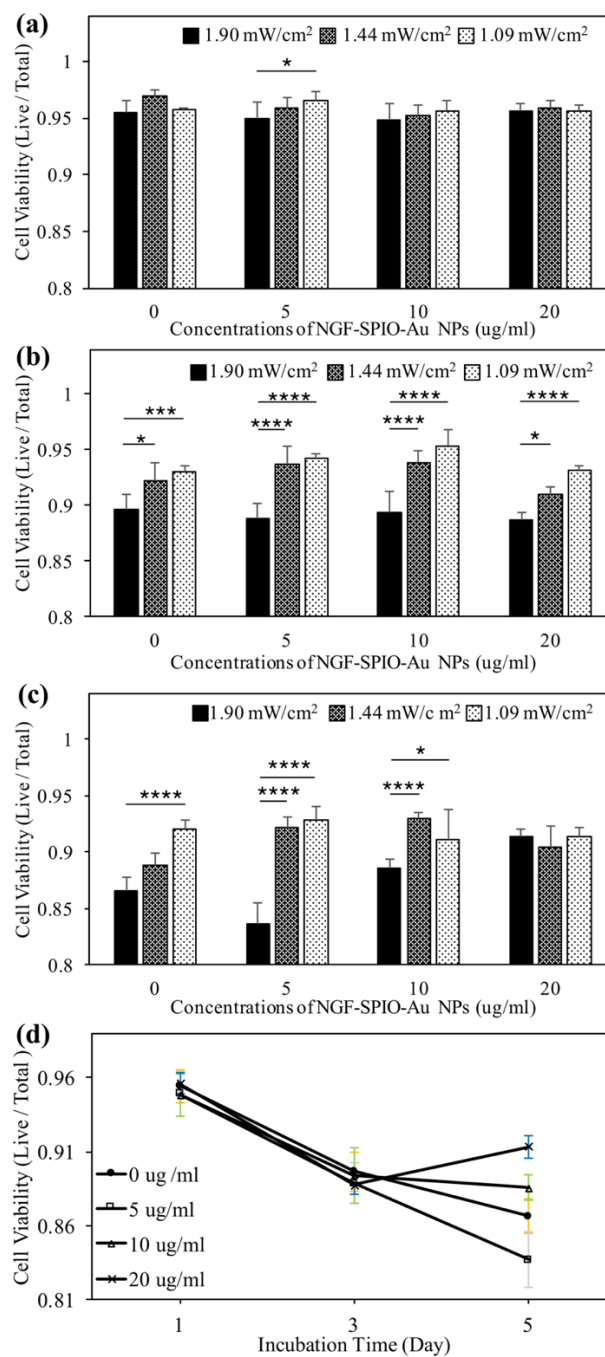
Figure 20. Cell viability evaluation by Trypan Blue staining. PC-12 cells treated and untreated by NGF-SPIO-Au NPs were irradiated with 30-minutes of LED light at 3 different intensities: 1.90, 1.44 and 1.09 mW/cm² daily for the (a): 1 day, (b): 3 days and (c): 5 days of incubation, (d) the time and concentration dependency of cell viability for cells exposed to 30 minutes of LED light (1.90 mW/cm²) each day. *p < 0.05; **p < 0.01; ***p < 0.001, ****p < 0.0001.

74

To further explore the cytotoxic effect of LEDs at different light intensities with NGF-SPIO-Au NPs, the Trypan blue exclusion assay was performed. The results of the living cells to total cells ratio showed that after 1 day of incubation, the LED intensity increased from 1.09 to 1.90 mW/cm^2 induced a slight reduction of cell viability from 0.97 to 0.95 at the NP concentration of 5 μg/ml, while the cell viability of all LED intensities at NP concentrations from 0-20 μg/ml was still above 0.95, indicating no obvious cytotoxic effect of LEDs on PC-12 cells at this time point (Figure 20(a)). After 3 days of incubation, only a slight reduction of cell viability was observed for the LED illumination of 1.90 mW/cm^2 at all NP concentrations (0-20 μg/ml, viablity >89%) (Figure 20(b)). After 5 days of incubation, the slight reduction of cell viability by using LED with stronger intensities was only observed at NP concentrations ≤10 μg/ml (Figure 20(c)). At this point, the viability is recovered at NP concentrations of 20 μg/ml, confirming that LEDs had little long-term effect on viability at this concentration of NPs (Figure 20(d)). To minimize the viability effect and maximize the stimulation effect of the LED light, it is recommended to use LEDs at a higher intensity (i.e., 1.90 mW/cm^2) for a shorter time of incubation (i.e., 1 day) with higher concentrations of NPs (i.e., 20 μg/ml).

Thermal effect of LED light

The temperature measurements in the cell culture medium under the LED light exposure from 0 to 1800 seconds showed that the LED irradiation elevated the local medium temperature after 30 minutes of LED exposure (Figure 21), while without LED light, this temperature elevation was not observed for both cases with and without NP treatment. The NPs treated medium temperature under the LED irradiation of 1.90

mW/cm^2 increased by 4.6 °C, while this value was 3.3 °C and 2.4 °C under the LED

irradiation of 1.44 and 1.09 mW/cm^2, respectively. It is noticed that the temperature of the

medium reached equilibrium after the LED irradiation of 1100 seconds. By comparing the

temperature rise of LED irradiation at 1.90 mW/cm^2, it is found that the temperature rise

of the NPs treated group (marked as " " in Figure 21, total temperature increase is 4.6 °C)

is higher than that of the group without NPs (marked as"×" in Figure 21, temperature

increase is 3.5 °C), at the same LED irradiation intensity. This higher temperature increase

is mainly due to the enhanced localized surface plasmon resonance (LSPR) effect of NGF-

SPIO-Au NPs, as reported from our previous work[128]: a strong light absorbance peak was

observed at the wavelength of 525 nm, leading to the conversion of the photon energy to

heat.
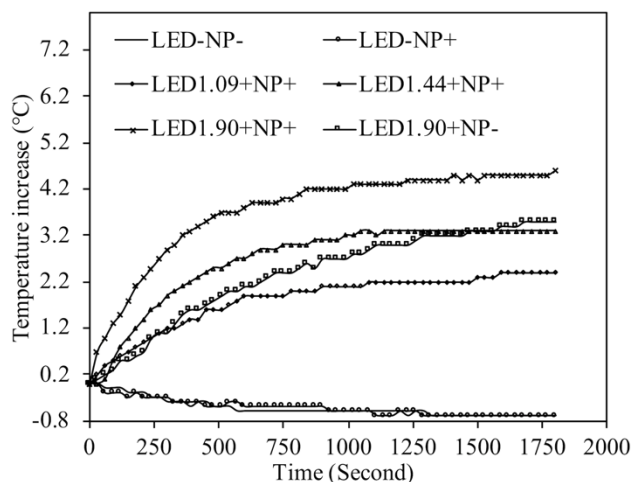
Figure 21. Temperature increase of cell culture media with and without plasmonic NGF-SPIO-Au NPs under the irradiation of LEDs or not. The temperature increase is higher at stronger LED intensity. The temperature rise of the NP-treated group is higher than that of the group without NPs at the LED irradiation of 1.90 mW/cm^2, confirming the photothermal effect of NGF-SPIO-Au NPs.

To examine the synergistic effect of LED light and NGF-SPIO-Au NPs on neuronal differentiation, PC-12 cells treated with NPs were exposed to LED light of different intensities for 30 minutes. PC-12 cells derived from rat pheochromocytoma respond to NGF by induction of the neuronal phenotype. Thus they have been widely used as a useful model to examine the neuronal differentiation.[129] The morphological differentiation of PC-12 cells in 5 different groups were recorded: LED-NP- (control group: no LED exposure, no NP treatment), LED-NP+ (no LED exposure, with NP treatment), LED1.90 (LED: 1.90 mW/cm^2, with NP treatment), LED1.44 (LED:1.44 mW/cm^2, with NP treatment) and LED1.09 (LED:1.09 mW/cm^2 LED exposure, with NP treatment).

To quantitatively investigate the level of neuronal differentiation, the number of differentiated cells and total cells were counted for each group. After 1 day of incubation, cells treated with NGF-SPIO-Au NPs and exposed to LED light showed a significant increase of the ratio of differentiated cells: for LED intensity at 1.90 mW/cm^2, this value reached 0.13, whereas for the control groups without LEDs or NP treatment, this value was only 0.07 . LED light at lower intensities also led to an increase in differentiated cells (0.11 for LED at 1.44 and 1.09 mW/cm^2) in comparison with the control groups (Figure 22(a)).
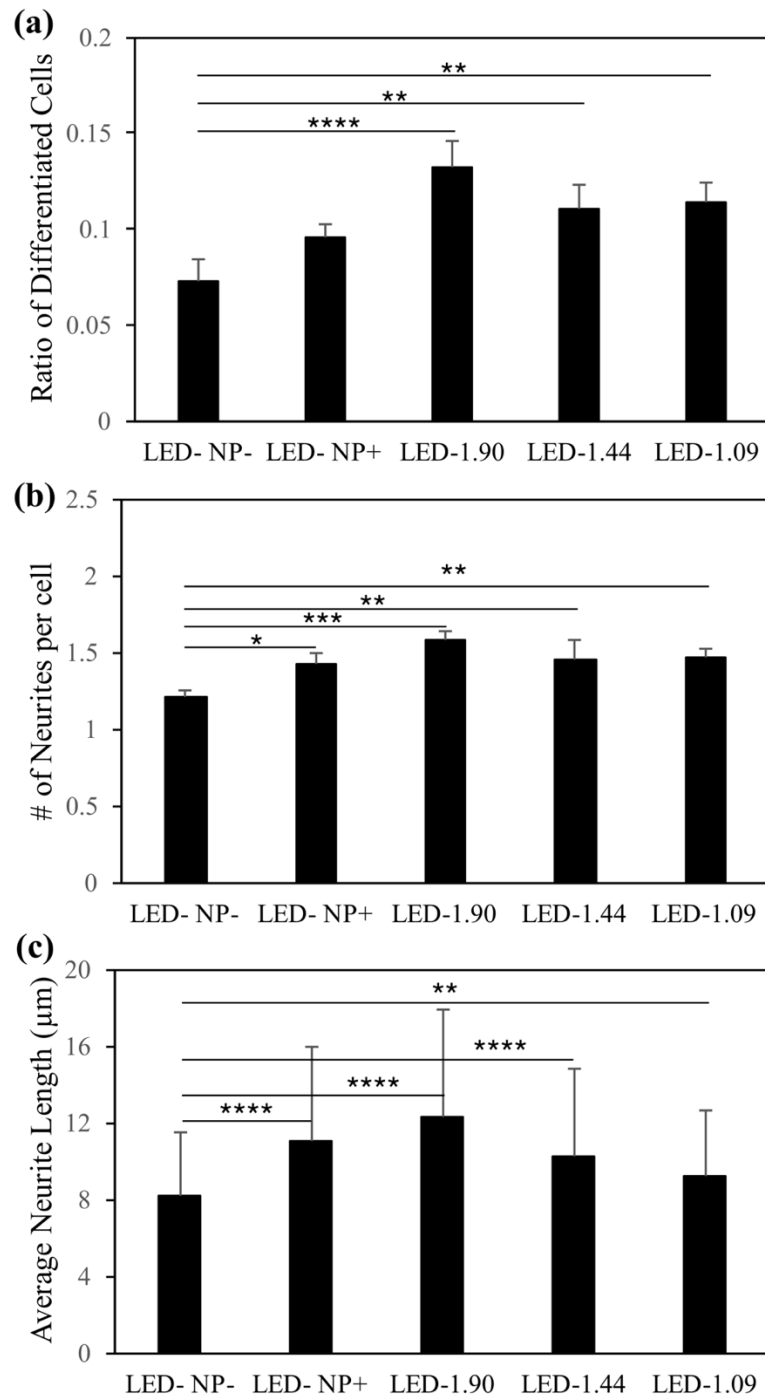
Figure 22. Morphology analysis for NGF-SPIO-Au NPs treated and untreated PC-12 cells exposed with and without LEDs. (a) Percentage of differentiated neuronal phenotype cells (b) Number of neurites per cell (c) Average neurite length. Group without LED or NPs were treated as control group. *p < 0.05; **p < 0.01; ***p < 0.001, ****p < 0.0001.

78

A similar trend was observed in examining the number of neurites per cells, as another parameter characterizing the level of neuronal differentiation: cells treated with NGF-SPIO-Au NPs and LED light developed more neurites per cell compared with the control groups without NPs or LED light. For the LED light intensities at 1.90, 1.44 and 1.09 mW/cm^2, the average number of neurites per cell is 1.58, 1.45 and 1.47, respectively, while it is 1.43 for the groups with only NPs and 1.21 for the control groups (Figure 22(b)).

The neurites' length was also measured and quantified for examining the morphological changes of PC-12 cells. The groups treated with NPs and LED of 1.90 mW/cm^2 had the longest average neurite length of 12.24 μm, with an increase of about 51% (of control group). However, the groups with only NPs had an average neurite length of 11 μm (an increase of 35% of control group), indicating the synergistic effect of LED of 1.90 mW/cm^2 and NPs on promoting neurite growth, which was not observed at lower LED intensities (1.44 and 1.09 mW/cm^2) (Figure 22(c)).

Localized Ca^{2+} signaling

To demonstrate whether the LED light could induce Ca^{2+} influx in differentiated PC-12 cells treated with NGF-SPIO-Au NPs, the localized Ca^{2+} signal was visualized using confocal fluorescence microscopy. Results showed no fluorescence intensity change for PC-12 cells without LED irradiation for both NPs treated and untreated cases, indicating no change of intracellular Ca^{2+} level (1st, 2nd, and 4th row) without the LED treatment, while an enhancement of the fluorescence intensities (red circle area) was observed for LED intensities at 1.90 and 1.44 mW/cm^2, indicating an increase of Ca^{2+} level stimulated by LED light (3rd and 5th row) (Figure 23(a)). The F/F0 (normalized

fluorescence by background fluorescence) in the red circle area was plotted in Figure 23(b) (1st row), (c) (2rd and 3th row), (d) (4th and 5th row), and (e) (6th row). During the exposure of LED light at the intensities of 1.90 and 1.44 mW/cm^2, the fluorescence intensity was elevated from the baseline, indicating the localized Ca^{2+} influx stimulated by LED light. On the other hand, neurons without LEDs exposure did not exhibit any elevation of the Ca^{2+} level from the baseline for both the NP-treated and untreated cases.
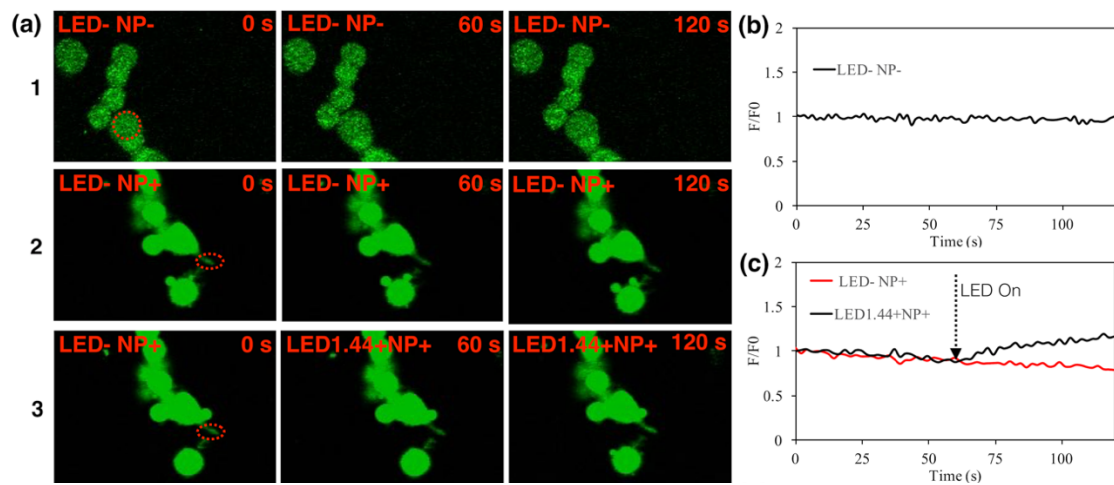
Figure 23. Calcium influx induced by LEDs at the neurites. (a). The 1st row shows control group of cells without LEDs and NPs; the 2nd and 4th row shows groups of cells with NPs and without LED treatment. For the 3rd, 5th and 6th row, cells with NPs were irradiated by LED light at the intensity of 1.44, 1.09 and 1.90 mW/cm^2 starting from t=60s to t=120s. (b). The normalized fluorescence intensity of circled area in the 1st row of (a) for the control group. (c) The normalized fluorescence intensity of circled area in the 2nd and 3rd row of (a) for the NP treated group without LED and LED intensity=1.44 mW/cm^2, respectively. (d). The normalized fluorescence intensity of circled area in the 4th and 5th row of (a) for the NP treated group without LED and LED intensity=1.90 mW/cm^2, respectively. (e). The normalized fluorescence intensity of circled area i and ii in the 6th row of (a) for LED intensity=1.90 mW/cm^2.

Figure 23 Continued
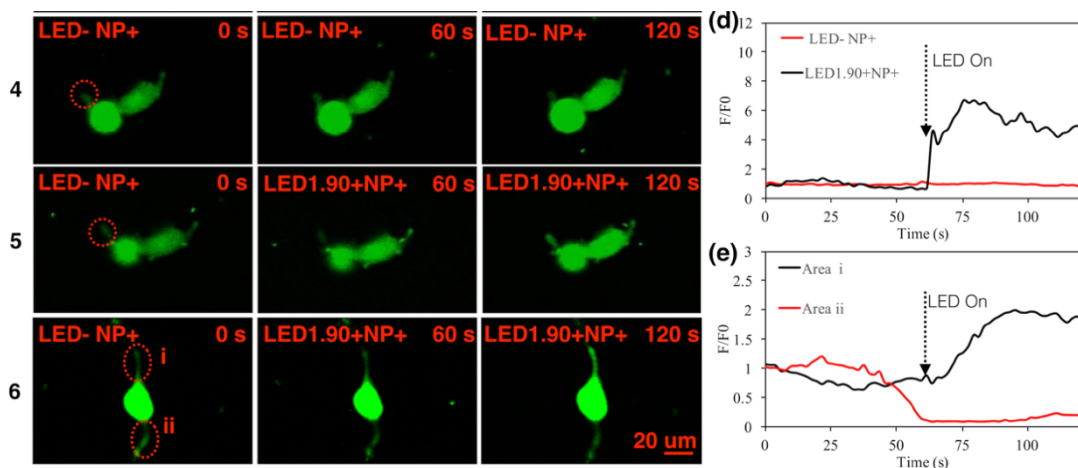
Molecular effects

The RT-PCR and western blot assay were used to quantify the effect of LED light and NGF-SPIO-Au NPs on the expression level of the adhesive molecule, integrin β1, and the neural specific marker, β3-tubulin in PC-12 cells. The upregulation of the mRNA level of integrin β1 in PC-12 cells was observed in groups treated with LED light and NGF-SPIO-Au NPs as compared with the control groups (with NPs only). While without NPs, there was no significant change of mRNA level of integrin β1 in LED light irradiated PC-12 cells as compared with the control groups (no NPs and no LED irradiation) (Figure 24(a)). These findings revealed that the synergistic effect of LED and NGF-SPIO-Au NPs enhanced the expression of integrin β1, which may be beneficial to the cell attachment and thus the induction of neurite growth.[87]

To account for the stimulation effect of LED and NGF-SPIO-Au NPs on neural differentiation, the mRNA levels of neural-specific marker, β3-tubulin were assayed. The results showed the upregulated expression of β3-tubulin in groups treated with LED and

NPs at the intensities of 1.90 and 1.44 mW/cm^2 as compared with the control groups (with NPs only). However, without NPs, the groups exposed to LED light exhibited a slightly reduced expression level of β3-tubulin as compared with the control groups (no LED irradiation) (Figure 24(b)).
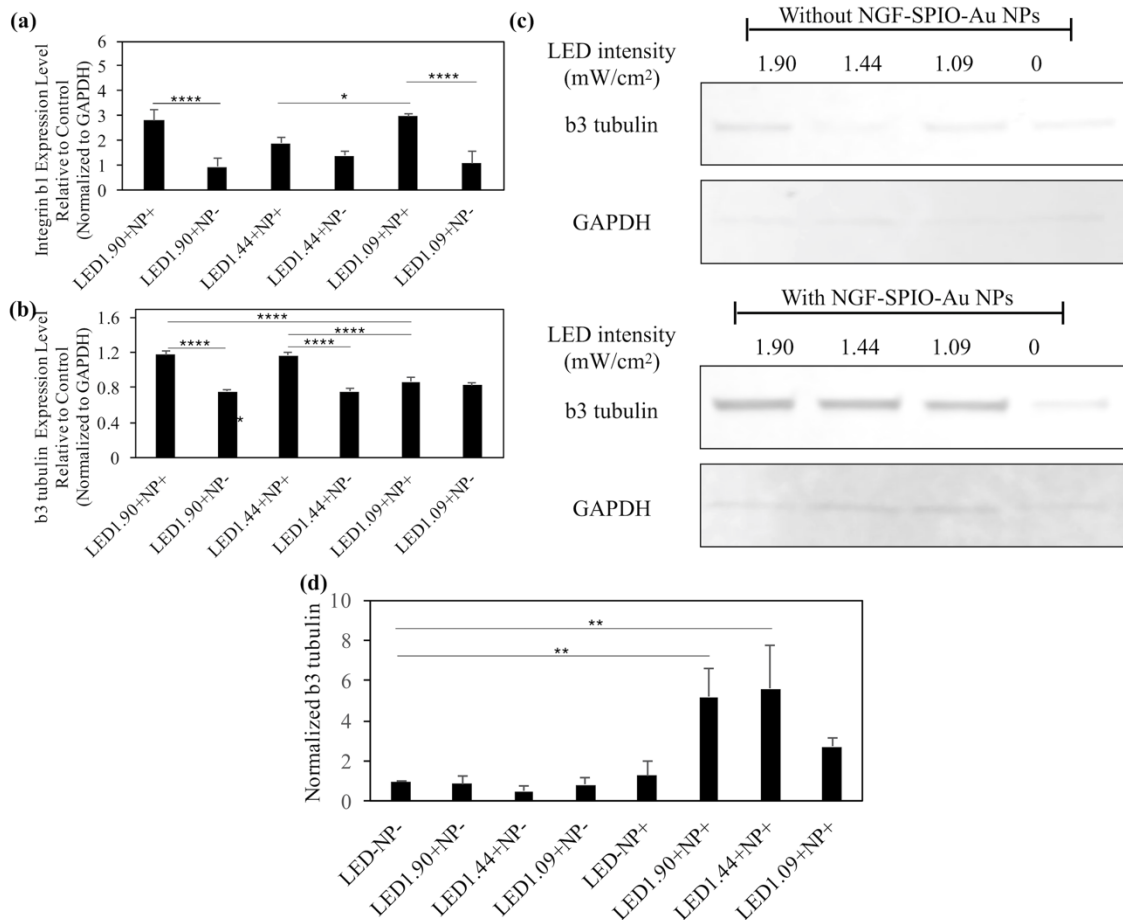
Figure 24. Results of RT-PCR and western blots for PC-12 cells treated with/without NGF-SPIO-Au NPs (20 μg/ml) and exposed to different intensity of LED light. (a) RT-PCR results for the mRNA level of integrin β1 of differentiated PC-12 cells. (b) RT-PCR for the mRNA level of β3-tubulin of differentiated PC-12 cells. The gene expression level was normalized to GAPDH as housekeeping gene. (c) Western blot analysis of β3-tubulin of differentiated PC-12 cells. (d) The average level of β3-tubulin protein normalized by GAPDH from triplicated experiments. *p < 0.05; **p < 0.01; ***p < 0.001, ****p < 0.0001.

82

This synergistic effect was also confirmed by the western blot analysis. The expression level of β3-tubulin protein was significantly upregulated by the LED (1.90 and 1.44 mW/cm^2) and NPs in comparison with the groups without LED and NPs, while the treatment of NPs alone or LED alone did not affect the expression level of β3-tubulin (Figure 24(c) and (d)).

Discussion

There are plenty of previous works focused on using iron oxide NPs as the nano carrier of NGF to stimulate neurite outgrowth under the direction of external magnetic fields.[1,3,86,87] However, the high dose of iron oxide NPs was reported to cause cell dysfunction.[21,22,130] Too strong magnetic fields with long-time exposure have also been proven to be toxic to cells[131-133] and may suppress the reproductive process,[134,135] not to mention the other challenges of using bare iron oxide NPs like the aggregations.[12] In this work, we presented the exploration of using our lab-synthesized NGF-SPIO-Au NPs as a nanomedicine to regenerate neurons non-invasively through low-intensity LED illumination. We demonstrated that low-intensity LEDs (up to 1.90 mW/cm^2) can trigger the neurite growth and neuronal differentiation remarkably with a stimulation time up to 30 minutes for 1 day of incubation. Within this time period, LED light did not induce severe toxicity on PC-12 cells at the measured intensities (up to 1.90 mW/cm^2) and exposure time (up to 1 hour).

From the morphology evaluation, we demonstrated the intensity-dependence of neurite growth and neuronal differentiation of PC-12 cells treated by LED irradiated NPs. And the comparison between the group treated by NPs alone, and by LED-illuminated

NPs showed that the synergistic effect of LED irradiation and NGF-SPIO-Au NPs is more effective than using NPs alone, which could be due to the remarkable photothermal effect of NPs from LED irradiation.

It is known that microtubules are essential cytoskeletal elements within the growth cones that affect the axon regeneration and outgrowth under the stimulation.[136] The associated microtubule proteins can be regulated by Ca^{2+} and/or Ca^{2+} sensitive kinases.[137] Filamentous actin (F-actin), as the other major cytoskeletal element within the growth cones, is also regulated by Ca^{2+} through affecting the binding affinity of various actin-binding proteins (ABP) to F-actin.[138] Therefore the concentration of cytoplasmic and intracellular Ca^{2+} has been treated as an essential regulator of neurite outgrowth, and the optimal range of Ca^{2+} can promote the neurite steering and extension.[139] Our results showed that the LED light-irradiated NPs induced a local Ca^{2+} influx in neurites, which implied the formation of the local calcium gradients that could interact with the growth cone cytoskeleton.[108]

In addition, we found from the molecular analysis that the stimulation by LED and NPs upregulated the neuronal specific marker as well as the cell adhesive molecules, which were associated with the cell attachment and neurite growth. And this stimulation effect was not found by LED or NPs alone. Additionally, the heat generation was observed during the LED irradiation of the NPs-treated medium which was the result of the LSPR effect of NGF-SPIO-Au NPs. These results suggest that the photostimulation of LED light might promote the neuronal differentiation and the neurite outgrowth via the photothermal effect of LED irradiated NGF-SPIO-Au NPs by modulating the local Ca^{2+} level and

enhancing the cell attachment. However, it is still unclear that whether any other factors triggered by LED illumination on NGF-SPIO-Au NPs could affect the neuronal differentiation pathway. Therefore a more detailed investigation on exploring other neural-related factors is needed to further explore the mechanism of nerve regeneration, which will be the focus of our future study.

Conclusions

In summary, this study reported a novel non-invasive neuroregeneration approach of using low-intensity LED light to irradiate NGF-SPIO-Au NPs, a promising nanomedicine, for promoting remarkable neuronal differentiation and neurite outgrowth in an intensity-dependent manner. And LEDs of higher intensities were favored to produce more differentiated cells, more branching points and longer neurite length. No severe toxicity was observed upon LED light irradiation at our measured intensities. In particular, NGF-SPIO-Au NPs irradiated by LED light of 1.90 mW/cm^2 were found to induce the calcium influx in the neurites, and upregulate a neural differentiation specific marker, β3-tubulin, and an adhesive molecule integrin β1. The results demonstrated a promising non-invasive nanomedicine-based neurogenesis induction scheme using low-intensity LED irradiated NGF-SPIO-Au NPs for nerve regeneration.

CHAPTER VI

CONCLUSIONS

In this thesis, we developed the multifunctional SPIO-Au core-shell NPs for promoting neuronal differentiation and neurite growth with the stimulation of MF and LEDs for nerve regeneration. In chapter 2, we first introduced a synergistic approach combing the seed growth and the citrate reducing method to prepare SPIO-Au NPs in DI water with well-controlled coating thickness (1.5 nm to 8.8 nm). NPs were proved to possess uniform quasi-spherical shape and narrow size distribution by TEM images. The successful formation of SPIO-Au NPs at predicted sizes and concentrations was further supported by ICP-MS analysis. The slightly red shift of the surface plasmon resonance band with the increasing Au shell thickness was verified by UV-Vis spectra. Lab synthesized SPIO-Au NPs also exhibited excellent stability in DI water and the cell growth medium for up to 21 days.

Then in chapter 3 we evaluated the unique plasmonic behavior of SPIO-Au NPs by measuring the photothermal efficiency of SPIO-Au NPs. A novel TC-tip-exposing temperature assessment technique was developed for the accurate measurement of the temperature profile of the lab-synthesized SPIO-Au NPs described in chapter 1. A FEM model using COMSOL Multiphysics $^®$ was designed to simulate the temperature profile within the first 30 seconds. By combining the experimental measurement and the simulation, the photothermal conversion efficiency was found to be close to 1 for all the concentrations, which was further confirmed by the Mie theory by calculating the absorption/extinction ratio.

The work on exploring the effect of SPIO-Au NPs on promoting neuronal differentiation and neurite growth was split into two chapters based the stimulation type, i.e. magnetic stimulation (chapter 4) and light stimulation (chapter 5). In chapter 4, we modified the method of synthesizing SPIO-Au NPs (D: 20.8 ± 2.7 nm) combining co-precipitation with iterative hydroxylamine seeding method, and then functionalized SPIO-Au NPs with NGF. The light absorbance and zeta potential measurement confirmed the successful functionalization of NGF with NPs. As the prerequisite of bio-applications, we evaluated the biocompatibility of NGF-SPIO-Au NPs in PC-12 cells. The viability results (> 96%) indicated the excellent biocompatibility of SPIO-Au NPs. The TEM images of PC-12 cells treated with NGF-SPIO-Au NPs showed that the cellular uptake can be enhanced by the functionalization of NGF. Then a noninvasive magnetic stimulation technique was developed by applying dynamic MFs on cells treated with NGF-SPIO-Au NPs. Our results showed that this multifunctional nanomedicine was able to effectively stimulate and promote neuronal growth. The dynamic MF was favored, as it drove the neurite stretching more efficiently than that of the static MF. Also a cytoskeleton force model was created, which agrees well with our experimental data of neurite elongation and orientation. This study confirmed the potential of non-invasive magnetic neuron stimulation technique synergistically combining the biocompatible magnetic NGF-SPIO-Au NPs with dynamic MFs for promoting neuronal growth.

In chapter 5, we reported a novel non-invasive neuroregeneration approach of using low-intensity LED light to irradiate NGF-SPIO-Au NPs, a promising nanomedicine, to remarkably induce neuronal differentiation and neurite outgrowth in an intensity-

dependent manner. LEDs of higher intensities were favored to produce more differentiated cells, more branching points and longer neurite length. No severe toxicity was observed upon LED light irradiation at our measured intensities. In particular, NGF-SPIO-Au NPs irradiated by LED light of 1.90 mW/cm^2 were found to induce the calcium influx in the neurites and upregulate a neural differentiation specific marker β3-tubulin and an adhesive molecule integrin β1. These results demonstrated a promising non-invasive nanomedicine-based neurogenesis induction scheme using low intensity LED irradiated NGF-SPIO-Au NPs for nerve regeneration.

We have also checked the potential of SPIO-Au NPs for bone tissue regeneration as shown in Appendix B. We found that SPIO-Au NPs (10, 20, 40 and 80 μg/mL) didn't induce acute toxicity for up to 7 days of incubation. The existence of SPIO-Au NPs did not affect the proliferation of MC3T3-E1 cells at the concentration range between 1 and 40 μg/mL. The TEM results revealed the cellular uptake of SPIO-Au NPs through endocytosis and the dose-dependence of the internalization of NPs into cells. The enhanced ALP activity level of cells treated by NPs implied their potential in promoting the osteogenic differentiation of MC3T3-E1 cells which suggested another possible application of SPIO-Au NPs for bone tissue regeneration.

To summarize, in the current work, we have demonstrated the effectiveness of electromagnetic fields on stimulating neuronal differentiation and regulating neuronal activities through activating the magneto-plasmonic SPIO-Au NPs. However it is still limited for brain tissue regeneration and repair due to the insufficient exploration of the intracellular internalization and localization mechanism and the low photothermal

modulation efficiency: visible light cannot penetrate deep inside brain tissue, but near-infrared (NIR) light, which can penetrate deeper, has a very low photothermal effect on these NPs. Therefore one of the future improvement is to explore how the surface chemistry and electronic properties of SPIO-Au NPs are related to their interactions with neurons and affect their intracellular localization at targeted organelles. It is known that the cellular internalization can be affected by the different surface charge of NPs. For instance, the cationic Au NPs tend to pass through the cell membrane by direct diffusion, whereas anionic Au NPs enter a cell through endocytosis.[140,141] For efficient drug delivery, direct diffusion is preferred as NPs tend to aggregate together during endocytosis pathway and are strictly confined to the endosomes, which restricts the interaction between NPs and cell organelles compared to freely dispersed NPs in the cytosol by direct diffusion.[142] Therefore the surface modification needs to be optimized in surface charge type and density to balance the delivery efficiency and minimize the cytotoxicity. For this purpose, SPIO-Au NPs can be functionalized with various ligands. It will be interesting to explore how the surface functionality of NPs affect the NPs – cells interaction and the behavior of NPs.

To overcome the limitation of restricted tissue penetration depth of 525 nm LED light and move forward to *in vivo* validation, the NGF-SPIO-Au NPs can also be stimulated by micro or nano-LED fibers, which have been developed very well *in vivo*,[143,144] allowing the wireless optogenetic manipulation of neuronal activities in animals.

89

For the further validation of light-stimulation and magnetic stimulation of SPIO-Au NPs for nerve regeneration on an animal model, it is also necessary to perform some preliminary *in vivo* examinations to explore the biodistribution, the in vivo toxicity as well as the half-life of SPIO-Au NPs. These data will be very useful for evaluating the dosage and duration time of SPIO-Au NPs for the effective stimulation of brain in animal test.

REFERENCES

1.   Riggio C, Calatayud MP, Giannaccini M, Sanz B, Torres TE, Fernández-Pacheco R, Ripoli A, Ibarra MR, Dente L, Cuschieri A. The orientation of the neuronal growth process can be directed via magnetic nanoparticles under an applied magnetic field. *Nanomed Nanotech Biol Med.* 2014;10(7):1549-1558.

2.   Huang EJ, Reichardt LF. Neurotrophins: roles in neuronal development and function. *Annu Rev Neurosci.* 2001;24(1):677-736.

3.   Marcus M, Skaat H, Alon N, Margel S, Shefi O. NGF-conjugated iron oxide nanoparticles promote differentiation and outgrowth of PC12 cells. *Nanoscale.* 2015;7(3):1058-1066.

4.   Wang L, Luo J, Maye MM, Fan Q, Rendeng Q, Engelhard MH, Wang C, Lin Y, Zhong C-J. Iron oxide–gold core–shell nanoparticles and thin film assembly. *J Mater Chem.* 2005;15(18):1821-1832.

5.   Wang L, Park H-Y, Lim SII, Schadt MJ, Mott D, Luo J, Wang X, Zhong C-J. Core@shell nanomaterials: gold-coated magnetic oxide nanoparticles. *J Mater Chem.* 2008;18(23):2629-2635.

6.   Xu Z, Hou Y, Sun S. Magnetic Core/Shell Fe3O4/Au and Fe3O4/Au/Ag Nanoparticles with Tunable Plasmonic Properties. *J Am Chem Soc.* 2007;129(28):8698-8699.

7.   Zhang S, Qi Y, Yang H, Gong M, Zhang D, Zou L. Optimization of the composition of bimetallic core/shell Fe2O3/Au nanoparticles for MRI/CT dual-mode imaging. *J Nanopart Res.* 2013;15(11):1-9.

8.   Zhang S, Zou L, Zhang D, Pang X, Yang H, Xu Y. GoldMag nanoparticles with core/shell structure: characterization and application in MR molecular imaging. *J Nanopart Res.* 2011;13(9):3867-3876.

9.   Tian Q, Hu J, Zhu Y, Zou R, Chen Z, Yang S, Li R, Su Q, Han Y, Liu X. Sub-10 nm Fe3O4@Cu2–xS Core–Shell Nanoparticles for Dual-Modal Imaging and Photothermal Therapy. *J Am Chem Soc.* 2013;135(23):8571-8577.

10.   Koppolu B, Bhavsar Z, Wadajkar AS, Nattama S, Rahimi M, Nwariaku F, Nguyen KT. Temperature-sensitive polymer-coated magnetic nanoparticles as a potential drug delivery system for targeted therapy of thyroid cancer. *J Biomed Nanotechnol.* 2012;8(6):983-990.

11.   Lee N, Hyeon T. Designed synthesis of uniformly sized iron oxide nanoparticles for efficient magnetic resonance imaging contrast agents. *Chem Soc Rev.* 2012;41(7):2575-2589.

12.   Yoffe S, Leshuk T, Everett P, Gu F. Superparamagnetic iron oxide nanoparticles (SPIONs): synthesis and surface modification techniques for use with MRI and other biomedical applications. *Curr Pharm Des.* 2013;19(3):493-509.

13.   Ramaswamy S, Greco JB, Uluer MC, Zhang Z, Zhang Z, Fishbein KW, Spencer RG. Magnetic resonance imaging of chondrocytes labeled with superparamagnetic iron oxide nanoparticles in tissue-engineered cartilage. *Tissue Eng Part A.* 2009;15(12):3899-3910.

14.   Saldanha KJ, Doan RP, Ainslie KM, Desai TA, Majumdar S. Micrometer-sized iron oxide particle labeling of mesenchymal stem cells for magnetic resonance

imaging-based monitoring of cartilage tissue engineering. *Magn Reson Imaging.* 2011;29(1):40-49.

15. Lalande C, Miraux S, Derkaoui SM, Mornet S, Bareille R, Fricain J-C, Franconi J-M, Le Visage C, Letourneur D, Amédée J. Magnetic resonance imaging tracking of human adipose derived stromal cells within three-dimensional scaffolds for bone tissue engineering. *Eur Cell Mater.* 2011;21(341):e54.

16. Nam SY, Ricles LM, Suggs LJ, Emelianov SY. Imaging strategies for tissue engineering applications. *Tissue Eng Part B Rev.* 2014;21(1):88-102.

17. Singh N, Jenkins GJS, Asadi R, Doak SH. Potential toxicity of superparamagnetic iron oxide nanoparticles (SPION). *Nano Rev.* 2010;1.

18. Cheng Y, Morshed RA, Auffinger B, Tobias AL, Lesniak MS. Multifunctional nanoparticles for brain tumor imaging and therapy. *Adv Drug Deliv Rev.* 2014;66(0):42-57.

19. Cherukuri P, Glazer ES, Curley SA. Targeted Hyperthermia Using Metal Nanoparticles. *Adv Drug Deliv Rev.* 2010;62(3):339-345.

20. Kumar CSSR, Mohammad F. Magnetic nanomaterials for hyperthermia-based therapy and controlled drug delivery. *Adv Drug Deliv Rev.* 2011;63(9):789-808.

21. Mahmoudi M, Hofmann H, Rothen-Rutishauser B, Petri-Fink A. Assessing the in vitro and in vivo toxicity of superparamagnetic iron oxide nanoparticles. *Chem Rev.* 2011;112(4):2323-2338.

22. Yan H, Teh C, Sreejith S, Zhu L, Kwok A, Fang W, Ma X, Nguyen KT, Korzh V, Zhao Y. Functional mesoporous silica nanoparticles for photothermal‐controlled drug delivery in vivo. *Angew Chem Int Ed.* 2012;51(33):8373-8377.

23. Pinkernelle J, Raffa V, Calatayud MP, Goya GF, Riggio C, Keilhoff G. Growth factor choice is critical for successful functionalization of nanoparticles. *Front Neurosci.* 2015;9.

24. Phan AD, Hoang TX, Nghiem THL, Woods LM. Surface plasmon resonances of protein-conjugated gold nanoparticles on graphitic substrates. *Appl Phys Lett.* 2013;103(16):163702.

25. Mahmoudi M, Sant S, Wang B, Laurent S, Sen T. Superparamagnetic iron oxide nanoparticles (SPIONs): development, surface modification and applications in chemotherapy. *Adv Drug Deliv Rev.* 2011;63(1):24-46.

26. Laurent S, Forge D, Port M, Roch A, Robic C, Vander Elst L, Muller RN. Magnetic iron oxide nanoparticles: synthesis, stabilization, vectorization, physicochemical characterizations, and biological applications. *Chem Rev.* 2008;108(6):2064-2110.

27. Llevot A, Astruc D. Applications of vectorized gold nanoparticles to the diagnosis and therapy of cancer. *Chem Soc Rev.* 2012;41(1):242-257.

28. Hainfeld JF, Lin L, Slatkin DN, Avraham Dilmanian F, Vadas TM, Smilowitz HM. Gold nanoparticle hyperthermia reduces radiotherapy dose. *Nanomed Nanotech Biol Med.* 2014;10(8):1609-1617.

29. Deatsch AE, Evans BA. Heating efficiency in magnetic nanoparticle hyperthermia. *J Magn Magn Mater.* 2014;354:163-172.

30. Lal S, Clare SE, Halas NJ. Nanoshell-Enabled Photothermal Cancer Therapy: Impending Clinical Impact. *Acc Chem Res.* 2008;41(12):1842-1851.

31. Maltzahn Gv, Park J-H, Agrawal A, Bandaru NK, Das SK, Sailor MJ, Bhatia SN. Computationally Guided Photothermal Tumor Therapy Using Long-Circulating Gold Nanorod Antennas. *Cancer Res.* 2009;69(9):3892-3900.

32. O'Neal DP, Hirsch LR, Halas NJ, Payne JD, West JL. Photo-thermal tumor ablation in mice using near infrared-absorbing nanoparticles. *Cancer Lett.* 2004;209(2):171-176.

33. Biju V. Chemical modifications and bioconjugate reactions of nanomaterials for sensing, imaging, drug delivery and therapy. *Chem Soc Rev.* 2014;43(3):744-764.

34. Alkilany AM, Thompson LB, Boulos SP, Sisco PN, Murphy CJ. Gold nanorods: Their potential for photothermal therapeutics and drug delivery, tempered by the complexity of their biological interactions. *Adv Drug Deliv Rev.* 2012;64(2):190-199.

35. Kang B, Mackey MA, El-Sayed MA. Nuclear targeting of gold nanoparticles in cancer cells induces DNA damage, causing cytokinesis arrest and apoptosis. *J Am Chem Soc.* 2010;132(5):1517-1519.

36. Khlebtsov N, Dykman L. Biodistribution and toxicity of engineered gold nanoparticles: a review of in vitro and in vivo studies. *Chem Soc Rev.* 2011;40(3):1647-1671.

37. Ojea-Jiménez I, Romero FM, Bastús NG, Puntes V. Small Gold Nanoparticles Synthesized with Sodium Citrate and Heavy Water: Insights into the Reaction Mechanism. *J Phys Chem C.* 2010;114(4):1800-1804.

38. Zhou H, Zou F, Koh K, Lee J. Multifunctional magnetoplasmonic nanomaterials and their biomedical applications. *J Biomed Nanotechnol.* 2014;10(10):2921-2949.

39. Maleki H, Simchi A, Imani M, Costa B. Size-controlled synthesis of superparamagnetic iron oxide nanoparticles and their surface coating by gold for biomedical applications. *J Magn Magn Mater.* 2012;324(23):3997-4005.

40. Conde J, Ambrosone A, Sanz V, Hernandez Y, Marchesano V, Tian F, Child H, Berry CC, Ibarra MR, Baptista PV. Design of multifunctional gold nanoparticles for in vitro and in vivo gene silencing. *Acs Nano.* 2012;6(9):8316-8324.

41. Saha K, Agasti SS, Kim C, Li X, Rotello VM. Gold nanoparticles in chemical and biological sensing. *Chem Rev.* 2012;112(5):2739-2779.

42. Ma X, Cheng Y, Huang Y, Tian Y, Wang S, Chen Y. PEGylated gold nanoprisms for photothermal therapy at low laser power density. *RSC Adv.* 2015;5(99):81682-81688.

43. Morrow BJ, Matijević E, Goia DV. Preparation and stabilization of monodisperse colloidal gold by reduction with aminodextran. *J Colloid Interface Sci.* 2009;335(1):62-69.

44. Mayer ABR, Mark JE. Colloidal gold nanoparticles protected by water-soluble homopolymers and random copolymers. *Eur Polym J.* 1998;34(1):103-108.

45. Kawazoe N, Chen G. Gold nanoparticles with different charge and moiety induce differential cell response on mesenchymal stem cell osteogenesis. *Biomaterials.* 2015;54:226-236.

46. Ji X, Shao R, Elliott AM, Stafford RJ, Esparza-Coss E, Bankson JA, Liang G, Luo Z-P, Park K, Markert JT. Bifunctional gold nanoshells with a superparamagnetic iron oxide-silica core suitable for both MR imaging and photothermal therapy. *J Phys Chem C.* 2007;111(17):6245-6251.

47. Kong L, Alves CS, Hou W, Qiu J, Möhwald H, Tomás H, Shi X. RGD peptide-modified dendrimer-entrapped gold nanoparticles enable highly efficient and specific gene delivery to stem cells. *ACS Appl Mater Interfaces.* 2015;7(8):4833-4843.

48. Muroski ME, Morgan Jr TJ, Levenson CW, Strouse GF. A gold nanoparticle pentapeptide: gene fusion to induce therapeutic gene expression in mesenchymal stem cells. *J Am Chem Soc.* 2014;136(42):14763-14771.

49. Dreaden EC, Alkilany AM, Huang X, Murphy CJ, El-Sayed MA. The golden age: gold nanoparticles for biomedicine. *Chem Soc Rev.* 2012;41(7):2740-2779.

50. Ricles LM, Nam SY, Trevino EA, Emelianov SY, Suggs LJ. A dual gold nanoparticle system for mesenchymal stem cell tracking. *J Mater Chem B.* 2014;2(46):8220-8230.

51. Richardson HH, Carlson MT, Tandler PJ, Hernandez P, Govorov AO. Experimental and Theoretical Studies of Light-to-Heat Conversion and Collective Heating Effects in Metal Nanoparticle Solutions. *Nano Lett.* 2009;9(3):1139-1146.

52.   Roper DK, Ahn W, Hoepfner M. Microscale Heat Transfer Transduced by Surface Plasmon Resonant Gold Nanoparticles. *J Phys Chem C.* 2007;111(9):3636-3641.

53.   Jiang K, Smith DA, Pinchuk A. Size-Dependent Photothermal Conversion Efficiencies of Plasmonically Heated Gold Nanoparticles. *J Phys Chem C.* 2013;117(51):27073-27080.

54.   Yang S-C, Fischer W-J, Yang T-L. Size-controllable micro-bubble generation using a nanoimprinted plasmonic nanopillar array absorber in the near-infrared region. *Appl Phys Lett.* 2016;108(18):183105.

55.   Palermo G, Cataldi U, De Sio L, Bürgi T, Tabiryan N, Umeton C. Optical control of plasmonic heating effects using reversible photo-alignment of nematic liquid crystals. *Appl Phys Lett.* 2016;109(19):191906.

56.   Polf JC, Bronk LF, Driessen WHP, Arap W, Pasqualini R, Gillin M. Enhanced relative biological effectiveness of proton radiotherapy in tumor cells with internalized gold nanoparticles. *Appl Phys Lett.* 2011;98(19):193702.

57.   Fan Z, Senapati D, Singh AK, Ray PC. Theranostic magnetic core–plasmonic shell star shape nanoparticle for the isolation of targeted rare tumor cells from whole blood, fluorescence imaging, and photothermal destruction of cancer. *Mol Pharm.* 2012;10(3):857-866.

58.   Havrdova M, Polakova K, Skopalik J, Vujtek M, Mokdad A, Homolkova M, Tucek J, Nebesarova J, Zboril R. Field emission scanning electron microscopy (FE-SEM) as an approach for nanoparticle detection inside cells. *Micron.* 2014;67(0):149-154.

59.   Mustafa T, Watanabe F, Monroe W, Mahmood M, Xu Y, Saeed LM, Karmakar A, Casciano D, All S, Biris AS. Impact of gold nanoparticle concentration on their cellular uptake by MC3T3-E1 mouse osteoblastic cells as analyzed by transmission electron microscopy. *J Nanomed Nanotechnol.* 2011;2(6):1000118.

60.   Bastús NG, Comenge J, Puntes V. Kinetically Controlled Seeded Growth Synthesis of Citrate-Stabilized Gold Nanoparticles of up to 200 nm: Size Focusing versus Ostwald Ripening. *Langmuir.* 2011;27(17):11098-11105.

61.   Turkevich J, Stevenson PC, Hillier J. A study of the nucleation and growth processes in the synthesis of colloidal gold. *Discuss Faraday Soc.* 1951;11(0):55-75.

62.   Lyon JL, Fleming DA, Stone MB, Schiffer P, Williams ME. Synthesis of Fe oxide core/Au shell nanoparticles by iterative hydroxylamine seeding. *Nano Lett.* 2004;4(4):719-723.

63.   Fan Z, Shelton M, Singh AK, Senapati D, Khan SA, Ray PC. Multifunctional Plasmonic Shell–Magnetic Core Nanoparticles for Targeted Diagnostics, Isolation, and Photothermal Destruction of Tumor Cells. *ACS Nano.* 2012;6(2):1065-1073.

64.   Montazeri H, Amani A, Shahverdi HR, al din Haratifar E, Shahverdi AR. Separation of the defect-free Fe3O4-Au core/shell fraction from magnetite-gold composite nanoparticles by an acid wash treatment. *Journal of Nanostructure in Chemistry.* 2013;3(1):1-6.

65. Vallejo-Fernandez G, Whear O, Roca AG, Hussain S, Timmis J, Patel V, O'Grady K. Mechanisms of hyperthermia in magnetic nanoparticles. *J Phys D: Appl Phys.* 2013;46(31):312001.

66. Feng W, Zhou X, Nie W, Chen L, Qiu K, Zhang Y, He C. Au/polypyrrole@ Fe3O4 nanocomposites for MR/CT dual-modal imaging guided-photothermal therapy: an in vitro study. *ACS Appl Mater Interfaces.* 2015;7(7):4354-4367.

67. Hu R, Zheng M, Wu J, Li C, Shen D, Yang D, Li L, Ge M, Chang Z, Dong W. Core-Shell Magnetic Gold Nanoparticles for Magnetic Field-Enhanced Radio-Photothermal Therapy in Cervical Cancer. *Nanomaterials.* 2017;7(5):111.

68. Wang Y, Zhang F, Wang Q, Yang P, Lin H, Qu F. Hierarchical MoSe 2 nanoflowers as novel nanocarriers for NIR-light-mediated synergistic photo-thermal/dynamic and chemo-therapy. *Nanoscale.* 2018;10(30):14534-14545.

69. Dulkeith E, Niedereichholz T, Klar TA, Feldmann J, von Plessen G, Gittins DI, Mayya KS, Caruso F. Plasmon emission in photoexcited gold nanoparticles. *Physical Review B.* 2004;70(20):205424.

70. Connor EE, Mwamuka J, Gole A, Murphy CJ, Wyatt MD. Gold Nanoparticles Are Taken Up by Human Cells but Do Not Cause Acute Cytotoxicity. *Small.* 2005;1(3):325-327.

71. Albanese A, Chan WCW. Effect of Gold Nanoparticle Aggregation on Cell Uptake and Toxicity. *ACS Nano.* 2011;5(7):5478-5489.

72.   Pauksch L, Hartmann S, Rohnke M, Szalay G, Alt V, Schnettler R, Lips KS. Biocompatibility of silver nanoparticles and silver ions in primary human mesenchymal stem cells and osteoblasts. *Acta biomater.* 2014;10(1):439-449.

73.   Gordon T. The physiology of neural injury and regeneration: The role of neurotrophic factors. *J Commun Disord.* 2010;43(4):265-273.

74.   Dickson BJ. Molecular mechanisms of axon guidance. *Science.* 2002;298(5600):1959-1964.

75.   Alunni A, Bally-Cuif L. A comparative view of regenerative neurogenesis in vertebrates. *Development.* 2016;143(5):741-753.

76.   Lampe KJ, Antaris AL, Heilshorn SC. Design of three-dimensional engineered protein hydrogels for tailored control of neurite growth. *Acta biomater.* 2013;9(3):5590-5599.

77.   Yu N-K, Kim HF, Shim J, Kim S, Kim DW, Kwak C, Sim S-E, Choi J-H, Ahn S, Yoo J. A transducible nuclear/nucleolar protein, mLLP, regulates neuronal morphogenesis and synaptic transmission. *Sci Rep.* 2016;6.

78.   Babensee JE, McIntire LV, Mikos AG. Growth factor delivery for tissue engineering. *Pharm Res.* 2000;17(5):497-504.

79.   Faroni A, Mobasseri SA, Kingham PJ, Reid AJ. Peripheral nerve regeneration: experimental strategies and future perspectives. *Adv Drug Deliv Rev.* 2015;82:160-167.

80.   Orive G, Anitua E, Pedraz JL, Emerich DF. Biomaterials for promoting brain protection, repair and regeneration. *Nature reviews Neuroscience.* 2009;10(9):682.

81.   Morelli S, Piscioneri A, Messina A, Salerno S, Al‐Fageeh MB, Drioli E, Bartolo
      LD. Neuronal growth and differentiation on biodegradable membranes. *J Tissue
      Eng Regen Med.* 2015;9(2):106-117.

82.   Aloe L, Rocco ML, Bianchi P, Manni L. Nerve growth factor: from the early
      discoveries to the potential clinical use. *J Transl Med.* 2012;10(1):239.

83.   Ziv-Polat O, Shahar A, Levy I, Skaat H, Neuman S, Fregnan F, Geuna S, Grothe
      C, Haastert-Talini K, Margel S. The role of neurotrophic factors conjugated to iron
      oxide nanoparticles in peripheral nerve regeneration: in vitro studies. *BioMed
      research international.* 2014;2014.

84.   Lee K, Silva EA, Mooney DJ. Growth factor delivery-based tissue engineering:
      general approaches and a review of recent developments. *J R Soc Interface.*
      2011;8(55):153-170.

85.   Anitua E, Sánchez M, Orive G, Andia I. Delivering growth factors for therapeutics.
      Trends Pharmacol Sci. 2008;29(1):37-41.

86.   Pilakka-Kanthikeel S, Atluri VSR, Sagar V, Saxena SK, Nair M. Targeted brain
      derived neurotropic factors (BDNF) delivery across the blood-brain barrier for
      neuro-protection using magnetic nano carriers: an in-vitro study. *PLoS One.*
      2013;8(4):e62241.

87.   Kim JA, Lee N, Kim BH, Rhee WJ, Yoon S, Hyeon T, Park TH. Enhancement of
      neurite outgrowth in PC12 cells by iron oxide nanoparticles. *Biomaterials.*
      2011;32(11):2871-2877.

88.   Marcus M, Karni M, Baranes K, Levy I, Alon N, Margel S, Shefi O. Iron oxide nanoparticles for neuronal cell applications: uptake study and magnetic manipulations. *J Nanobiotechnology.* 2016;14(1):37.

89.   Bodelon G, Costas C, Perez-Juste J, Pastoriza-Santos I, Liz-Marzan LM. Gold nanoparticles for regulation of cell function and behavior. *Nano Today.* 2017;13:40-60.

90.   Yuan M, Wang Y, Qin Y-X. Promoting neuroregeneration by applying dynamic magnetic fields to a novel nanomedicine: Superparamagnetic iron oxide (SPIO)-gold nanoparticles bounded with nerve growth factor (NGF). *Nanomed Nanotech Biol Med.* 2018;14(4):1337-1347.

91.   Sood A, Arora V, Shah J, Kotnala RK, Jain TK. Multifunctional gold coated iron oxide core-shell nanoparticles stabilized using thiolated sodium alginate for biomedical applications. *Materials Science and Engineering: C.* 2017;80:274-281.

92.   Karamipour S, Sadjadi MS, Farhadyar N. Fabrication and spectroscopic studies of folic acid-conjugated Fe3O4@ Au core–shell for targeted drug delivery application. *Spectrochimica Acta Part A: Molecular and Biomolecular Spectroscopy.* 2015;148:146-155.

93.   Ghaznavi H, Hosseini-Nami S, Kamrava SK, Irajirad R, Maleki S, Shakeri-Zadeh A, Montazerabadi A. Folic acid conjugated PEG coated gold–iron oxide core–shell nanocomplex as a potential agent for targeted photothermal therapy of cancer. *Artificial cells, nanomedicine, and biotechnology.* 2018;46(8):1594-1604.

94. Han L, Zhang Y, Zhang Y, Shu Y, Chen X-W, Wang J-H. A magnetic polypyrrole/iron oxide core/gold shell nanocomposite for multimodal imaging and photothermal cancer therapy. *Talanta.* 2017;171:32-38.

95. Li J, Hu Y, Yang J, Wei P, Sun W, Shen M, Zhang G, Shi X. Hyaluronic acid-modified Fe3O4@ Au core/shell nanostars for multimodal imaging and photothermal therapy of tumors. *Biomaterials.* 2015;38:10-21.

96. Kukreja A, Kang B, Kim H-O, Jang E, Son HY, Huh Y-M, Haam S. Preparation of gold core-mesoporous iron-oxide shell nanoparticles and their application as dual MR/CT contrast agent in human gastric cancer cells. *Journal of industrial and engineering chemistry.* 2017;48:56-65.

97. Sabale S, Kandesar P, Jadhav V, Komorek R, Motkuri RK, Yu X-Y. Recent developments in the synthesis, properties, and biomedical applications of core/shell superparamagnetic iron oxide nanoparticles with gold. *Biomaterials science.* 2017;5(11):2212-2225.

98. Marino A, Genchi GG, Mattoli V, Ciofani G. Piezoelectric nanotransducers: The future of neural stimulation. *Nano Today.* 2017;14:9-12.

99. Tsao JY, Schubert EF, Fouquet R, Lave M. The electrification of energy: Long-term trends and opportunities. *MRS Energy & Sustainability.* 2018;5.

100. Pattison PM, Tsao JY, Brainard GC, Bugbee B. LEDs for photons, physiology and food. *Nature.* 2018;563(7732):493.

101. Miesenböck G. Genetic methods for illuminating the function of neural circuits. *Curr Opin Neurobiol.* 2004;14(3):395-402.

102. Yong J, Needham K, Brown WGA, Nayagam BA, McArthur SL, Yu A, Stoddart PR. Gold‑Nanorod‑Assisted Near‑Infrared Stimulation of Primary Auditory Neurons. *Advanced healthcare materials.* 2014;3(11):1862-1868.

103. Eom K, Kim J, Choi JM, Kang T, Chang JW, Byun KM, Jun SB, Kim SJ. Enhanced infrared neural stimulation using localized surface plasmon resonance of gold nanorods. *Small.* 2014;10(19):3853-3857.

104. Lee JW, Jung H, Cho HH, Lee JH, Nam Y. Gold nanostar-mediated neural activity control using plasmonic photothermal effects. *Biomaterials.* 2018;153:59-69.

105. Lavoie-Cardinal F, Salesse C, Bergeron É, Meunier M, De Koninck P. Gold nanoparticle-assisted all optical localized stimulation and monitoring of Ca2+ signaling in neurons. *Sci Rep.* 2016;6.

106. Chen N, Tian L, Patil AC, Peng S, Yang IH, Thakor NV, Ramakrishna S. Neural interfaces engineered via micro-and nanostructured coatings. *Nano Today.* 2017;14:59-83.

107. Paviolo C, Haycock JW, Yong J, Yu A, Stoddart PR, McArthur SL. Laser exposure of gold nanorods can increase neuronal cell outgrowth. *Biotechnol Bioeng.* 2013;110(8):2277-2291.

108. Gasperini RJ, Pavez M, Thompson AC, Mitchell CB, Hardy H, Young KM, Chilton JK, Foa L. How does calcium interact with the cytoskeleton to regulate growth cone motility during axon pathfinding? *Molecular and Cellular Neuroscience.* 2017;84:29-35.

109. Yuan M, Wang Y, Qin YX. SPIO‑Au core‑shell nanoparticles for promoting osteogenic differentiation of MC3T3‑E1 cells: Concentration‑dependence study. *J Biomed Mater Res A.* 2017;105(12):3350-3359.

110. Yeh NG, Wu C-H, Cheng TC. Light-emitting diodes—Their potential in biomedical applications. *Renewable and Sustainable Energy Reviews.* 2010;14(8):2161-2166.

111. Mills E. The specter of fuel-based lighting. *Science.* 2005;308(5726):1263-1264.

112. Whelan HT, Smits Jr RL, Buchman EV, Whelan NT, Turner SG, Margolis DA, Cevenini V, Stinson H, Ignatius R, Martin T. Effect of NASA light-emitting diode irradiation on wound healing. *J Clin Laser Med Surg.* 2001;19(6):305-314.

113. Rodrigues de Morais NC, Barbosa AM, Vale ML, Villaverde AB, de Lima CJ, Cogo JC, Zamuner SR. Anti-inflammatory effect of low-level laser and light-emitting diode in zymosan-induced arthritis. *Photomed Laser Surg.* 2010;28(2):227-232.

114. Barolet D. Light-emitting diodes (LEDs) in dermatology. *J Cutan Med Surg.* 2008;27(4):227-238.

115. Naeser MA, Saltmarche A, Krengel MH, Hamblin MR, Knight JA. Improved cognitive function after transcranial, light-emitting diode treatments in chronic, traumatic brain injury: two case reports. *Photomed Laser Surg.* 2011;29(5):351-358.

116. Serafim KGG, de Paula Ramos S, de Lima FM, Carandina M, Ferrari O, Dias IFL, de Oliveira Toginho Filho D, Siqueira CPCM. Effects of 940 nm light-emitting

diode (led) on sciatic nerve regeneration in rats. *Lasers Med Sci.* 2012;27(1):113-119.

117. Stroh A, Tsai HC, Wang LP, Zhang F, Kressel J, Aravanis A, Santhanam N, Deisseroth K, Konnerth A, Schneider MB. Tracking stem cell differentiation in the setting of automated optogenetic stimulation. *Stem Cells.* 2011;29(1):78-88.

118. Zhang Z, Tarone G, Turner DC. Expression of integrin alpha 1 beta 1 is regulated by nerve growth factor and dexamethasone in PC12 cells. Functional consequences for adhesion and neurite outgrowth. *J Biol Chem.* 1993;268(8):5557-5565.

119. Sun J, Longtin JP, Irvine Jr TF. Laser-based thermal pulse measurement of liquid thermophysical properties. *Int J Heat Mass Transfer.* 2001;44(3):645-657.

120. Hohenester U, Trügler A. MNPBEM–A Matlab toolbox for the simulation of plasmonic nanoparticles. *Comput Phys Commun.* 2012;183(2):370-381.

121. Sainsbury T, Ikuno T, Okawa D, Pacile D, Frechet JMJ, Zettl A. Self-assembly of gold nanoparticles at the surface of amine-and thiol-functionalized boron nitride nanotubes. *J Phys Chem C.* 2007;111(35):12992-12999.

122. Vijayakumar S. In vitro stability studies on gold nanoparticles with different stabilizing agents. *Int J Curr Sci.* 2014;11:84-93.

123. Laaksonen T, Ahonen P, Johans C, Kontturi K. Stability and Electrostatics of Mercaptoundecanoic Acid‐Capped Gold Nanoparticles with Varying Counterion Size. *Chemphyschem.* 2006;7(10):2143-2149.

124.   Yuan M, Wang Y, Qin YX. SPIO‑Au core‑shell nanoparticles for promoting osteogenic differentiation of MC3T3‑E1 cells: Concentration‑dependence study. *J Biomed Mater Res A.* 2017.

125.   Nam HY, Kwon SM, Chung H, Lee S-Y, Kwon S-H, Jeon H, Kim Y, Park JH, Kim J, Her S. Cellular uptake mechanism and intracellular fate of hydrophobically modified glycol chitosan nanoparticles. *J Control Release.* 2009;135(3):259-267.

126.   Darbyshire PM. Dynamics of Magnetic Nanoparticles in Newly Formed Microvascular Networks Surrounding Solid Tumours: A Parallel Programming Approach. *Cancer Research Journal* 2016;4(1):9-23.

127.   Masserini M. Nanoparticles for brain drug delivery. *ISRN Biochem.* 2013;2013.

128.   Yuan M, Wang Y, Hwang D, Longtin JP. Thermocouple-tip-exposing temperature assessment technique for evaluating photothermal conversion efficiency of plasmonic nanoparticles at low laser power density. *submitted to Review of Scientific Instruments.* 2019.

129.   Westerink RHS, Ewing AG. The PC12 cell as model for neurosecretion. *Acta Physiologica.* 2008;192(2):273-285.

130.   Pisanic Ii TR, Blackwell JD, Shubayev VI, Finones RR, Jin S. Nanotoxicity of iron oxide nanoparticle internalization in growing neurons. *Biomaterials.* 2007;28(16):2572-2581.

131.   Miyakoshi J. Effects of static magnetic fields at the cellular level. *Prog Biophys Mol Biol.* 2005;87(2-3):213-223.

132. Lai H, Singh NP. Magnetic-field-induced DNA strand breaks in brain cells of the rat. *Environ Health Perspect.* 2004;112(6):687.

133. Hashish AH, El-Missiry MA, Abdelkader HI, Abou-Saleh RH. Assessment of biological changes of continuous whole body exposure to static magnetic field and extremely low frequency electromagnetic fields in mice. *Ecotoxicol Environ Saf.* 2008;71(3):895-902.

134. Chernoff N, Rogers JM, Kavet R. A review of the literature on potential reproductive and developmental toxicity of electric and magnetic fields. *Toxicology.* 1992;74(2-3):91-126.

135. Ramadan LA, Abd-Allah ARA, Aly HAA, Saad-El-Din AA. Testicular toxicity effects of magnetic field exposure and prophylactic role of coenzyme Q10 and L-carnitine in mice. *Pharmacol Res.* 2002;46(4):363-370.

136. Dehmelt L, Halpain S. Actin and microtubules in neurite initiation: are MAPs the missing link? *Dev Neurobiol.* 2004;58(1):18-33.

137. Redondo PC, Harper AGS, Sage SO, Rosado JA. Dual role of tubulin-cytoskeleton in store-operated calcium entry in human platelets. *Cell Signal.* 2007;19(10):2147-2154.

138. Wang H-J, Wan A-R, Jauh G-Y. An actin-binding protein, LlLIM1, mediates calcium and hydrogen regulation of actin dynamics in pollen tubes. *Plant Physiol.* 2008;147(4):1619-1636.

139. Henley J, Poo M-m. Guiding neuronal growth cones using Ca2+ signals. *Trends Cell Biol.* 2004;14(6):320-330.

140. Lin J, Alexander-Katz A. Cell Membranes Open "Doors" for Cationic Nanoparticles/Biomolecules: Insights into Uptake Kinetics. *ACS Nano.* 2013;7(12):10799-10808.

141. Lin J, Zhang H, Chen Z, Zheng Y. Penetration of Lipid Membranes by Gold Nanoparticles: Insights into Cellular Uptake, Cytotoxicity, and Their Relationship. *ACS Nano.* 2010;4(9):5421-5429.

142. Nativo P, Prior IA, Brust M. Uptake and intracellular fate of surface-modified gold nanoparticles. *ACS nano.* 2008;2(8):1639-1644.

143. McCall JG, Kim T-i, Shin G, Huang X, Jung YH, Al-Hasani R, Omenetto FG, Bruchas MR, Rogers JA. Fabrication and application of flexible, multimodal light-emitting devices for wireless optogenetics. *Nat Protoc.* 2013;8(12):2413.

144. Cao H, Gu L, Mohanty SK, Chiao JC. An integrated μLED optrode for optogenetic stimulation and electrical recording. *IEEE Trans Biomed Eng.* 2012;60(1):225-229.

145. Heo DN, Ko W-K, Bae MS, Lee JB, Lee D-W, Byun W, Lee CH, Kim E-C, Jung B-Y, Kwon IK. Enhanced bone regeneration with a gold nanoparticle–hydrogel complex. *J Mater Chem B.* 2014;2(11):1584-1593.

146. Goldman EB, Zak A, Tenne R, Kartvelishvily E, Levin-Zaidman S, Neumann Y, Stiubea-Cohen R, Palmon A, Hovav A-H, Aframian DJ. Biocompatibility of tungsten disulfide inorganic nanotubes and fullerene-like nanoparticles with salivary gland cells. *Tissue Eng Part A.* 2014;21(5-6):1013-1023.

147. Chithrani BD, Ghazani AA, Chan WC. Determining the size and shape dependence of gold nanoparticle uptake into mammalian cells. *Nano Lett.* 2006;6(4):662-668.

148. Albanese A, Tang PS, Chan WCW. The effect of nanoparticle size, shape, and surface chemistry on biological systems. *Annual review of biomedical engineering.* 2012;14:1-16.

149. Cho EC, Au L, Zhang Q, Xia Y. The effects of size, shape, and surface functional group of gold nanostructures on their adsorption and internalization by cells. *Small.* 2010;6(4):517-522.

150. Yi C, Liu D, Fong C-C, Zhang J, Yang M. Gold nanoparticles promote osteogenic differentiation of mesenchymal stem cells through p38 MAPK pathway. *Acs Nano.* 2010;4(11):6439-6448.

151. Dashnyam K, Perez RA, Singh RK, Lee E-J, Kim H-W. Hybrid magnetic scaffolds of gelatin–siloxane incorporated with magnetite nanoparticles effective for bone tissue engineering. *RSC Adv.* 2014;4(77):40841-40851.

152. Qiu K, Chen B, Nie W, Zhou X, Feng W, Wang W, Chen L, Mo X, Wei Y, He C. Electrophoretic Deposition of Dexamethasone-loaded Mesoporous Silica Nanoparticles onto Poly (L-lactic acid)/Poly (ε–caprolactone) Composite Scaffold for Bone Tissue Engineering. *ACS applied materials & interfaces %@ 1944-8244.* 2016.

153. Park JS, Yang HN, Woo DG, Chung H-M, Park K-H. In Vitro and In Vivo Chondrogenesis of Rabbit Bone Marrow–Derived Stromal Cells in Fibrin Matrix

Mixed with Growth Factor Loaded in Nanoparticles. *Tissue Eng Part A.* 2009;15(8):2163-2175.

154.   Zheng F, Wang S, Wen S, Shen M, Zhu M, Shi X. Characterization and antibacterial activity of amoxicillin-loaded electrospun nano-hydroxyapatite/poly (lactic-co-glycolic acid) composite nanofibers. *Biomaterials.* 2013;34(4):1402-1412.

155.   Ganesh N, Ashokan A, Rajeshkannan R, Chennazhi K, Koyakutty M, Nair SV. Magnetic resonance functional nano-hydroxyapatite incorporated poly (caprolactone) composite scaffolds for in situ monitoring of bone tissue regeneration by MRI. *Tissue Eng Part A.* 2014;20(19-20):2783-2794.

APPENDIX A

ELECTROMAGNETIC STIMULATION USING STATIC n42 MAGNETIC FIELDS

FOR NEUROREGENERATION (PC-12 CELLS)[*]

The determination of the concentration of SPIO-Au NPs

The calculation of the final concentration of SPIO-Au NPs is based on the original mass of materials used in the synthesis process. As shown in table A1, the mass amount of SPIO used is 1.32 mg, while the mass amount of Au is 2.9 mg. So the total mass concentration of SPIO-Au NPs is 422 µg/ml (in 10 ml DI water).

Table A1. The calculation of SPIO-Au concentration. Reprinted with permission from reference 90.

Fe (mmol)	Fe_2O_3 (mmol)	SPIO conc. (mM)	SPIO diluted (mM)	SPIO ($*10^{-3}$ mmol)	Au ($*10^{-3}$ mmol)	SPIO (mg)	Au (mg)	Total conc. (µg/ml)
15	7.5	60	1.5	8.25	14.7	1.32	2.9	422

N42 static magnetic applicator-set-up and results

As shown in the inset of Figure A1, the static magnetic applicator was composed by eight N52 NdFeB magnetic cubes of 0.5 inch arranged in a Halbach array. The magnetic strength along the diameter of the magnetic applicator was simulated from FEM

---

[*] Reprinted with permission from "Promoting neuroregeneration by applying dynamic magnetic fields to a novel nanomedicine: Superparamagnetic iron oxide (SPIO)-gold nanoparticles bounded with nerve growth factor (NGF)" by Yuan M, Wang Y, Qin Y-X, 2018. Nanomed Nanotech Biol Med, 14(4):1337-1347. Copyright [2019] by Elsevier.

modeling and then experimentally measured using a F.W. Bell 8010 gauss/tesla meter (Figure A1), confirming the theoretical simulation.

An average magnetic field gradient of -23.28 T/m was calculated from the FEM modeling (Figure A1). Cells were seeded at the density of $5*10^4$ cells/dish in PLL pre-coated Ibidi Petri dishes (D: 35mm). After 24 h, the medium was replaced by fresh serum reduced medium containing NGF-SPIO-Au NPs at the concentration of 10 μg/ml. Cells were incubated for 24 h to let the NPs to interact with cells. Then the Petri dish was put inside the N42 static magnetic applicator.

Two groups of cells were prepared (control (Control-MF-), static (N42-static-MF+)). After 1 day, a light microscope (Axiovert 200M Inverted Fluorescence/phase Contrast Microscope (Carl Zeiss Inc.) equipped with an AxioCam CCD camera) was used to capture the images of differentiated cells. The neurite length, number and angle theta between the direction of the neurite and the magnetic force (0 degree) in each image were measured using Simple Neurite Tracer as a plugin of Fiji. The results were shown in Figure A2 and Figure A3.
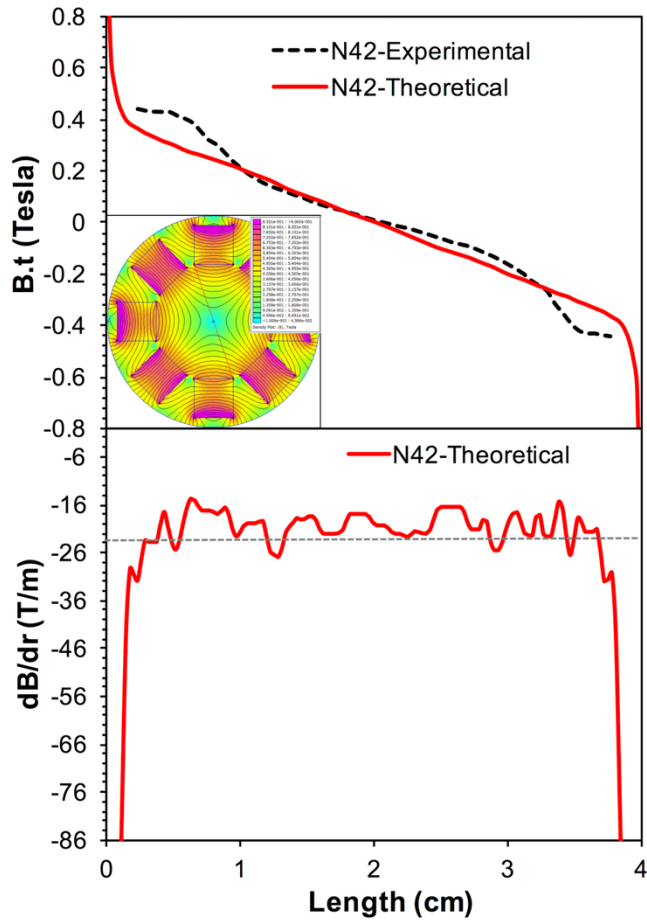
Figure A1. Finite element modeling result (theoretical) and the experimental measurement result of the flux density distribution inside the N42 Halbach-like magnetic applicator. The top figure is the tangential flux density B(T) and the bottom figure is the derivative dB/dr (T/m) along the radial direction inside the Halbach-like magnetic applicator. The dot line in the bottom figure represents the average value of dB/dr, which is -23.28 T/m. Reprinted with permission from reference 90.
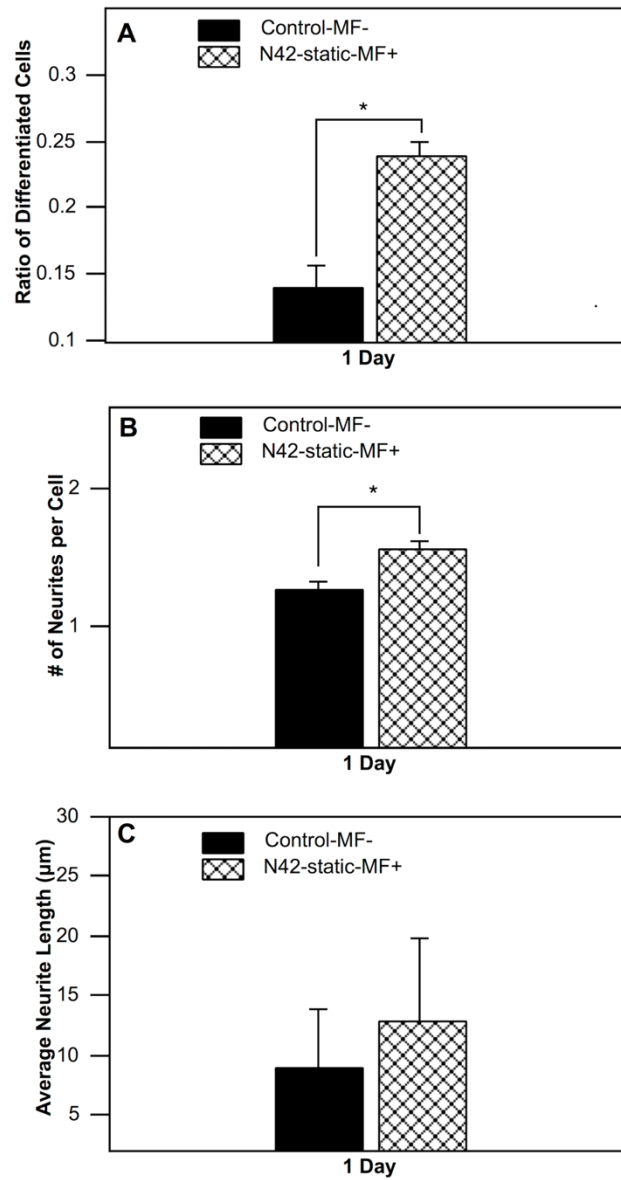
Figure A2. Morphology analysis for PC12 cells treated with and without N42 magnetic field for 1 day of incubation. (A) Percentage of differentiated neuronal phenotype cells (B) Number of neurites per cell (C) Average neurite length; *p < 0.05. Reprinted with permission from reference 90.

In Figure A2, the ratio of differentiated cells (72%), the number of neurites per cell (25%) and the average neurite length (43%) are significantly increased for cells treated with static N42 magnetic field compared with control group. In Figure A3, the magnetic field group exhibits the preferential alignment of the neurites along the direction of magnetic force.
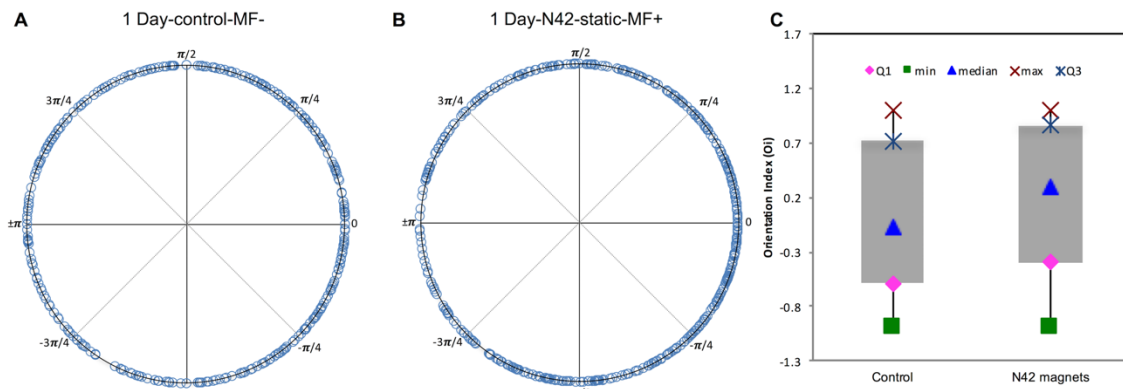

Figure A3. Neurite orientation (θ) distribution: (A) 1 day of incubation without magnetic field(control). (B) 1 day of incubation with N42 static magnetic field. (C) Orientation index (cosθ) distribution: The box plot represents the median, the first quartile, the third quartile, the maximum and the minimum value. cos~1 for the neurites long the direction of magnetic force. Reprinted with permission from reference 90.

APPENDIX B

CONCENTRATION-DEPENDENT PROMOTING EFFECT OF SPIO-AU CORE-

SHELL NANOPARTICLES: TOWARDS TISSUE DIFFERENTIATION (MC3T3-E1

CELLS)*

This work aims to explore the concentration-dependence of SPIO-Au core-shell NPs (17.3 ± 1.2 nm in diameter) on biocompatibility and osteogenic differentiation of preosteoblast MC3T3-E1 cells. The stability of NPs was first investigated by UV-Vis absorption spectra and zeta potential measurement. Then concentration effects of NPs (10-80 μg/mL) were evaluated on viability, morphology, proliferation, cellular uptake and alkaline phosphate (ALP) activity levels. Results have shown no acute toxicity (viability > 93%) or morphological difference at all concentration levels of NPs. The proliferation results indicated that NP of 10 μg/mL could promote the cell proliferation to 100% confluency at 7 days of incubation. Transmission electron microscopy (TEM) images revealed the successful internalization of NPs into MC3T3-E1 cells and the dose-dependent accumulation of NPs inside the cytoplasm. The ALP level of MC3T3-E1 cells was improved by 49% (of control) after treated with NPs at 10 μg/mL for 10 days, indicating their positive effect on early osteogenic differentiation. This study confirmed the excellent biocompatibility of SPIO-Au NPs and their great potential for promoting

---

osteogenic differentiation and promised the future application for these NPs in bone engineering including drug delivery, cell labeling and activity tracking within scaffolds.

Materials and Methods

Cell culture

MC3T3-E1 cells at passage-8 were cultured in Petri dishes with cell growth medium, which consisted of 89% alpha Minimum Essential Medium (αMEM) (Gibco, Grand Island, NY), 10% fetal bovine serum (Gibco, Grand Island, NY) and 1% penicillin streptomycin solution (Gibco, Grand Island, NY). The cells were kept in a 5% CO_2 atmosphere at 37°C. The cell growth medium was replaced every two days and the cells were passaged at sub-confluency.

Cell viability assessment and cell morphology observation

The cell viability test was performed by using a Cellstain double staining kit (04511, Sigma-Aldrich, St. Louis, MO). Briefly, MC3T3-E1 cells were seeded into 96-well tissue culture plates at a density of 1000 cells per well with growth medium. After 24 h of incubation, the medium was replaced by fresh growth medium containing SPIO-Au NPs at different concentrations (10, 20, 40, and 80 μg/mL). Cells without NPs were seeded as a control group. All the cells were incubated for 1, 3 and 7 day(s) for further testing. At each time period, the cells were washed with Dulbecco's phosphate-buffered saline (DPBS) twice and incubated in 100 μL of the assay solution (5 mL of DPBS containing 10 μL of calcein-AM and 5 μL of propidium iodide) in each well for 15 min. The live/dead fluorescence images were captured using an Axiovert 200M Inverted Fluorescence/phase Contrast Microscope (Carl Zeiss Inc.) equipped with an AxioCam CCD camera. The cell

morphology was also observed and recorded with this inverted microscope after 3 and 7 days of incubation.

Cell proliferation assay

The proliferation of MC3T3-E1 cells was measured using a CCK-8 cell counting kit (Sigma-Aldrich, St. Louis, MO). MC3T3-E1 cells were seeded into 96-well tissue culture plates at a density of 1000 cells per well with growth medium. After 24 h of incubation, the medium was replaced by fresh medium containing SPIO-Au NPs at different concentrations (1, 5, 10, 20, 40 and 80 μg/mL). Cells without NPs were seeded as a control group. All the cells were incubated for 1, 3 and 7 day(s). At each time period, the cells were washed with DPBS and followed by adding 100 μL of growth medium and 10 μL of CCK-8 solution to each well. Then after 2 h of incubation the intensity was measured at the wavelength of 450 nm by using a microplate reader (SpectraMax i3x, Molecular Devices Inc.).

Transmission electron microscopy (TEM)

To observe the cell uptake of SPIO-Au NPs in MC3T3-E1 cells, cells were seeded on a Aclar® (Electron Microscopy Sciences Inc.) film in a 12-well plate at a density of $1*10^5$ cells per well and incubated with growth medium containing SPIO-Au NPs at concentrations of 40 μg/mL and 80 μg/mL, respectively. After 48 h of incubation, cells were prefixed in 3% Electron Microscopy (EM) grade glutaraldehyde in 0.1 M phosphate buffer saline (PBS), pH 7.4 at room temperature for 1 h. Cells were then fixed in 1% osmium tetroxide in 0.1 M PBS, pH 7.4. Followed by the dehydration in a graded series of ethyl alcohol and embedded in Durcupan resin (Sigma-Aldrich, St. Louis, MO).

Ultrathin sections (80 nm) were cut with a Leica EM UC7 Ultramicrotome (Leica Microsystems Inc.) and collected on formvar coated copper slot grids. Then these sections were stained with uranyl acetate and lead citrate and then analyzed by using a FEI Tecnai12 BioTwinG^2 transmission electron microscope with an AMT XR-60 CCD Digital Camera system, at an accelerating voltage of 80 kV.

Alkaline phosphatase activity (ALP) assay

To study the performance of SPIO-Au NPs in osteogenic differentiation of MC3T3-E1 cells, the ALP activity level was assessed by using an Abcam$^®$ Alkaline phosphatase assay kit (ab83369, Abcam, Cambridge, MA). MC3T3-E1 cells were seeded into a 24-well plate at a density of $5*10^4$ cells per well with growth medium. After 24 h of incubation, the medium was changed to osteogenic induction medium, containing SPIO-Au NPs at different concentrations (0, 1, 5, 10 and 20 μg/mL). The osteogenic induction medium consisted of αMEM (Gibco, Grand Island, NY) supplemented with 10% fetal bovine serum (Gibco, Grand Island, NY), 1% penicillin (Gibco, Grand Island, NY), 10 mM disodium β–glycerophosphate (Sigma-Aldrich, St. Louis, MO), 10 nM dexamethasone (Sigma-Aldrich, St. Louis, MO) and 0.28 mM ascorbic acid (Sigma-Aldrich, St. Louis, MO). All the cells were incubated for 7, 10 and 14 days. At each time period, cells were harvested following the manufacturer's instruction. The intensity was measured at the wavelength of 405 nm on a microplate reader (SpectraMax i3x, Molecular Devices Inc.). The amount of ALP in each well was calculated and normalized by total protein content, which was measured simultaneously using the Pierce^{TM} Coomassie (Bradford) protein assay kit (Thermo Scientific, Rockford, IL).

Statistical analysis

All results were analyzed based on 3 independent experiments and expressed using the standard deviation. Statistical analysis was performed by the one-way analysis of variance (ANOVA) and Tukey post hoc test. Each sample group treated with NPs was compared with the control group. P value less than 0.05 was considered as a significant difference.

Results

Cell viability of SPIO-Au NPs: Fluorescence images and statistics

The treatment of live/dead double staining was performed to assess the viability on cells treated with SPIO-Au NPs at concentrations of 10, 20 40 and 80 μg/mL for 1, 3 and 7 day(s) of incubation. As observed, all groups of cells exhibited high cell viability with scarcely any dead cells (red staining) in comparison to the control group (Figure B1).

The number of viable and dead cells in the fluorescence images was counted and plotted (Figure B2). The percentage of live cells to the total cells showed no significant difference for 1 and 3 day(s) of incubation. Although a slight reduction of viability was observed at the highest concentration of 80 μg/mL for 7 days of incubation, SPIO-Au NPs still had 93% viability of MC3T3-E1 cells. No obvious cytotoxic effect was found with the treatment of SPIO-Au NPs.

Cell morphology: time and concentration dependence study

The morphology of cells treated with the SPIO-Au NPs was observed by an inverted light microscope (Figure B3). After 3 and 7 days of incubation, MC3T3-E1 cells were formed with spindle shapes. The increase of the number of cells was observed at a

longer incubation period (7 days). No significant difference in morphology was observed between the cell groups treated with NPs and the control group at each time period.
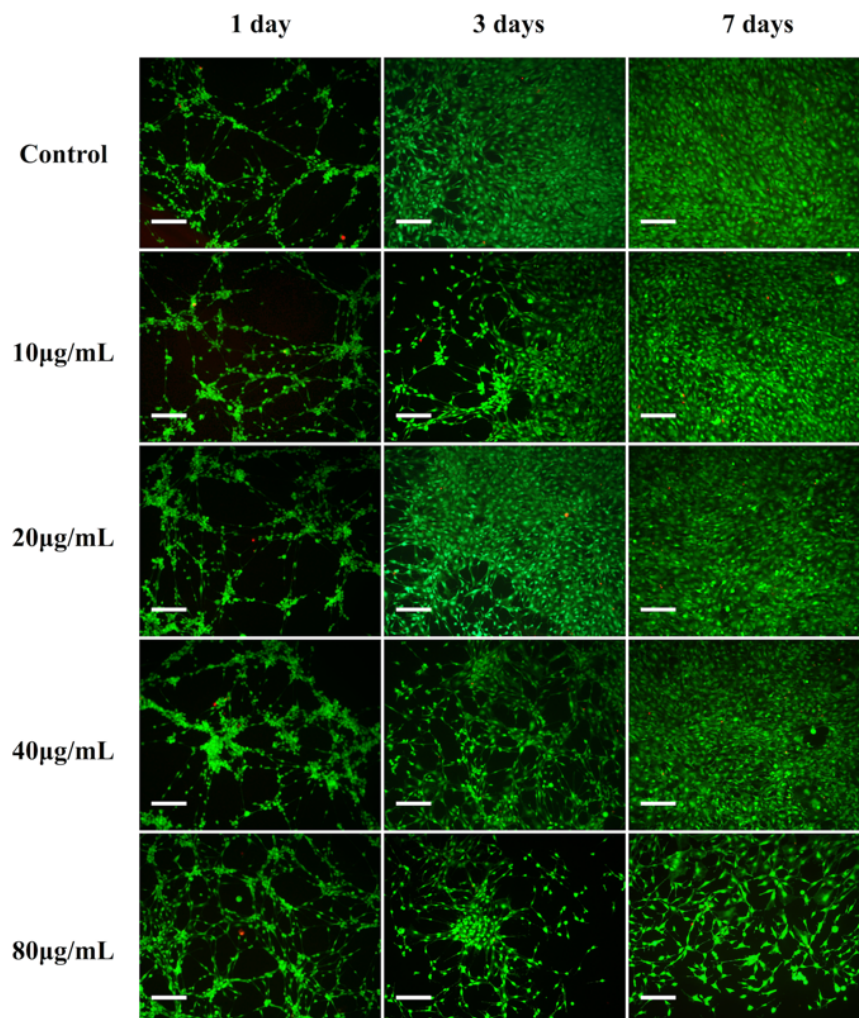

Figure B1. Fluorescence images for live/dead double staining tests after the cells were cultured with different concentrations of SPIO-Au NPs for 1, 3 and 7 day(s) in growth medium. Live and dead cells were stained by the calcein AM and the propidium iodide respectively. Green color represents viable cells while red color represents dead cells. Scale bar length = 200 μm. Direct observation of live cells and dead cells was provided to guarantee the accuracy. Reprinted with permission from reference 109.
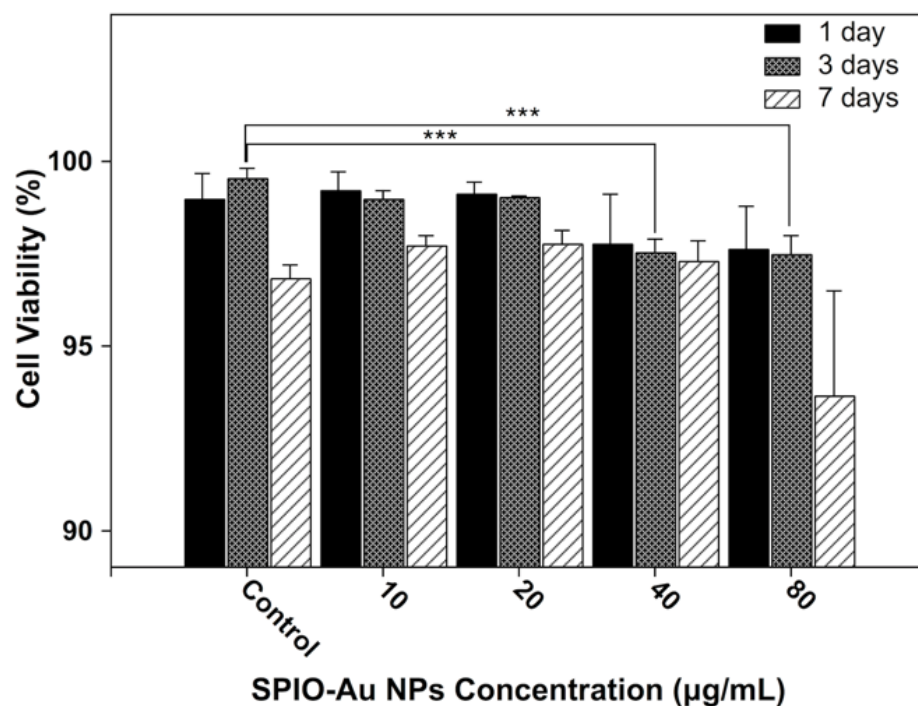
Figure B2. Cell viability determined by fluorescence images of live/dead cells. The number of live cells and dead cells were counted by using Matlab. Cells containing no NPs were used as the control group. Viability higher than 93% was observed for each sample group. Slight reduction of viability happened at the highest concentration after 7 days incubation. ((***) $p \leq 0.001$). Reprinted with permission from reference 109.
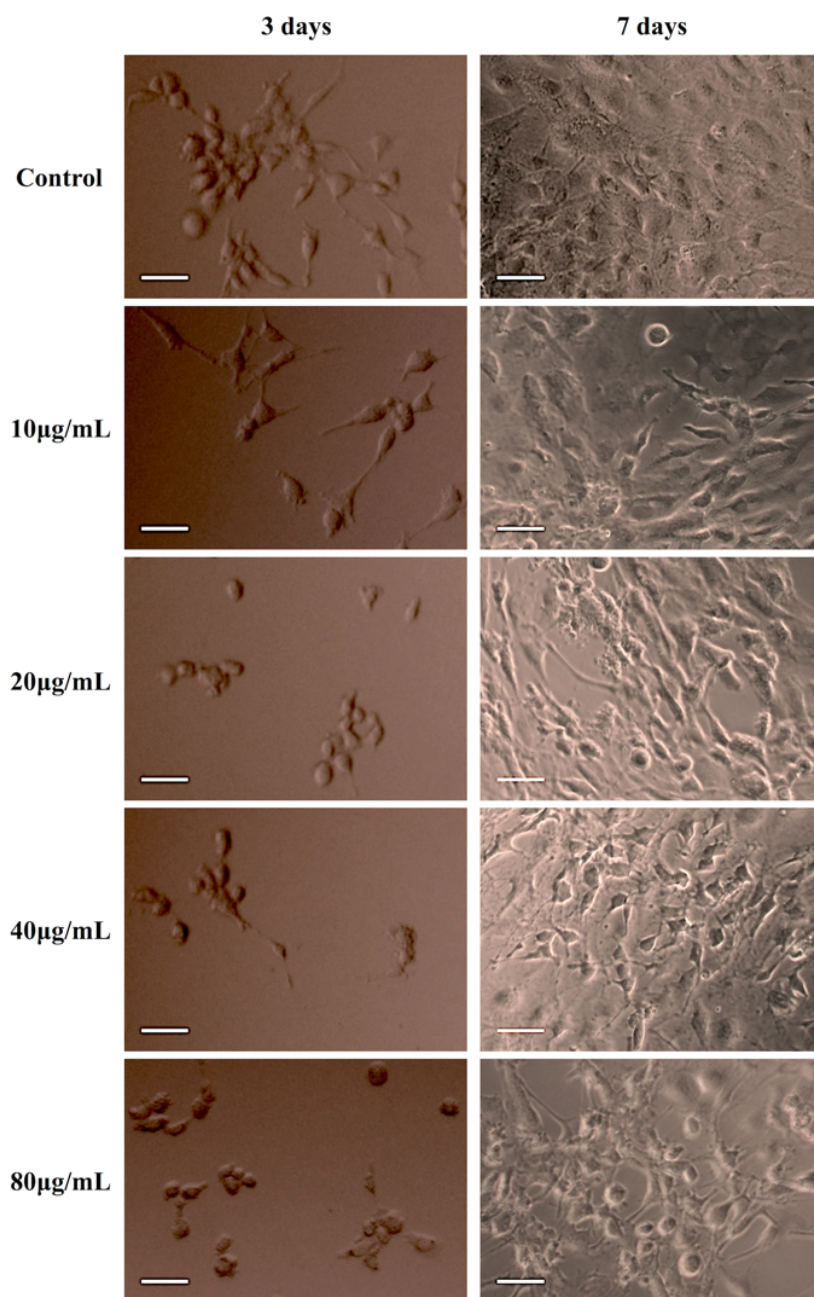
Figure B3. Cell morphology images by using an inverted light microscopy after cells were treated with different concentrations of SPIO-Au NPs for 3 and 7 days of incubation. The increase of cell density was observed at a longer time period. Scale bar length = 100 μm. Reprinted with permission from reference 109.

Cell proliferation: Curve-fitted modeling and analysis

The proliferation of MC3T3-E1 cells treated with the SPIO-Au NPs at concentrations of 0, 1, 5, 10, 20, 40 and 80 µg/mL was determined at different time points up to 7 days (Figure B4). The standard curve of Absorbance vs. Cell concentration was generated to reflect the relationship between the absorbance and the cell concentration by using a CCK-8 kit (Figure B5). Results show that the absorbance was increased at higher concentration, which approximated a linear relationship when the concentration was below the threshold value of $1.5*10^5$ cells/mL. Results of the proliferation assay in Figure B4 showed a significant reduction of the proliferation rate for 3 days of incubation when the concentration reached 80 µg/mL. However, there was no significant decrease of the proliferation rate at lower concentration levels ($\leq$ 40 µg/mL) for 3 days of incubation and at the whole concentration range (1-80 µg/mL) for 1 day and 7 days of incubation.

Cellular uptake of SPIO-Au NPs: TEM analysis

To examine the cellular uptake of the SPIO-Au NPs, MC3T3-E1 cells were incubated for 48 h after treated with NPs at concentrations of 40 and 80 µg/mL, respectively. As shown in the TEM images (Figure B6), the clusters of SPIO-Au NPs were found inside each MC3T3-E1 cell, indicating the successful internalization of NPs at both concentration levels.
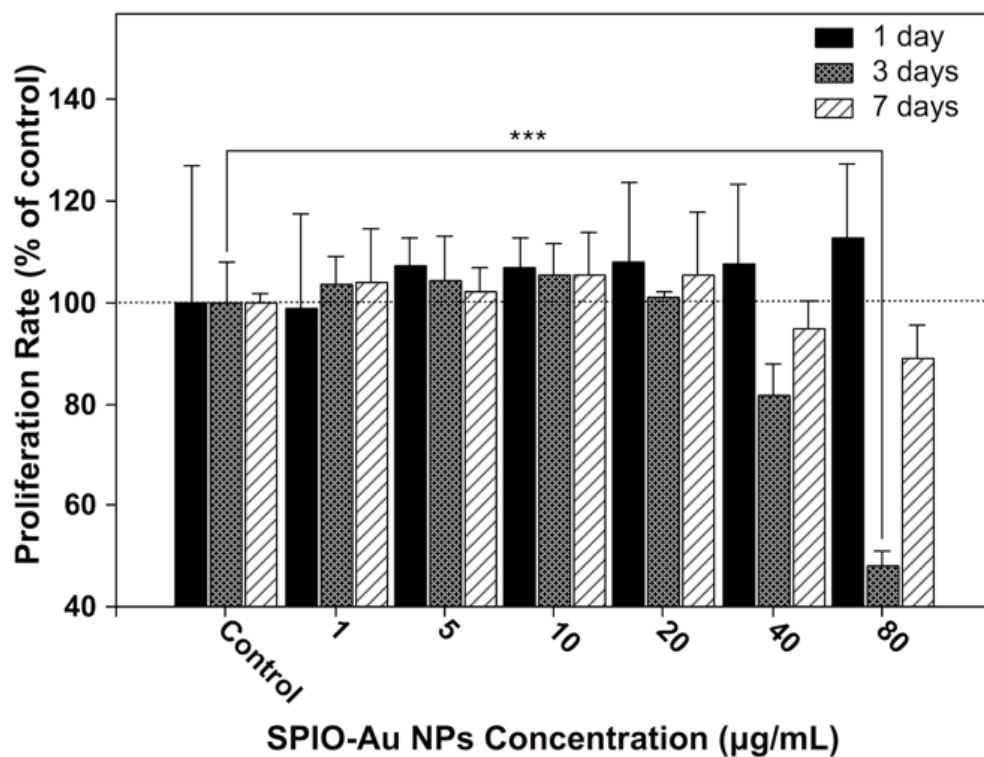
Figure B4. Proliferation of MC3T3-E1 cells treated with different concentrations of SPIO-Au NPs determined by a CCK-8 kit. Cells were cultured for up to 1, 3 and 7 day(s) in cell growth medium. Cells containing no NPs were used as the control group. ((***) p ⩽ 0.001). Reprinted with permission from reference 109.
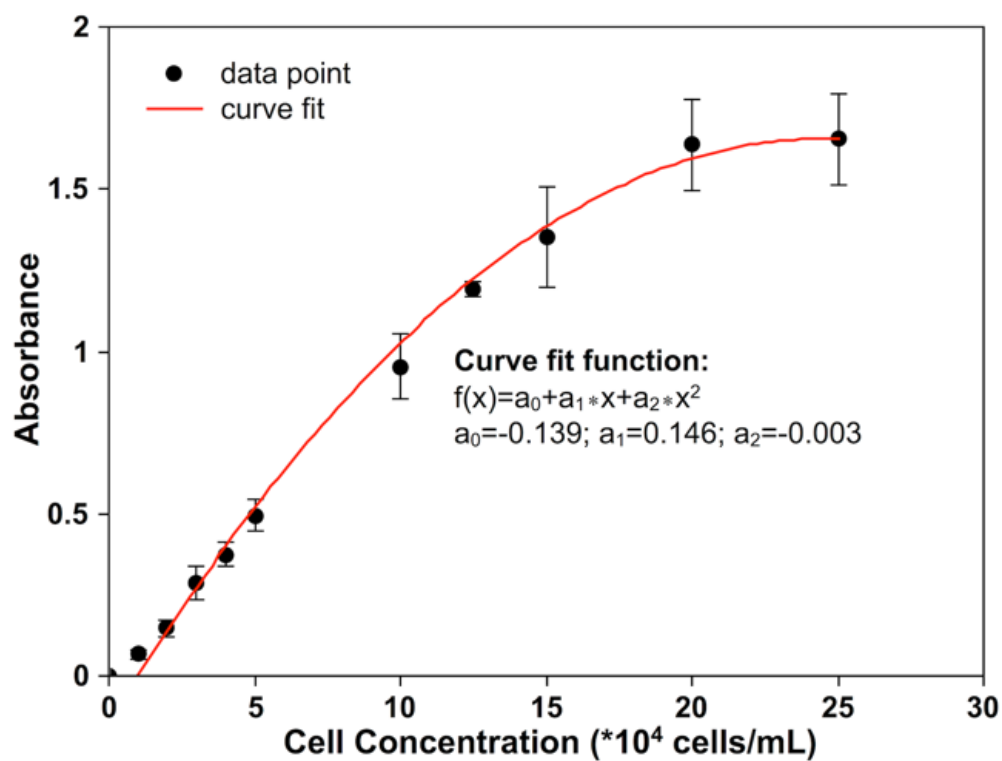
127

Figure B5. Standard curve of absorbance vs. cell concentration by experimentally measuring the absorbance of cells at different concentration. The linear-like region was found at the concentration below 1.5*105 cells/mL, indicating that the absorbance measurement can be used to reflect the change of cell concentration. The curve fit was performed by SciDAVis software using Polyfit4 function. Reprinted with permission from reference 109.
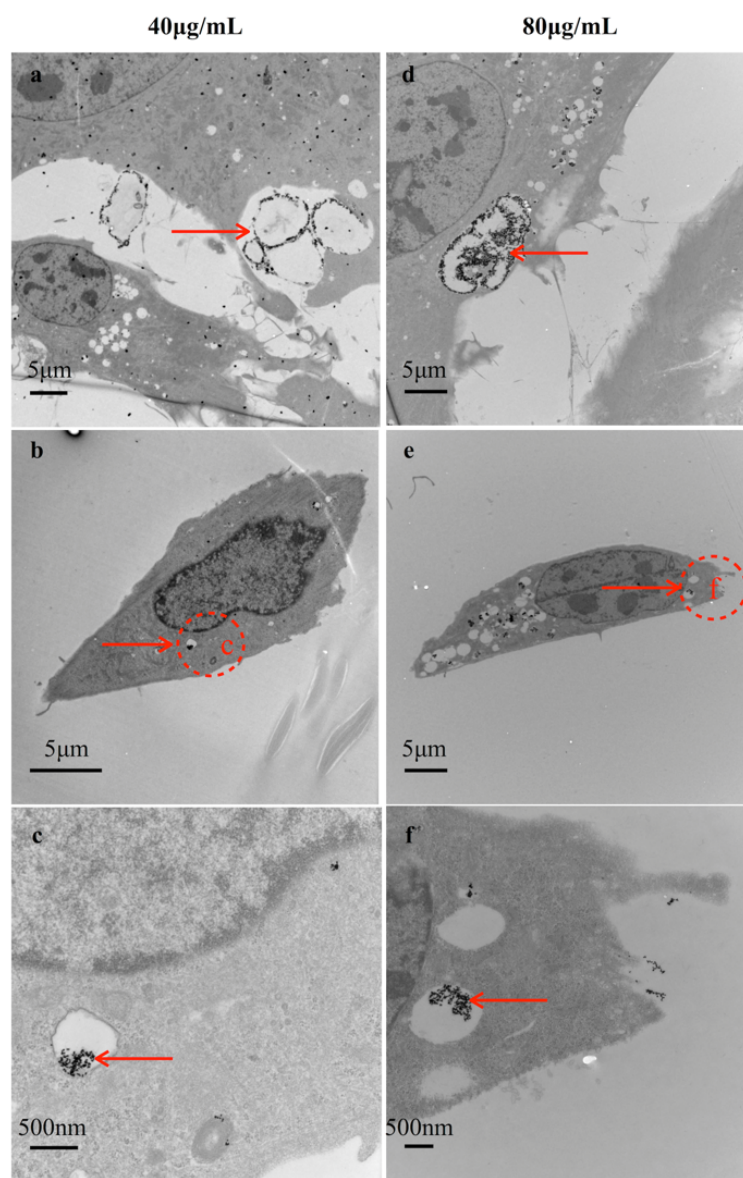
Figure B6. Transmission electron microscopy (TEM) images of MC3T3-E1 cells treated with SPIO-Au NPs at 40 μg/mL (a, b, c) and 80 μg/mL (d, e, f) after 48 h of incubation. Note: (c) and (f) are enlarged images of areas shown inside the dashed circles in (b) and (e). The arrows in (a), (c), (d) and (f) showed the accumulation of SPIO-Au NPs inside the cellular cytoplasm. In particular, (a) and (d) illustrated how NPs penetrated into cells through endocytosis. Reprinted with permission from reference 109.

Interestingly, the internalized NPs mainly located inside the endosomal vesicles in the cytoplasm, rather than in the nucleus, as preferred. Larger clusters of NPs were found in the vesicles at a higher concentration (80 µg/mL), than that at a lower concentration (40 µg/mL). For both concentrations, some NP clusters were found in the endocytic pathway, suggesting that NPs penetrated into cells mainly through endocytosis.[72,146]

It can be readily seen how the plasma membrane engulfed the cluster of NPs (the areas pointed by arrows) before their penetration into the cytoplasm (Figure B6(a) and (b)), which was the sign of early endocytosis.[59] Moreover, examined from all the TEM images, the MC3T3-E1 cells treated with NPs at concentrations of 40 and 80 µg/mL had intact cytoplasmic membranes, indicating the excellent biocompatibility of SPIO-Au NPs.

Promoting the osteogenic differentiation of MC-3T3-E1 cells

The ALP activity assay was conducted to explore the concentration-dependence of SPIO-Au NPs on the osteogenic differentiation (Figure B7(a)). Cells were treated with NPs at concentrations of 1, 5, 10, and 20 µg/mL in the osteogenic induction medium for 7, 10 and 14 days. It was found that the ALP level of MC3T3-E1 cells was affected by the treatment of NPs in a time and dose dependent manner. The significant increase of ALP level per gram of protein was displayed at 10 and 20 µg/mL for 14 days of incubation, with the maximum increase of ALP level by 49% at 10 µg/mL.

Interestingly, the ALP level of groups treated with NPs was slightly reduced after 7 days of incubation, while promoted after 10 and 14 days of incubation. It was speculated that for a short time incubation (7 days), most NPs might not be able to interfere with the

cells yet. The ALP level normalized by protein content exhibited the similar trend (Figure
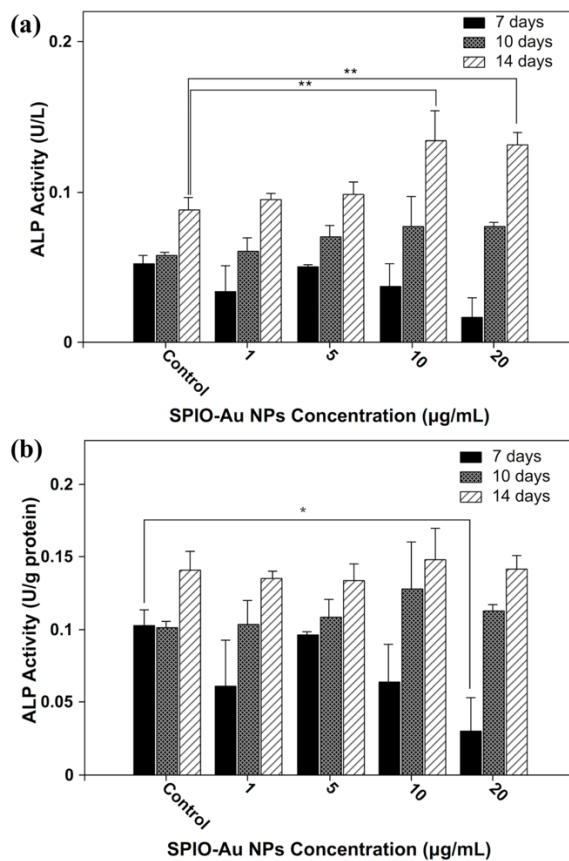
B7(b)).

Figure B7. (a) The Alkaline phosphatase activity level of MC3T3-E1 cells treated with

different concentrations of SPIO-Au NPs for 7, 10 and 14 days of incubation (original

data without normalization by protein content). Cells containing no NPs were used as the

control group. ((**) $p \leqslant 0.01$) (b). The Alkaline phosphatase activity level of MC3T3-

E1 cells treated with different concentrations of SPIO-Au NPs for 7, 10 and 14 days of

incubation (Normalized by protein content). Cells containing no NPs were used as the

control group. ((*) $p \leqslant 0.05$, (**) $p \leqslant 0.01$)). Reprinted with permission from reference

109.

Discussion

Our goal is to evaluate the concentration-dependence of SPIO-Au NPs (17.3 ± 1.2 nm) on the osteogenic differentiation of the MC-3T3-E1 preosteoblast cell line. This work lays the foundation for future applications of these NPs in tissue engineering, such as drug or gene delivery, cell labeling and tracking within scaffolds.

Our results showed an excellent cell viability ($\geq 93\%$) for the SPIO-Au core-shell NPs at concentrations of 10, 20, 40 and 80 µg/mL. The cell morphology observation clearly exhibited the unchanged shape and size of cells treated with SPIO-Au NPs at all tested concentrations, and demonstrated that the near-zero influence of cellular internalization of NPs on the cellular morphology. This supports the aforementioned viability result. More morphological work in 3D network, i.e. scaffolds, could be performed in the near future.

The proliferation results proved the optimal concentration range of the NPs (≤ 40 µg/mL) and saturation could be reached at much faster rate with higher NP concentrations (> 40 µg/mL). The inhibition of proliferation may happen when the concentration of NPs reaches 80 µg/mL, while interestingly the viability of cells still maintained above 93% for concentrations up to 80 µg/mL. This suggests that, longer incubation days (> 1 day) or higher NP concentration levels (> 40 µg/mL) are not necessary for obtaining optimal proliferation benefits. For instance, NP of 10 µg/mL could promote the cell proliferation to 100% confluency at 7 days of incubation.

TEM analysis provided a direct tool to observe the existence of NPs absorbed by MC3T3-E1 cells. The size and the number of the NP clusters shown in TEM images

demonstrated the dose-dependence of cellular NPs uptake. The fact of NPs staying inside the vesicles within the cytoplasm structure implied the possible mechanism of cell internalization by endocytosis at the concentrations of 40 and 80 μg/mL, which was further supported by some TEM images showing the engulfing of NPs by cells. The zeta potential measurement showed that the surface charge of the SPIO-Au NPs is negative (-31.7mV in water) due to the existence of citric acid as the stabilizing ligand, while the surface charge was increased to -11.9 mV (in cell growth medium), which implies the surface modification of SPIO-Au NPs by the nonspecifically absorbed serum proteins. Therefore, we hypothesize that the access of NPs into cells was induced by serum proteins, which were absorbed onto the surface of SPIO-Au NPs, via receptor-mediated endocytosis. This mechanism has been proposed by Chithrani et al.[147] and Mustafa et al.[59] for the study of the internalization of Au NPs by Hela cells and ME3T3-E1 cells, respectively. At the concentration as low as 10 μg/mL, Thikra et al.[27] suggested that NPs may penetrate into the cells individually rather than through endocytosis. Moreover, the intact cell membranes indicated the excellent biocompatibility of SPIO-Au NPs, which has been proved before by viability results. We can also conclude that the uptake of NPs into cells did not induce any cellular toxicity (viability > 93%). In addition, the surface modification of SPIO-Au NPs also plays an important role in cell uptake as it determines the surface charge and the hydrophilicity[148] of NPs. Cho[149] found that the surface conjugation of different groups changed the amount of the NPs internalized by SK-BR-3 cells in the following order: poly(allylamine hydrochloride) > anti-HER2 > antibody > poly(ethylene glycol). To determine the best mechanism for cellular NP uptake and cellular kinetics,

longer incubation time, more time points and necessary surface functionalization are needed for future study.

The results from viability, proliferation, morphology and TEM analysis indicated that SPIO-Au NPs did not induce acute toxicity on MC3T3-E1 cell line. Based on the biocompatibility evaluation, The ALP activity measurements were designed and performed to assess the potential of SPIO-Au NPs in osteogenic differentiation. The results exhibited the promoted effect of SPIO-Au NPs on the early osteogenic differentiation of MC3T3-E1 cells. Pure Au NPs have been shown to promote the osteogenic differentiation of ADSCs.[145] However the examination of the SPIO-Au NPs core-shell on osteogenesis have not been mentioned in any of previous works. The presented work is the first to confirm the osteogenic effect of SPIO-Au NPs for the application in bone cell regeneration. The ALP level is known to be an early phenotypic marker for osteogenic differentiation.[150] In the next stage, matrix mineralization and specific gene expression will be studied to further examine the effect and mechanism of SPIO-Au NPs on osteogenesis. To enhance their promotion effect on bone tissue regeneration, NPs can be embedded into scaffolds in the near future. In particular, composite scaffolds are able to provide enough surface roughness for cellular attachment and improve the mechanical strength of the system.[151] Incorporating NPs with osteogenic agents,[152] growth factors[153] and drugs are some other promising strategies to promote cell differentiation and/or add more functionality to the scaffolds.[154] Moreover, to enhance the contrast capability, SPIO-Au NPs can be combined with other types of nanocomposite scaffolds.[155]

Conclusions

In this work, we synthesized SPIO-Au core-shell NPs with uniform size (17.3 ± 1.2 nm), shape (spherical) and excellent stability in DI water and the MC3T3-E1 cell growth medium. Experimental results suggest that SPIO-Au NPs (10, 20, 40 and 80 μg/mL) didn't induce acute toxicity for up to 7 days of incubation. The existence of SPIO-Au NPs does not affect the proliferation of MC3T3-E1 cells at the concentration range between 1 and 40 μg/mL. The TEM results revealed the cellular uptake of SPIO-Au NPs through endocytosis and the dose-dependence of internalization of NPs into cells. The enhanced ALP activity level of cells treated by NPs implied their potential in promoting the osteogenic differentiation of MC3T3-E1 cells. Further investigation of SPIO-Au NPs integrated with 3D scaffolds and/or growth factors as well as the in-vivo studies will be performed in the near future to explore their promising applications in bone tissue engineering.